Conducting Polymers as Functional Binders for Lithium Ion Battery Positive Electrodes

(Leitfähige Polymere als funktionale Bindermittel für positive Elektroden in Lithium-Ionen-Batterien)

Von der Fakultät für Mathematik und Naturwissenschaften
der Carl von Ossietzky Universität Oldenburg
zur Erlangung des Grades und Titels eines

Doktors der Naturwissenschaften (Dr. rer. nat.)

angenommene Dissertation

von Herrn Pratik Ranjan Das, M.Sc.
geboren am 30.05.1987 in Basudevpur
Oldenburg, April 2016

Diese Arbeit wurde in der Zeit von November 2012 bis April 2016 unter der Betreuung von Herrn Prof. Dr. Gunther Wittstock am Institut für Chemie und dem Center of Interface Science an der Carl von Ossietzky Universität Oldenburg angefertigt. Die experimentellen Arbeiten wurden am Oldenburger Forschungszentrum NEXT ENERGY• EWE Forschungszentrum für Energietechnologie e.v. durchgeführt, das auch die Finanzierung dieser Dissertation sicherstellte.

Teile dieser Arbeit wurden bereits veröffentlicht. Diese sind durch römische Ziffern gekennzeichnet und in Abschnitt 10 erfasst.

Gutachter: Prof. Dr. Gunther Wittstock
Zweitgutachter: Prof. Dr. Michael Wark
Tag der Disputation: 01/01/2016

This thesis is dedicated to my lovely grandparent.

Acknowledgement

First of all I would like to thank my supervisor, Prof. Dr. Gunther Wittstock for his excellent guidance and support. His advice and insight into my PhD work is invaluable. My thanks to Prof. Dr. Michael Wark and Prof. Dr. Carsten Agert for accepting to be in my examination committee.

I also thank Dr. Lidiya Komsiyska for her guidance, support and fruitful discussion throughout my thesis work and my fellow PhD students Jan grosse Austing, Barbara Satola and Timo Di Nardo for their scientific insight and light hearted discussions throughout my time at work. I would like to thank Alexander Gräfenstein for his help in scientific work for my thesis. I would also like to thank Dr. Wedigo von wedel and Dr. Oliver Osters for their guidance and support during my PhD time period.

I thank Benedikt Burger, Sergio Garnica for their support during my lab work. I would like to thank all the co-workers at energy storage department at Next-Energy for providing pleasant and productive research atmosphere.

I would like to thank Next-Energy for providing financial support and a productive scientific facility to carry out my research work.

I would personally like to thank Martina Elsner for her help in administrative work at Next-Energy. Finally, I would like to thank my parent, brothers and sister in-laws and friends in India and Germany for their help, support, understanding and encouragement during my PhD work.

Abstract

Lithium ion batteries have been successfully used in portable electronics applications. Their application areas are growing continuously. For their commercial application in electromobility and stationary storage, high energy density, high rate capability and long cycle life is required. This work demonstrates the improvement in energy density and rate capability of $LiFePO_4$ composite positive electrodes by replacing conventional binders with conducting polymers such as polyaniline (PANI), poly-*o*-methoxy aniline (POMA), poly(3,4-ethylenedioxythiophene):polystyrene sulfonate (PEDOT:PSS). Conducting polymers act in a dual role as binder and conducting additive in the positive composite electrode. The capacity and charging rate capability of the electrodes are improved by using PANI and POMA. However, due to their inherent lower conductivity in the emeraldine state, complete replacement of carbon additive is not possible. On the other hand in this work it is shown that PEDOT:PSS is stable and highly conducting in the working potential window of $LiFePO_4$ electrodes (2.8-4 V). Hence composite electrodes free of any carbon additive are prepared with PEDOT:PSS and $LiFePO_4$. In order to understand the flow behaviour of composite slurries with different solid content; rheological measurements is performed with rheometer. All slurries show solid-like behavior due to formation of a network structure of $LiFePO_4$ bridged by PEDOT:PSS chains. However, the solid loading of the slurries influences the distribution of the agglomerates and the binder affecting also the thickness, the adhesion and the electrical conductivity of the coatings casted from the different slurries under the same conditions. The optimum electrochemical performance is achieved with slurries containing 40 % solid loading. Electrodes with different PEDOT:PSS composition is prepared and their morphometric properties are studied using scanning electron microscope (SEM), mercury porosimetry and high resolution X-ray computer tomography. The electrochemical performance and the cycling stability of the composite electrodes are compared to the behaviour of conventional positive electrodes with carbon additives and PVDF binder. With increasing PEDOT:PSS content a decrease in the overvoltage and correspondingly an improvement in the rate capability is observed. Composite electrodes containing 8% PEDOT:PSS show comparable electrode capacity and better cycling stability as compared to conventional PVDF based system.

Zusammenfassung

Lithium-Ionen-Batterien sind heutzutage nicht nur in Mobilgeräten erfolgreich eingesetzt, sondern erfahren einen stetigen Zuwachs in verschiedensten Anwendungsbereichen. Für den kommerziellen Einsatz in der Elektromobilität und als stationärer Speicher sind jedoch eine hohe Energiedichte, hohe Lade-/Entladeraten, sowie eine gute Zyklenstabilität notwendig. In dieser Arbeit wird die Verbesserung der Energiedichten und der Lade /Entladeraten von Lithium-Ionen-Batterien durch den Austausch von konventionellen Bindern im Kompositen des positiven Elektrodenmaterials $LiFePO_4$ mit leitfähigen Polymeren wie Polyanilin (PANI), Poly-*o*-methoxyanilin (POMA), Poly(3,4-ethylendioxythiophen):Polystyrensulfonat (PEDOT:PSS) gezeigt. Dabei agieren die leitfähigen Polymere sowohl als Binder als auch als leitfähiges Additiv in der Kompositelektroden. Der Einsatz von PANI bzw. POMA erhöht zwar die Kapazitäten und Leistungsfähigkeit der Elektroden, sorgt jedoch, aufgrund der niedrigeren elektrischen Leitfähigkeit im oxidierten Zustand der Polymere, dafür, dass das Kohlenstoffadditiv nicht komplett ersetzbar ist. PEDOT:PSS hingegen erweist sich als stabil und sehr leitfähig im Spannungsbetriebsfenster von $LiFePO_4$ (2.8-4 V). Daher wird aus dem PEDOT:PSS/$LiFePO_4$ Kompositelektroden frei von Kohlenstoffadditiven hergestellt und gründlich charakterisiert.

Um das Fließverhalten von Pasten mit unterschiedlichem Feststoffanteil des Komposites zu untersuchen, werden systematische rheologische Messungen durchgeführt. Alle Pasten zeigen, aufgrund der Bildung einer über PEDOT:PSS Ketten verbrückten Netzwerkstruktur, feststoffartiges Verhalten. Der Feststoffanteil der Pasten bestimmt die Verteilung der Agglomerate und der Bindermatrix. Dies wiederum beeinflusst die Dicke, die Adhäsion und die elektrische Leitfähigkeit der Kompositelektroden. Ein Optimum der elektrochemischen Leistungen wird durch eine Paste mit einem Feststoffanteil von 40 % erreicht.

Zudem wurde der Einfluss der Elektrodenzusammensetzung (unterschiedlichen PEDOT:PSS Anteilen) auf die morphologischen Elektrodeneigenschafften mittels Rasterelektronenmikroskopie (REM), Quecksilberporosimetrie und hochauflösende Röntgen Computertomographie (CT) untersucht. Das elektrochemische Verhalten und die Zyklenstabilität der Kompositelektroden wurden mit denen von konventionellen Kathoden (Kohlenstoffadditiv und Polyvinylidenfluoridbinder) verglichen. Mit steigendem PEDOT:PSS Anteil wird ein geringeres Überpotential und

dementsprechend verbesserte Lade/Entladeraten beobachtet. Im direkten Vergleich zeigt die Kompositelektrode mit 8 % PEDOT:PSS-Anteil eine vergleichbare Kapazität und eine bessere Zyklenstabilität als das konventionelle PVDF basierte System.

Contents

List of Abbreviations and Acronyms

PANI	Polyaniline
POMA	Poly-o-methoxy aniline
PEDOT:PSS	Poly(3,4-ethylenedioxythiophene): Polystyrene sulfonate
CP	Conducting polymer
SEI	Solid electrolyte interphase
LIB	Lithium ion battery
NMP	N-methyl pyrrolidone
CMC	Carboxymethyl cellulose
PVDF	Poly(vinylidenfluorid)
PMMA	Poly(methyl methacrylate)
PTFE	Poly(tetrafluoroethylene)
PEG	Polyethylene glycol
HPMC	Hydroxypropyl methylcellulose
PAALi	Lithium poly(acrylic acid)
PAANa	Sodium poyl(acrylic acid)
PA	Polyacelene
PT	Polythiophene
EB	Emeraldine base
ES	Emeraldine salt
EDOT	3,4-ethylenedioxythiophene
PPy	Polypyrrol
EC	Ethylene carbonate
EMC	Ethyl-methyl carbonate
IR	Infrared spectroscopy
TGA	Thermo gravimetric analysis
DSC	Differential scanning calorimetry
CV	Cyclic voltammetry
SEM	Scanning electron microscopy
EIS	Electrochemical impedance spectroscopy
CT	Computer tomography

symbol	Description	Unit
τ	Shear stress	Pa
γ	Shear strain	-
$\dot{\gamma}$	Shear rate	s^{-1}
μ	viscosity	Pa s
n	Power law coefficient	-
F	Force	N
A	Area	m^2
ω	Angular velocity	
f	Frequency	Hz
G	Modulus	GPa
τ_B	Batrex interaction parameter	-
φ	Volume fraction of solid	-
I	Current	A
E	Potential	V
t	Time	t
C-rate	Current rate	h^{-1}
T	Temperature	°C
R	Resistance	Ω
C	Capacitance	F
Z	Impedance	Ω
σ_{el}	Electrical conductivity	S cm^{-1}
σ	Adhesion strength	N m^{-2}
P	Pressure	N m^{-2}
r	Pore radius	m
θ	Contact angle	°
γ_s	Surface tension	N m^{-1}

1 Introduction

Modern day civilization has become very much dependent on fossil fuels which have finite supply and uneven global distribution. It has two important consequences: (1) vulnerability of nations to fossil-fuel imports and (2) CO_2 emissions that acidify the oceans and create global warming. If it is left unchecked, heat-trapping emissions, such as carbon dioxide (CO_2), are expected to cause irreversible damage to communities throughout the world. This damage will likely include increased urban air pollution and emerging infectious diseases such as West Nile Virus (1), sea-level rise causing flooding and erosion in coastal communities; extreme weather including more intense droughts and hurricanes; reduced productivity of some agricultural regions; and loss of many treasured landscapes and species from coral reefs to polar bears (2).

Renewable energy such as wind, solar, geothermal, hydroelectric provides substantial benefits for our climate, our health, and our economy. According to data aggregated by the International Panel on Climate Change, life-cycle global warming emissions associated with renewable energy including manufacturing, installation, operation and maintenance, and dismantling and decommissioning are minimal as compared to the fossil fuel system (3). Renewable energy sources, such as wind and solar, have vast potential to reduce dependence on fossil fuels and greenhouse gas emissions in the energy sector. Responding to climate change, state initiatives including renewable portfolio standards and consumer efforts are resulting in increased deployments of solar photovoltaics (PV) and wind turbines. Both technologies provide variable and uncertain (sometimes referred to as “intermittent” electricity supply). To determine the potential role of storage in the grid of the future, it is important to examine the technical and economic impacts of variable renewable energy sources.

It is not only necessary to generate energy from the renewable resources but to use greener ways for energy consumption. Mobility has been an important development for humans since years. However, today’s mobility is largely dependent on internal combustion engine which produces one third of total greenhouse gases on the planet. It has been suggested if electric vehicles replace the majority of gasoline powered transport, the greenhouse gas emission can be significantly reduced (4). However, there

are many challenges to be addressed before it comes to major main stream business and compete effectively with the gasoline vehicles.

Hence renewable energy generation and storage is the biggest challenge of 21st century. Electrochemical energy storage and conversion plays a crucial role in our daily life and it can provide solutions for environment issues as well. The development of greener, cheaper and safer rechargeable lithium ion battery has strategic importance for energy storage technology (5-7). This technology has potential to enable modern civilization to secure a sustainable, distributed energy supply and reduce the imprint on air pollution of the internal combustion engine and coal-fired power plants. Lithium ion battery (LIB) has high energy density, cyclic stability and relatively good power density. Hence, it has enabled the wireless revolution in portable electronics (cell phones, laptop computers, digital cameras, and iPads) and moving towards the bigger goal for electric mobility and grid scale storage possibilities. However, at present the cost and safety factors limit the use of these batteries extensively in grid and electric cars. Hence, there has been lot of effort put in the direction improving the performance and safety while reducing the cost of the system (8-10). Another major aspect is the charging time; it is limited by the rate capability of the battery. In this work this issue is addressed.

1.1 Structure of lithium ion battery

A lithium ion battery consists of several components such as negative electrode, positive electrode, separator, current collector and electrolyte. A schematic of lithium ion battery is shown in the Figure 1.1a. The positive electrode is typically an inorganic metal oxide or phosphate. A negative electrode typically consists of layered graphite material and a separator to avoid electrical contact between positive electrode and negative electrode. The separator is typically made from polymers or glass fibre. Both positive electrode and negative electrode have current collectors to carry the electrons in the outer circuit through the load. At the positive electrode side aluminium and at the negative electrode side copper is used as current collector. Electrolyte, made with Li^+ containing salts in an organic solvent is used to carry ions inside the cell. Li^+ ions move from the negative electrode to the positive electrode during discharging and from the positive electrode to the negative electrode during charging. After the first charging cycle, a thin layer of a solid interphase is deposited on the negative electrode side. This

results from irreversible electrochemical decomposition of the electrolyte because typical electrolytes are not stable at the operating potential of the negative electrode during charging. It is called solid electrolyte interphase (SEI). The SEI separates the strongly reducing lithiated graphite from the electrolyte and thus avoids further reduction of the electrolyte at the negative electrode in the following charging cycles. The material is conducting for Li^+ ions. This avoids further decomposition of negative electrode in the following charging cycles and allows the passage of ions. A schematic of a cylindrical lithium ion cell with layered electrode structure is shown in the Figure 1.1b. It can be seen that the current collectors are coated on both side and the electrode layers are rolled to fit in a cylindrical case.

Different electrodes (positive electrode and negative electrode) and their operating potential have been described in Figure 1.2. Different metal oxide and phosphate positive electrode ranges from potential 3 V to 4.5 V. Graphite is used as negative electrode material in most commercial batteries. However, silicon and pure lithium negative electrode show a huge potential in next generation lithium ion batteries due to the possibility of improving the energy density of the system (11).

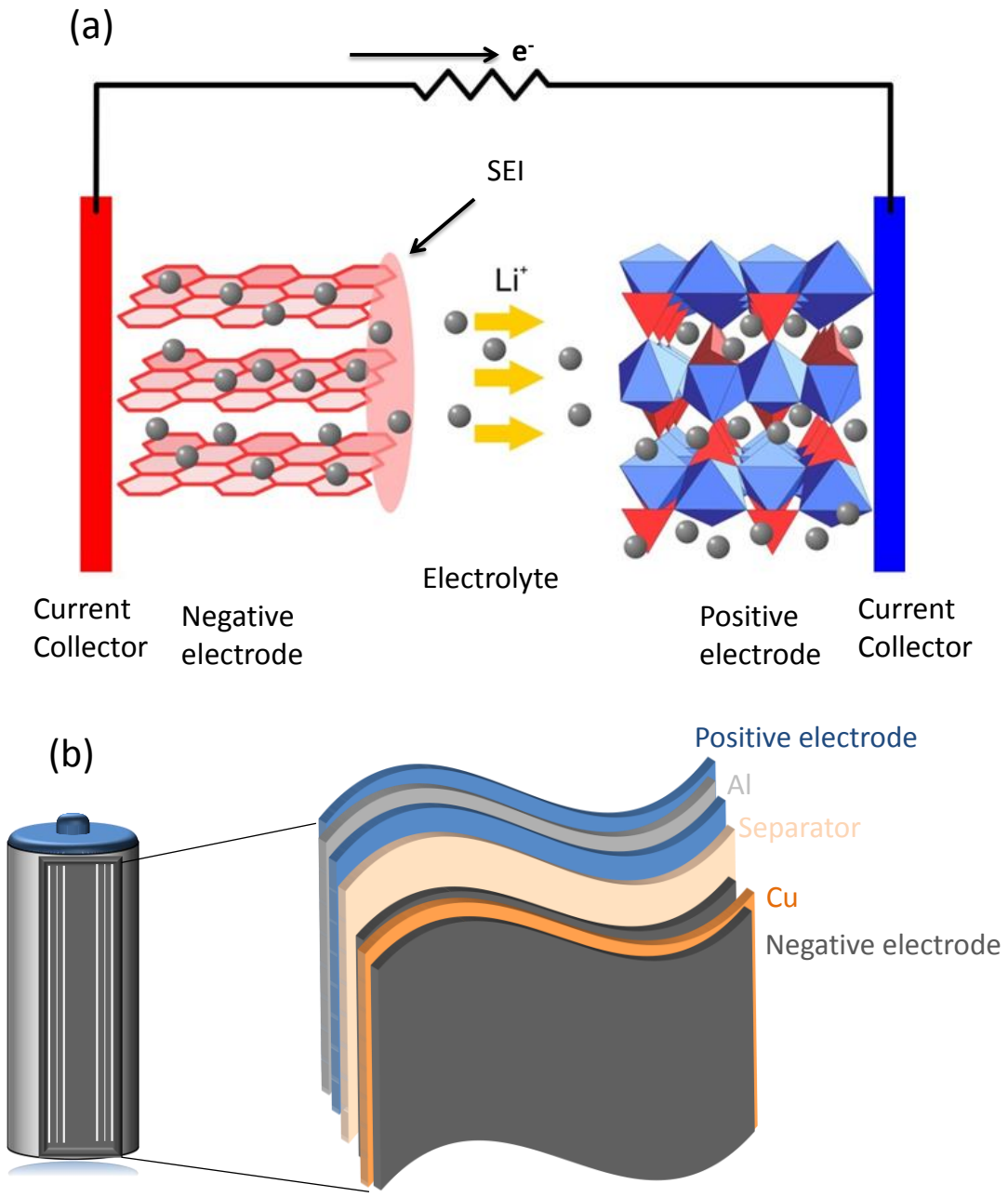

Figure 1.1. (a) Schematic of the reaction in a lithium ion battery, (b) Schematic of a cylindrical battery with composite electrodes.

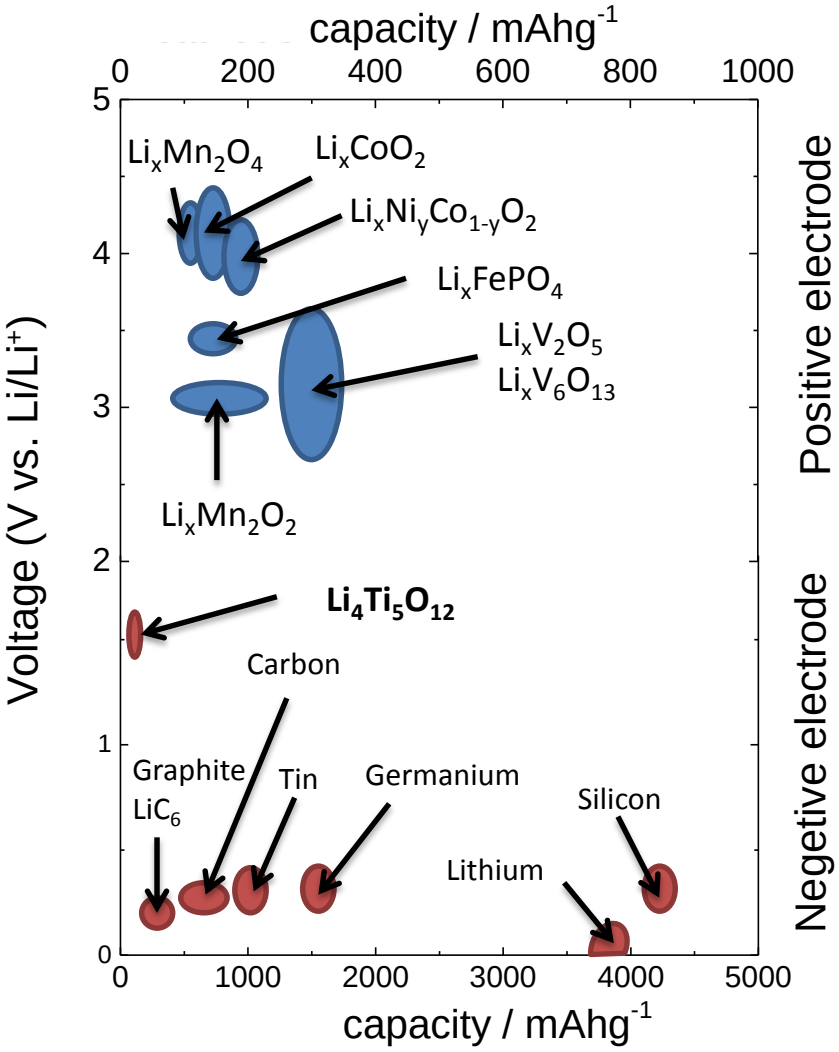

Figure 1.2. Li ion capacity and electrochemical reduction potentials with respect to Li metal for a range of positive electrode and negative electrode materials (12).

1.2 Composite electrodes

Lithium ion battery electrodes consist not only of active materials but contain other components such as conductive additive and binder. Hence it is called a composite electrode. A conductive additive is necessary to ensure high electrical conductivity of the composite electrode because the inherent electronic conductivity of the positive electrode materials is very low, it cannot conduct all the electrons to the current collector. Typical conductive additive used for positive electrodes is 5-10 % carbon black or carbon nanotubes. It is depicted in the Figure 1.3. A polymeric binder is required to bind active material and conductive additive together and give the electrode proper structure. It has many other functions described in the next chapter.

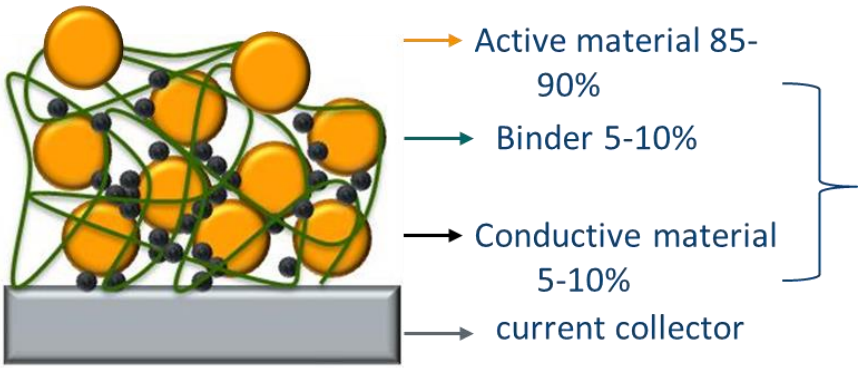

Figure 1.3. Schematic of a conventional positive electrode for lithium ion battery consisting of active material, binder and conductive additive.

1.3 New electrode design

In this PhD project a new electrode design is proposed. This concept has two components system consisting of active material and conductive binding agent. Here a conductive polymer (CP) performs a dual role of binder and conductive additive. The proposed structure is shown schematically in the Figure 1.4.

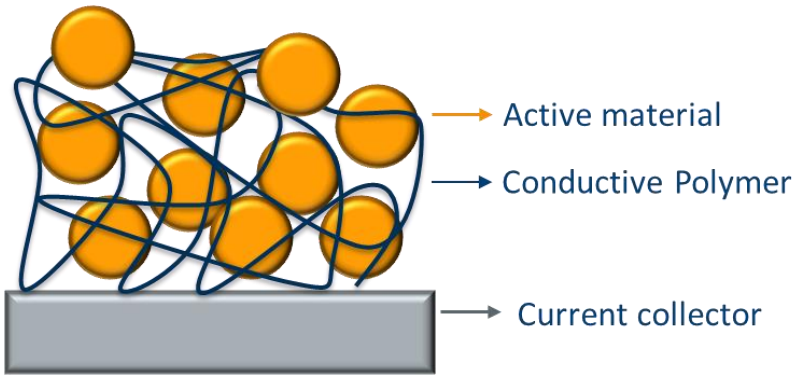

Figure 1.4. Schematic of the proposed two component composite positive electrode consisting of active material and conductive binder.

Reducing the three components system of Figure 1.3 to a two component system in Figure 1.4 provides many advantages in processing. The main potential advantages of the concept are:

1. The CP performs the dual role of binder and conductive additive. Hence loading of the active material in the composite electrode can be increased. This increases the capacity of the composite electrode. The binder and conductive additives are inactive component of a composite electrode. They do not add to the capacity of the

system. Hence their amount should be minimized. This can be achieved with the new concept.

2. CP is very flexible and due to their long chain structures they can provide good electrical connectivity between the active materials in the composite electrode. The conventional carbon additive provides a specific path for electron conduction (Figure 1.3) and does not connect all the active material uniformly. Hence the overall three dimensional conductivity of the two component system is expected to be better than that of conventional three component system. Hence the charging and discharging performances of these electrodes at higher rates are expected to be better.
3. With cycling, the active material particle can break due to volume changes. In conventional composite electrode, the active material loses contact with carbon additives after breaking, but in case of conducting polymer based composite positive electrodes, the active material remains in contact with the flexible polymers after breaking. This should improve the lifetime of the electrode and the cell.
4. N-methyl pyrrolidone (NMP) is used as a solvent for slurry processing technique of conventional composite positive electrode. This solvent is expensive, exhibits flammable vapours, and is highly toxic. Hence there is a lot of interest for developing water based industrial processing technique. Some of the conducting polymers are available as aqueous suspensions. Hence the processing of this new electrodes design can be environmentally friendly and cheaper.

There are many challenges to be studied in the new composite electrode system. These challenges are selecting the conductive polymers for the operating potential range of the battery; to study their behaviour in the organic battery electrolyte. Different kinds of CP show redox activity in different potential ranges. Hence they affect the performance of composite electrode with active material differently if they are redox active in the active potential range of active material or redox inactive.

To obtain uniform coatings, the flow behaviour of the composite electrodes with the new binder need to be studied and optimized. Rheological measurement in lab allow simulation of the real coating conditions in terms of the applied shear force and drying conditions after coating with the aim to achieve a uniform and reproducible composite electrode. Finally the effect of different component of the CP in the composite positive electrode needed to be studied to optimize the amount of CP binder required for better performance of the coatings.

2 Theory

2.1 Functions of binders in composite electrode

2.1.1 Processing of the electrodes

Composite electrodes are produced by slurry processing technique. In this process active material, conductive additive and binder are mixed in a solvent to obtain a slurry. This slurry must have specific flow characteristics for better mixing of the components of the slurry and for avoiding settling of the active materials during the coating process. It is difficult to disperse the active material and carbon additives, due to their large surface area and presence of attractive van der Waals forces. Hence, flocculation of the particles causes agglomeration and settling of active material in the final coating. In order to avoid this, particles must repel each other to stay in the dispersed state in the slurry. This can be achieved by electrostatic or steric stabilization. In electrostatic stabilization the particle surface is charged and particles repel each other dispersed state is stabilized. On the other hand, steric repulsion is provided by layers of adsorbed polymer binders on the active material. It has been shown that $LiCoO_2$ particles shift from attractive force to repulsive force by addition of poly (ammonium acrylate) (PAA-NH_4) or carboxymethyl cellulose (CMC) binder (13, 14). CMC also acts as a dispersant for $LiFePO_4$ and graphite particles (15, 16). In case of non-aqueous solvent, the principle of attractive and repulsive forces remains the same and the binder can modify the surface.

2.1.2 Electronic and ionic conductivity of the electrodes

The electronic and ionic conductivity of the composite electrodes are controlled by the type and amount of binders. The binder controls the distribution of conductive additive and active material throughout the composite electrode. The electrical conductivity of the electrodes depends strongly upon the distribution of active material and the distribution of carbon additives around the agglomerates. It was also shown that the electronic transport occurs by tunnelling mechanism through the insulating polymer

layers in between the conducting carbon black (17). Hence the type and amount of polymer influence the conduction of electron.

The ionic conductivity of the composite electrode and its electrolyte uptake depends on binder content and the interaction of the binder with the electrolyte (18). Polar binders such as poly(vinylidenfluorid) (PVDF), poly(methyl methacrylate) (PMMA), and carboxymethyl cellulose (CMC) improve the wettability of the electrode more as compared to the non-polar ones such as styrene-butadiene rubber (SBR) or polyethylene. It has been shown that higher Li^+ ion conductivity in a $LiCoO_2$ composite electrode enhances its electrochemical performance (19). Furthermore, the ionic conductivity of the electrodes also depends on its porosity (20). The amount and type of binder can influence the porosity of the composite electrodes and thus affect the ionic movement through the composite electrode (21).

2.1.3 Mechanical properties

The original function of the binder is to provide cohesion of the composite electrode and adhesion strength to the current collector (17). These properties can be studied by means of tensile test and peel test, respectively. The amount and type of binder has a great influence on both, cohesion and adhesion properties of the composite electrode. Babinec et al. studied the failure mechanism of PVDF and $LiCoO_2$ electrodes and showed that, tensile strain at break is less than 2 % and the stress relieving mechanism of the composite electrode is the delamination of particles from the PVDF matrix (18). Porcher et al. measured the adhesion between the composite electrode from the current collector for CMC and SRB binder system. They found a correlation between adhesion strength and the calendaring pressure applied to the coating for improving the contact resistance and the adhesion strength (16).

2.1.4 Lifetime

The cycle lifetime of a composite electrode depends on its structure and its mechanical properties. For better lifetime the electrode must have a high cohesion and adhesion strength with the current collector. The homogeneity of the components and carbon black distribution has a great influence on the cycle life of the composite electrode. If the conductive additives are not uniformly distributed, the utilization of the active material is not uniform and they experience unequal potential distribution (22-25).

Hence some active material degrades due to overcharge or over-discharge. The loss of contact between conductive additive and active material is also a cause for capacity fade.

2.2 State of the art binders for lithium ion battery

2.2.1 Binders for positive electrodes

PVDF and poly(tetrafluoroethylene) (PTFE) are the most widely adopted binders for composite electrodes. They show chemical stability up to 4.5 V and have good mechanical properties and electrolyte absorption. However, they can only be dissolved with NMP solvent. As already mentioned, NMP is expensive, exhibits flammable vapours, and is highly toxic. The allowable limit in air is 20 ppm (26). The flammable vapours of NMP require all processing equipment during the production of electrodes to be explosion proof, this increases the capital cost of such equipment considerably. Although the binding strength of PVDF is high it has a low flexibility. In addition to that fluorine-based polymers produce harmful HF due to decomposition of fluorine hydrogen bond. Hence, a new trend is the substitution of the PVDF with alternative water-soluble binders. Water-based systems have many advantages such as low cost, low impact on environment by release of harmful processing chemicals and no requirement of strict control of processing humidity (27). However a number of issues need to be addressed before moving to water-based binder system. They include the instability of the positive electrode in water, studying the flow behaviour of the slurry, film processing and robust drying procedure to limit the remaining water to ppm level. Different positive electrode active materials such as $LiCoO_2$, $LiFePO_4$, and lithium nickel manganese cobalt oxide (NMC) have been processed with water-soluble binders for coating preparation.

$LiCoO_2$ has remained the most common material for commercial lithium ion batteries since its discovery (28-30). When $LiCoO_2$ is used as an active material, the use of water based binder meets several challenges. It has a significant dissolution rate with water; and it is very difficult to control the dispersion properties of $LiCoO_2$ (31). However, if the pH of the water based slurry with $LiCoO_2$ and CMC binder can be controlled, higher dispersion homogeneity and cell performance can be achieved (32). Trna et al. (33) reported thick electrodes with active mass loading of 30 mg cm^{-2} using

polyethylene glycol (PEG) based binders. They achieved a high columbic efficiency of 98.7 %, indicating aqueous binder can be a good choice for $LiCoO_2$ based system.

CMC has been used as a slurry thickener with $LiFePO_4$ as active material. Porcher et al. (15) showed that $LiFePO_4$ ages slightly when brought in contact to water. The flow behaviour of CMC and hydroxypropyl methylcellulose (HPMC) based slurries for $LiFePO_4$ as an active material has been also studied. It is found that, there is no settling of active material with CMC based slurry, suggesting that its flow behaviour is appropriate for good coating conditions. Lee et al. (34) used PAA with CMC for $LiFePO_4$ slurries. It reduced the viscosity and improved discharged capacity in terms of volumetric density. Lux et al. (35) reported enhanced rate capability when using CMC as a binder as compared to conventional PVDF system.

Lithium nickel manganese cobalt oxide (NMC) is a promising commercial positive electrode material with advantages such as high operating voltage, high specific capacity, high cyclic stability and structural stability. It has been seen that CMC based binder shows better rate capability than PVDF based system with NMC positive electrodes. The reason mentioned is the lower activation energy of the electrodes with CMC as a binder facilitates the transport of lithium ions compared to electrodes with PVDF as binder (36).

2.2.2 Binders for Negative electrodes

The most common carbon material used for negative electrodes in lithium ion battery is graphite. CMC is first proposed by Lee *et.al.* (37) as a water soluble binder for graphite composite electrode. It is found that CMC could lead to good adhesion with high capacity retention of up to 90 % for 200 cycles. It is also proposed to be used with acetylene black to improve the electrical contact between graphite spheres during long term cycling (38). Moreover, CMC has been used for commercial negative electrodes for lithium ion batteries; one of the examples is from Ashland Company Bondwell BVH9 CMC.

In case of conventional PVDF based binders for graphite, it has been found that the distribution of the binder is very non-uniform compared to CMC-based slurries. One of the reasons is the slower evaporation rate of NMP compared to water. Hence, a longer drying time is required for NMP-based slurries and migration of binder to the top of the coating takes place (39). Chong *et al.* (40) showed that for spherical graphite,

lithium poly(acrylic acid) (PAALi) and sodium poyl(acrylic acid) (PAANa) binders show better cell performance in terms of capacity and columbic efficiency than PVDF binder because of a more suitable conformation of the polymers in the composite structure. A more stable and effective SEI is formed with lower number of cycles for PAALi and PAANa than PVDF. Although PAA based coatings are brittle, styrene butadiene rubber (SBR) (0.5-3%) can be added to make it flexible.

Si is one of the promising materials for lithium ion battery negative electrodes due to its abundance in nature and inherent very high capacity of 3579 $mAhg^{-1}$. However, achieving cycling stability represents a grand challenge due to large volume expansion of up to 270 % after lithiation (41, 42). Hence it is very difficult to form a stable SEI for these negative electrodes. An effective binder material will play an important role to bring Si negative electrodes to a commercial use. Buqa *et al.* (43) showed that, 1 % CMC based binder has the same cycling performance as compared to a 10 % PVDF binder composition. Li *et al.* (44) proposed that the stability of SEI can be enhanced by modification of surface of the negative electrode by CMC binder.

Conducting polymers as a special class of polymers exhibit flexibility of a polymeric structure and has high electronic conductivity. They can be interesting as additive in composite electrodes. Several study have been dedicated to the understanding of their use in lithium ion batteries as described in the review paper (45).

2.3 Conducting polymers

Materials can be divided into 3 categories with respect to their electrical conductivity such as insulators, semiconductors and conductors. In general a material having a conductivities of less than 10^{-7} S cm^{-1} is regarded as insulator, a material with conductivity larger than 10^{3} S cm^{-1}, such as metals, is regarded as conductor, and a material for which the conductivity is in the range 10^{-4} to 10 S cm^{-1} is called a semiconductor. Plastics or organic polymers with saturated macromolecules are very good insulators. Metals are conductors and silicon, germanium are the example of semiconductors.

However a conducting polymer has been established since discovery of polyacetylene (PA) doped with iodine. MacDiarmid, Shirakawa and Heeger have received the Nobel Prize in 2000 for this discovery (46, 47). The structure of PA is shown in the Figure 2.1a. It has an alternating sequence of single and double bonds

which is called as π-conjugated system. The electrons in the π bonds are more mobile than in the σ-bond. This is the major reason for the conducting nature of PA. After the discovery of PA, many more π-conjugated conducting polymers have been reported such as polyaniline (PANI), polythiophene (PT) (Figure 2.1b, 2.1c). The bandgap of the conducting polymers are estimated to be in the range of 1 to 3 eV from their electronic absorption spectra. This range of bandgap corresponds to their semiconducting behaviour. But with doping processes their conductivity can rise up to the level of metals.

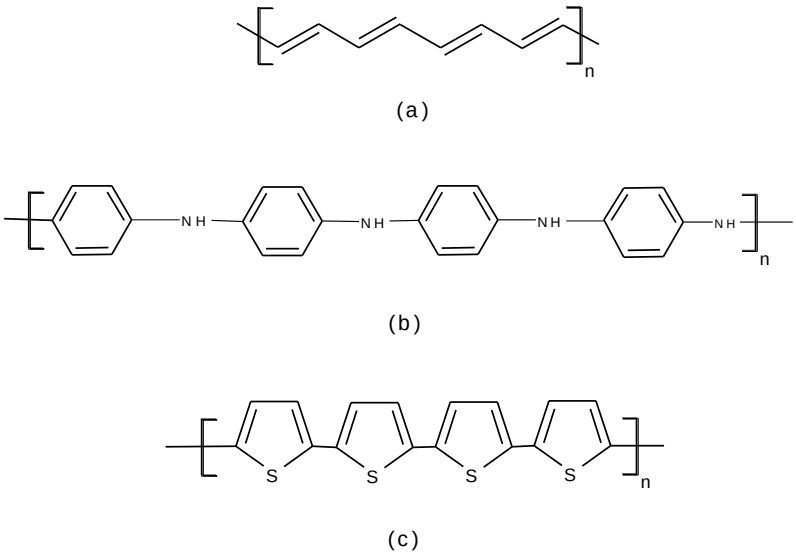

Figure 2.1. Molecular structure of PA (a), PANI (b), PT(c).

2.3.1 The doping process in conducting polymers

The transition of π-conjugated polymers from insulator to metal like conductivity has been achieved by a doping process. However, the doping process in polymers is very different to the doping process of conventional semiconductor. It can be explained as follows,

1. Intrinsic doping process in a polymer is an oxidation (p-type) or reduction (n-type) process, unlike an atomic replacement in inorganic semiconductors. Taking PA as an example, oxidation and reduction process can be written as

$$[\mathrm{CH}]_n + 1.5x\,\mathrm{I}_2 \rightarrow [\mathrm{CH}]_n^{x+} + x\mathrm{I}_3^- \qquad 2.1$$

$$[\mathrm{CH}]_n + x\mathrm{Na} \rightarrow [\mathrm{CH}]_n^{x-} + x\mathrm{Na}^+ \qquad 2.2$$

2. The p-doping or n-doping of the conjugated polymer can be accomplished by incorporation of counter ions in the structure. The counter ions used are anions for p-doping and cations for n-doping. In case of PA iodine, molecules take up electron from the polymer chain to become I_3^-. PA molecule is now positively charged and I_3^- is the counter anion associated with the molecule to make the system electrically neutral. In case of conventional inorganic semiconductors there is no counter-ion present in the structure.
3. The π-conjugated polymers can be converted to the conducting state by chemical or electrochemical doping. This process can be reversed (de-doping) to return to the original state. Hence, a reversible doping and de-doping process can be obtained in conjugated polymers, which is not possible in inorganic semiconductors.
4. The doping percentage in conducting polymers can be as high as 50 % where as in case of inorganic semiconductors it is very low (48). The mobility of charge careers is very low in case of the polymer system due to presence of defect as a result of the amorphous nature of polymers.

2.3.2 Charge carrier and conduction mechanism

Charge transfer mechanism of PA and PT are described using the doping mechanism. For PA it can be seen in the schematic (Figure 2.2) that p-type doping creates a polycarbonium cation and attracts an anion to stabilize the structure. Positive charges of polycarbonium cations are mobile. Removal of a second electron gives rise to another radical cation and the two cations combined together gives a spineless dication or soliton. They are the main charge careers in the PA structure (49, 50). These solitons can move around the PA backbone carrying only charge and no spin. If an electron is added or removed from the anion, a neutral radical soliton is re-established (51).

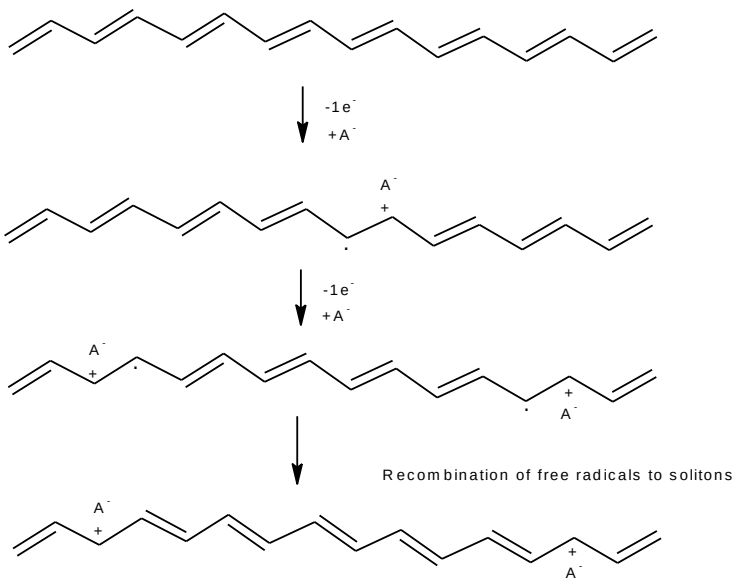

Figure 2.2. Charge conduction mechanism of PA.

In case of cyclic heteroconjugated polymer system such as poly(3,4-ethylenedioxythiophene) (PEDOT) which is a polymer of the polythiophene family, a different mechanism occurs for charge transfer (Figure 2.3). The removal of electrons proceeds with a formation of a cation which is called a polaron. A quinone type bond sequence is created due to presence of the polaron. The removal of another electron leads to the formation of another polaron or a spinless bipolaron. This bipolaron separates quinone-type bond from the aromatic structure. In case of polythiophene, formation of polarons and bipolarons are the mechanism of charge transfer (52).

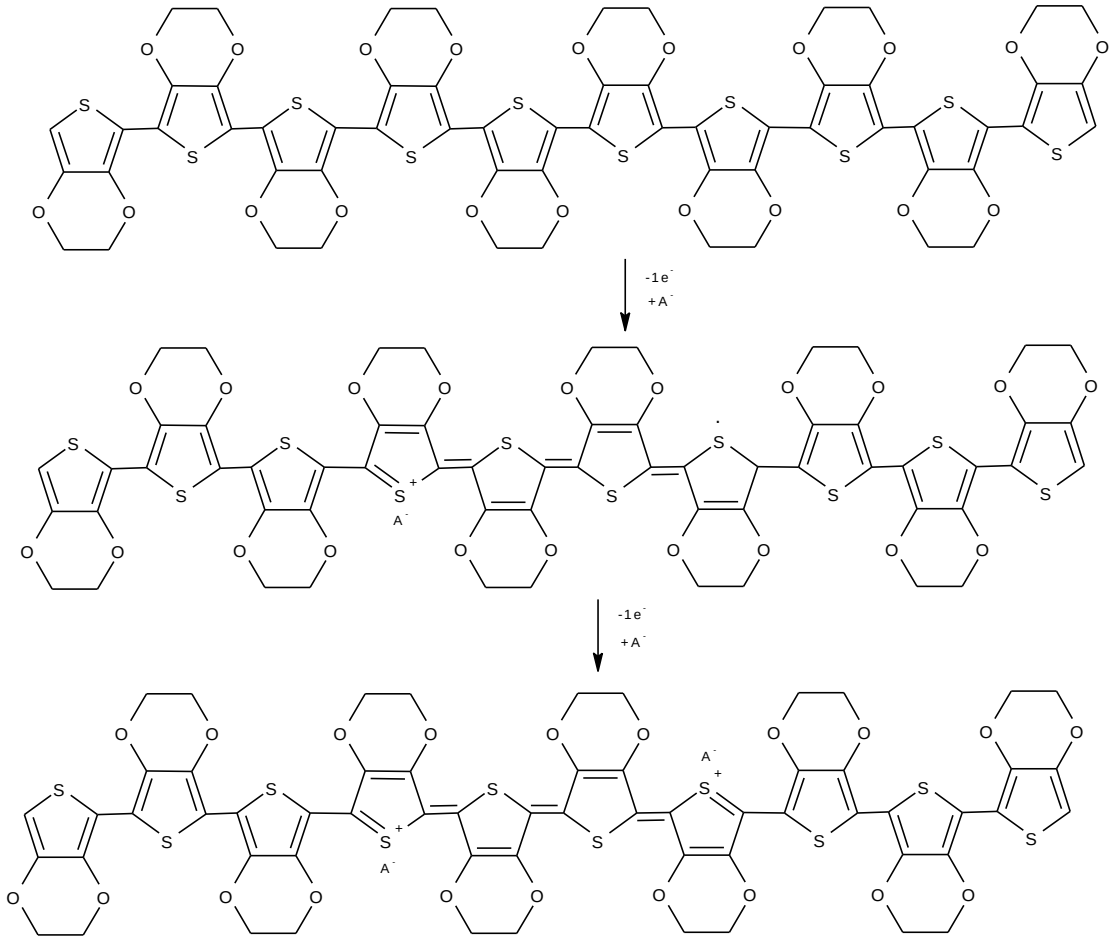

Figure 2.3. Charge conduction mechanism of PEDOT.

2.3.3 Polyaniline

Among conducting polymers, polyaniline is one of the most attractive due to its environmental stability, controllable electrical conductivity and interesting redox properties (53). The structure of PANI was first shown by MacDermid et al. (54). They proposed the general formula for PANI which is shown schematically in Figure 2.4. They can be categorized as three redox states depending on the level of oxidation of PANI. The completely reduced form Figure 2.4a is known as leucoemraldine base and the completely oxidised form (Figure 2.4c) is called pernigraniline form. The semi-oxidized form (Figure 2.4b) is called emeraldine base.

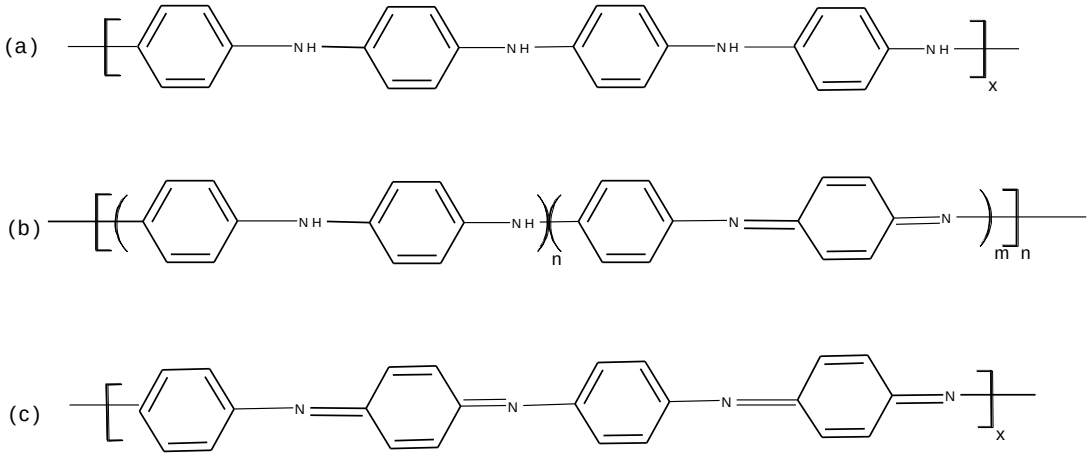

Figure 2.4. Structure of different oxidation state of PANI. (a) leucoemraline, (b) emeraldine, (c) pernigraniline.

Emeraldine base (EB) can be doped with a proton (1 mol L^{-1} HCl) to obtain a highly conducting salt called emeraldine salt (ES). As shown in the Figure 2.5, it does not change the number of electrons associated with the polymer backbone. Thus proton doping is a major characteristic difference of PANI to other conducting polymers. The proton doping process can be summarized as following,

1. Proton doping selectively takes place in the imine segment of the PANI chain.
2. The protonation process is a fast chemical reaction of the proton with nitrogen in the imine segment accompanied by a slow diffusion process of counter ions from aqueous solution to the polymer.
3. The protonation state of ES should be considered in the molecular structure as partial protonated state. Hence the molecular structure of protonated PANI should be determined both by the oxidation and the protonation states.

Depending on the type of acid used, the ES can have different counter ions. Several doping medium have been used for PANI such as HCl, H_2SO_4, $HClO_4$, HNO_3, H_3PO_4. Accordingly, different counter ions will be associated with the structure such as Cl^-, SO_4^{2-}, ClO_4^-, NO_3^-, PO_4^{3-} (55). Apart from protonation, PANI can also be p-doped or n-doped by charge transfer using an oxidizing or reducing agent, which increases its conductivity (56, 57).

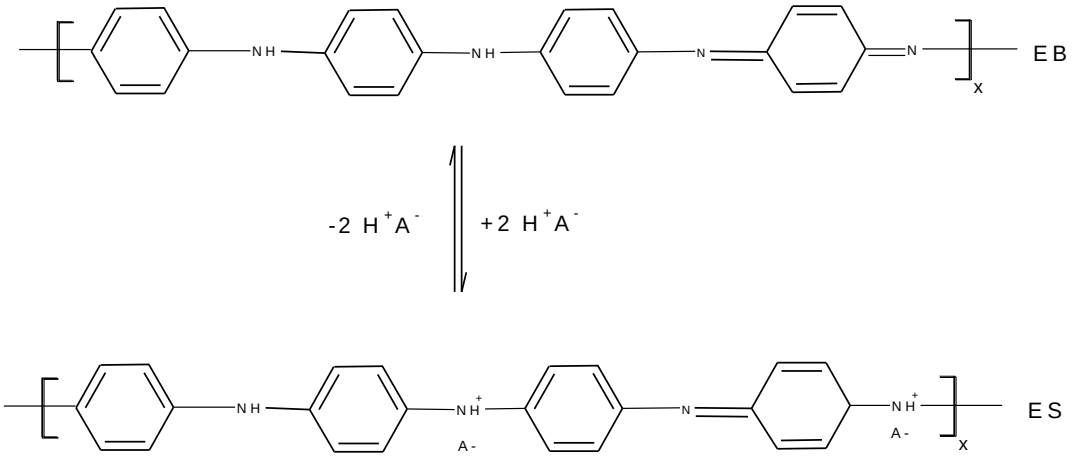

Figure 2.5. Schematic of protonation mechanism of emeraldine base to emeraldine salt.

Chemical synthesis method: PANI can be synthesized chemically or electrochemically. The chemical synthesis of PANI is shown in the Figure 2.6. Emeraldine salt is prepared from aniline by using an oxidant in a strong acidic medium (1 mol L^{-1} HCl). Then the salt is treated with NH_4OH base to obtain emeraldine base.

At first, radical cation is formed from the aniline monomer due to the oxidation, loss of electrons, of the respective monomers by ammonium persulphate (Figure 2.6). The radical cations can exist in four resonant forms as depicted in Figure 2.6. The second stage of the polymerization is the production of a dimer by the head to tail coupling of two radical cations (Figure 2.6). The dimer is itself oxidized to a dimer cation at lower potential than the monomer. Thereafter, the dimer cation can react with another monomer cation to form a trimer, which in turn also undergoes oxidation. Further head to tail couplings promote the chain propagation and thus the polymerization into a long chain PANI. Inevitably however, branching occurs as the cations do not only react with the tail ends but also with other sites of the polymer chain.

$$\text{Aniline} + \text{Dopant} \xrightarrow{\text{Oxidant}} \text{PANi (BS)} \xrightarrow{\text{NH4OH}} \text{PANI (EB)} \qquad 2.3$$

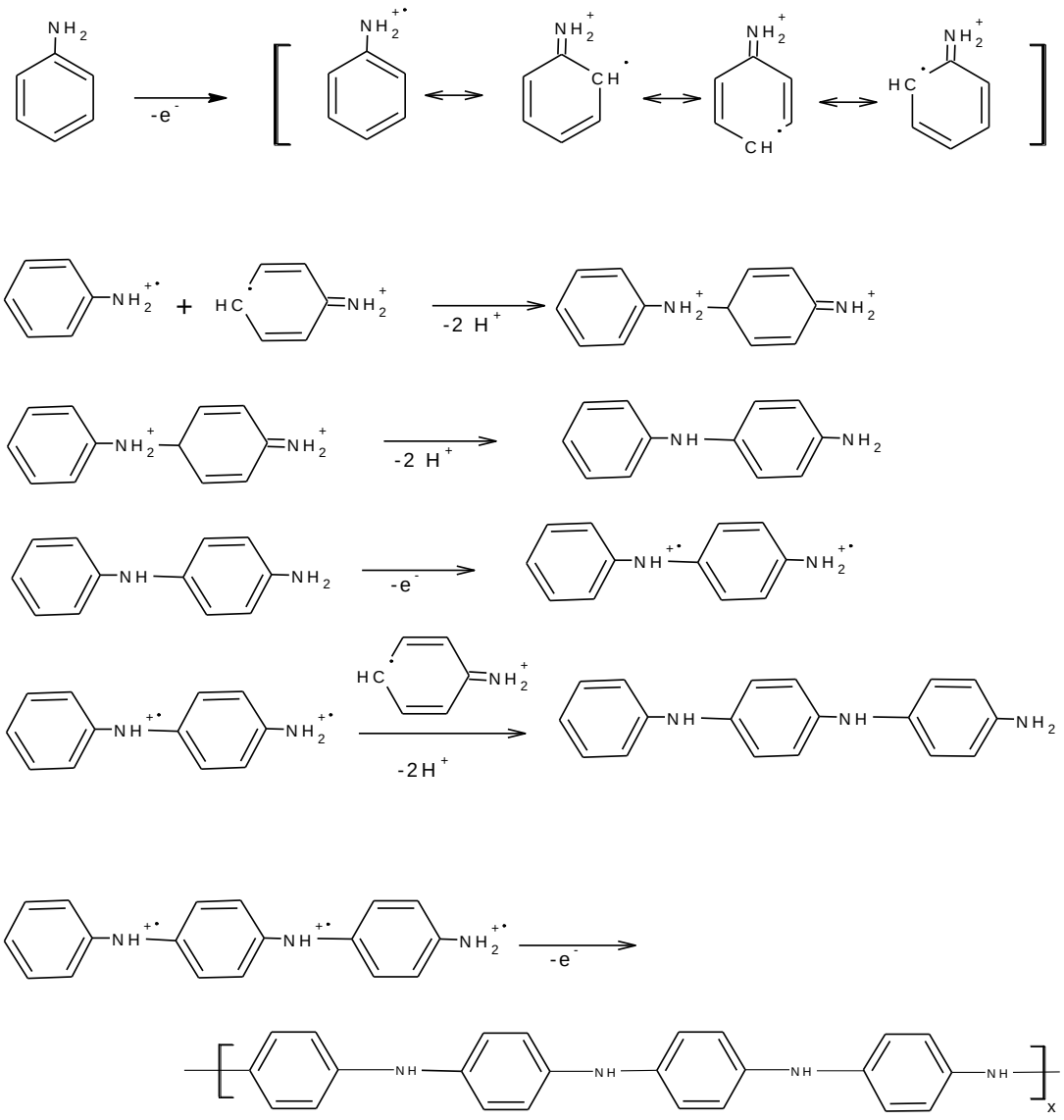

Figure 2.6. Schematic representation of PANI polymerization.

Physical properties: EB form of PANI is soluble in NMP and free standing coatings can be prepared from this solution. But ES is not soluble in NMP. Hence processing of PANI is an issue. Several reports have been dedicated to study the solubility enhancement of PANI (58-61). One possibility is the incorporation of a side chain or group into the polymer chain. Poly(ortho-methoxy-aniline) (POMA) is an example, where the methoxy group is attached to the ortho-position of the monomer (60).

As mentioned before, the insulating state of PANI EB can be proton-doped to obtain the conducting state of PANI. The ES form has a conductivity of 10 Scm^{-1} which is up to 10 orders of magnitude higher than PANI (62). Localized conductivity of PANI

can be affected by the localized variation of thickness, stoichiometry and defect levels (63, 64).

2.3.4 POMA

As described in the previous sections, POMA is a derivative of PANI (Figure 2.7). The oxidative polymerization process of POMA is very similar to that described for PANI. Due to the presence of the methoxy group at ortho position, no position in the ring structure is highly activated. Therefore a linear polymer is formed rather than a highly cross-linked polymer (60). The oxidation state and proton doping mechanism of POMA are very similar to those of PANI. However, POMA is more soluble in organic solvents than PANI. This is due to substitution of flexible methoxy group in the PANI chain, which reduces the stiffness of the polymer backbone and also increases the polarity of the polymer chain. The disadvantage of the presence of the substituent on the PANI chain is the steric effect caused by them, which can result in twisted chains, that decreases the electrical conductivity of the polymer (65, 66). Nevertheless, POMA is very attractive for industrial applications due to its solubility, stability in air and highly mono-disperse nature.

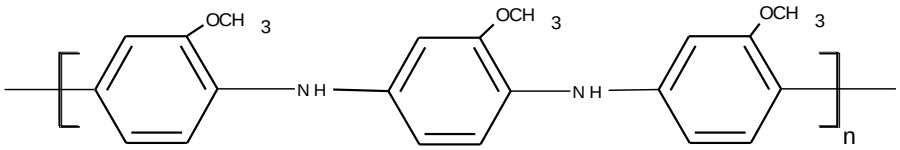

Figure 2.7. Structure of POMA.

2.3.5 PEDOT

Conductive polythiophenes were successfully synthesized by Garnier and Tourillon fundamental work (67). However, the doped bipolaron state did not show any long-term stability in air and moisture. They have only a low solubility in common solvents such as ketones or halogenated hydrocarbons. Hence technical applications of polythiophene are not possible.

Oxygen substituents at the 3- and 4-positions in the thiophene moiety could stabilize the doped, bipolaronic state in polythiophenes by their electron donating properties (68). The monomer is called 3,4-ethylenedioxythiophene or EDOT. The polymer is called PEDOT (Figure 2.8). It is known to possess a high conductivity,

stability in air and up to 250 °C. This has led to several technical application of the compound.

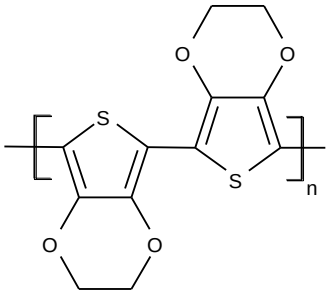

Figure 2.8. PEDOT structure.

Synthesis: PEDOT can be synthesized by chemical polymerization technique by oxidizing the EDOT monomer with an oxidizer and conducting a radical polymerization. Radicals combine with more radicals to form dimers. The dimer can be oxidized followed by coupling with monomer to trimers. This chain continues until a termination reaction occurs. This process is shown in the Figure 2.9.

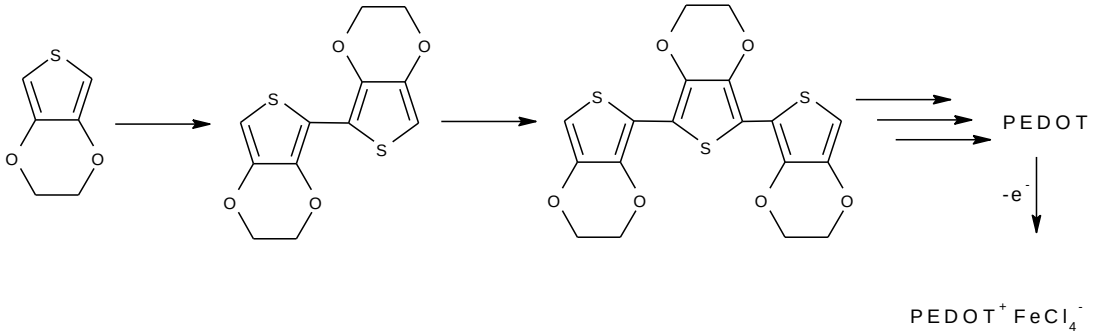

Figure 2.9. Polymerization process of PEDOT.

Counter-ions for PEDOT: Counter ions are present in all oxidized state of PEDOT for charge balance. The type of counter ion affects the properties of the polymer. In case of chemical polymerization, the oxidizing agent is typically a salt. Therefore, the counter ion for the polymer comes generally from the oxidizing agent used. If additional counter ions are added to the reaction mixture during synthesis, PEDOT with mixed counter ions is formed. Jonas and Heywang (68, 69) have used different oxidizing agents such as iron(III) chloride, iron(III) tosylate, or ammoniumperoxodisulfate for polymerization of EDOT. These oxidizing agents result in chloride, tosylate and sulphate counter ions respectively. Iron(III) tosylate is soluble in organic solvents like alcohol, hence tosylate

counter ion PEDOT polymers can be produced easily and show conductivities as high as 1000 S cm^{-1} (70). But the solubility of these counter ion-based polymers in common solvents like alcohol or water is very low. Hence industrial application is limited for these polymer systems.

Polystyrene sulfonic acid (PSS) is the most prominent counter ion for PEDOT because of the formation of the polyelectrolyte complex PEDOT:PSS in water. Hence it can be used industrially for preparation of coatings. For the synthesis of PEDOT:PSS, chemical polymerization is performed with iron (III) sulphonate as oxidant and PSS is added to the reaction mixture. At the end the produced polymer contains a mixture of counter ions of PSS and sulphate. However the sulphate ions can easily be replaced by PSS during an ion exchange process and a true PEDOT:PSS complex can be prepared (71). The structure of PEDOT:PSS is shown in the Figure 2.10. It shows a high temperature stability up to 200 °C and high electrical conductivity in the range 0.1-100 S cm^{-1} (68).

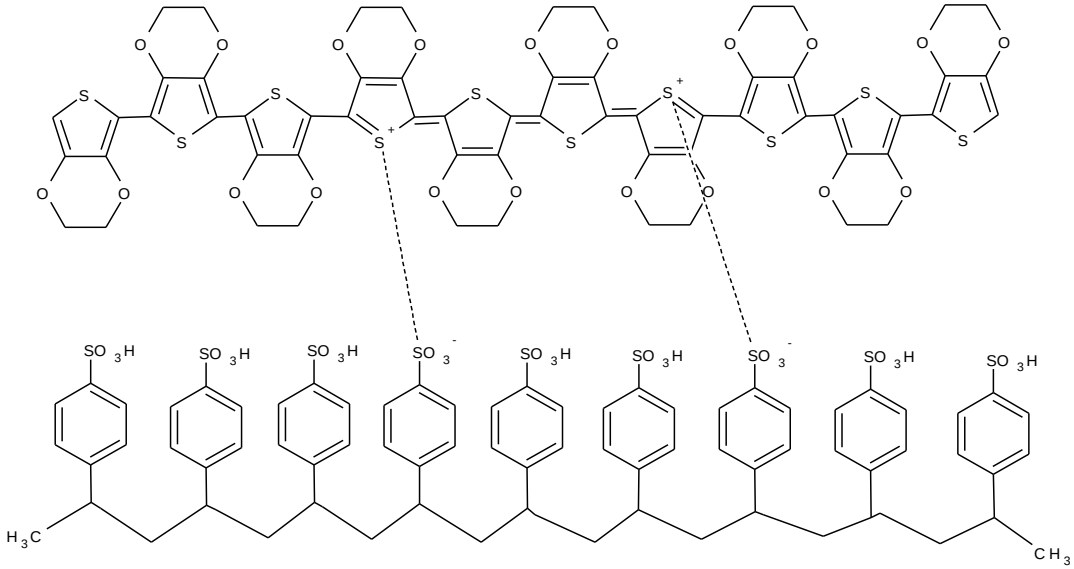

Figure 2.10. Structure of PEDOT:PSS.

2.4 Conducting polymers in lithium ion battery

Conducting polymers have been used as active material for lithium ion batteries in the early 90s (45, 72). It has been reported that PANI exhibits good specific capacity of up to 140 Ah kg^{-1}, low self-discharge and high rate capability when used as a positive electrode material in the voltage range 1.5 to 4 V vs. Li/Li^{+} (73, 74). Electrodes made of

PT and its derivatives in aprotic lithium ion containing electrolytes corresponds to a moderate specific capacity of 50 Ah kg^{-1} (45, 75). However, there are only a few studies of the redox behaviour of PANI and PEDOT in aprotic electrolytes (76, 77). It is shown that reduction reaction in aprotic lithium ion containing electrolyte occurs at potential more negative than 2.5 V vs. Li/Li^+ for PEDOT doped with BF_4^- counter ions. PEDOT itself is not redox active in the positive electrode operating window up to 4 V vs. Li/Li^+ (76). The commercial application of electrodes with conducting polymers alone as active material in lithium ion batteries failed due to their low stability and moderate specific capacity in comparison to layered metal oxides and other inorganic positive electrode materials such as $LiCoO_2$ and $LiFePO_4$. In recent years several studies have shown that surface modification of $LiFePO_4$ and $LiCoO_2$ with nanometer coatings of conducting polymers such as PANI and PEDOT can improve significantly the capacity and the rate capability of the positive electrodes (78-87).

Recently, it was shown that the addition of polypyrrol (PPy) binder in the positive electrodes of lithium ion batteries leads to enhanced electrode capacities and better rate capabilities (88, 89). PANI has been also successfully used as a binder material with $LiFePO_4$ and V_2O_5 active materials (90, 91). It has been observed that conductive polymer binders provide conductive bridges between individual particles which can improve the electron transport within the electrode (92). Furthermore, PEDOT:PSS has also been proposed as a binder for mesocarbon composite negative electrodes for lithium ion batteries causing significant capacity retention at higher charging rates (93). Recently, PEDOT:PSS has been used also for composite positive electrodes free of any carbon additives and improvement in capacity and rate capability of the system is observed (94). Hence the effort in recent times is to use conducting polymers together with the inorganic active materials. In this case the mixing and flow behaviour of the composite mixture produced by these elements should be understood and optimized in order to be able to convert the potential advantages into improved device performance.

2.5 Composite electrode processing

As mentioned in the introduction chapter, composite electrodes consist of active material, conductive additive and polymeric binder. They are generally prepared by slurry processing technique. In this method all, the components are dispersed in a

solvent and mixed thoroughly to a produce slurry with high solid loading. The uniformity of the slurry can be studied from its rheological behaviour. It strongly depends on the sequence of mixing, solution preparation, mixing devices and operating conditions (24, 95-97). Before moving on to discuss the coating behaviour of the slurry, it is important to understand the flow behaviour of the slurry i.e. the rheological behaviour of suspensions.

2.5.1 Rheological behaviour of fluids

Rheology is the study of flow behaviour caused by deformation. There are two types of flow with respect to adjacent particles in a liquid, shear flow and extensional flow. In shear flow, liquid elements flow over each other whereas liquid elements flow towards or away from each other in extensional flow. A schematic is shown in the Figure 2.11. All flows are resisted by viscosity of a fluid. Viscosity is essentially internal friction of the fluid. A body incapable of flow has infinite friction, whereas gas flows readily as its internal friction is small. Liquids are in between solid and gas. The study of flow or rheology provides information about the internal structure of a fluid system. Conversely by controlling the internal structure, flow of desired quality can be obtained.

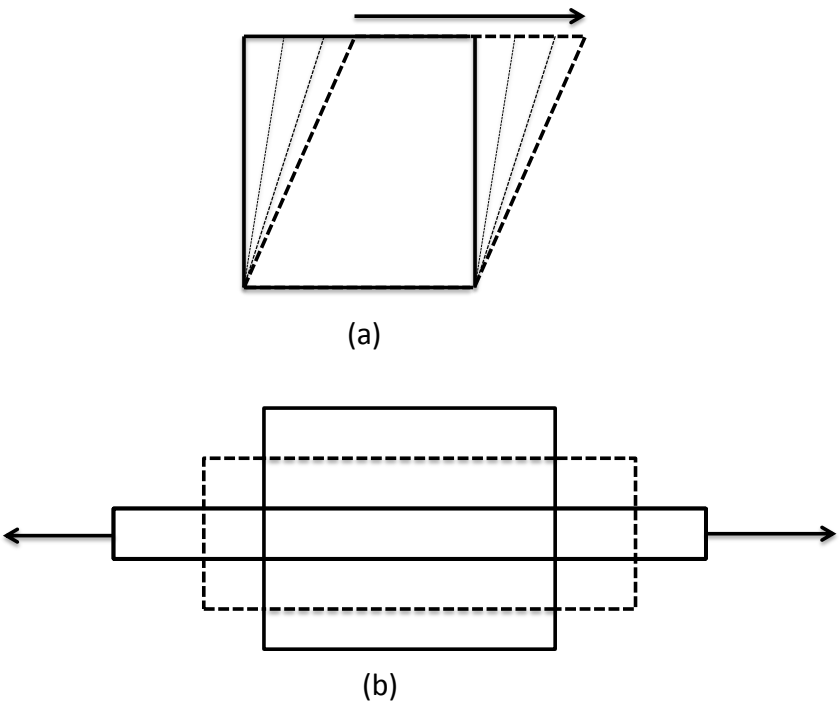

Figure 2.11. Motion of fluid elements in shear (a) and extensional flow (b).

Shear rate and shear stress: As previously mentioned, shear flow corresponds to the flow of liquid elements over each other. Fluid movement may be compared to a large number of platelets moving parallel to one another at different velocities (98, 99). It is shown schematically in Figure 2.12.

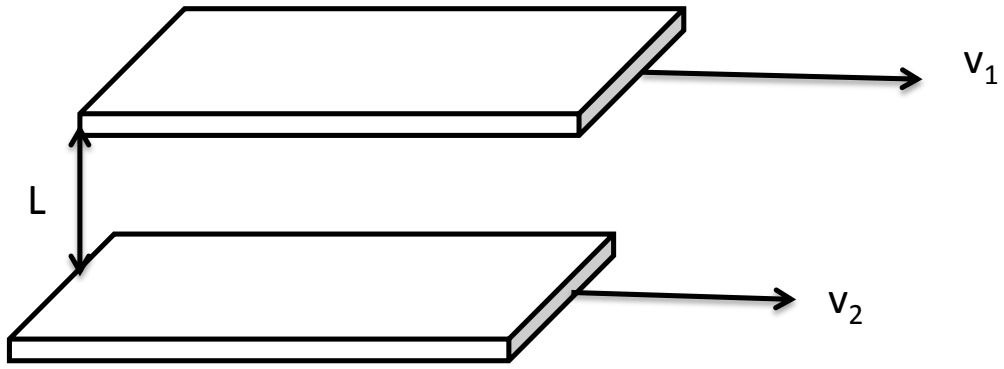

Figure 2.12. Motion of two fluid element separated by distance *L* in shear flow.

In this simple geometry, the velocity of the fluid varies linearly from one layer to another. The shear rate or the gradient of velocity can be expressed as,

$$\text{Shear rate} = \frac{\text{velocity difference between two layers}}{\text{Distance between two layers}}$$

$$\frac{dv}{dx} = \frac{v_1 - v_2}{L} \qquad 2.4$$

Where v_1 and v_2 are the velocity of the two layers and L is the distance between the two layers. The unit of shear rate is,

(Length × time^{-1})/ Length = time^{-1}

It is expressed as $\dot{\gamma}$.

The force applied to the top layer caused shear force expressed as τ.

$$\tau = \frac{F}{A} \qquad 2.5$$

The viscosity (η) of a fluid is the ratio of the shear stress, τ, to the shear rate $\dot{\gamma}$.

In SI unit, it is expressed as Pascal × sec (Pa.s).

$$\eta = \frac{\tau}{\dot{\gamma}} \qquad 2.6$$

Newtonian fluid: A Newtonian fluid is one for which the viscosity although varying with temperature and pressure does not vary with deformation rate or time; nor does such a liquid display any elastic properties or extensional anomalies. The behaviour is shown in the Figure 2.13. It can be seen that the slope of a plot of the shear stress versus shear rate is constant, i.e. the viscosity is constant. The fluids which show Newtonian

type behaviour are normally liquids with low molecular weight. e.g., water, gasoline, silicon oils.

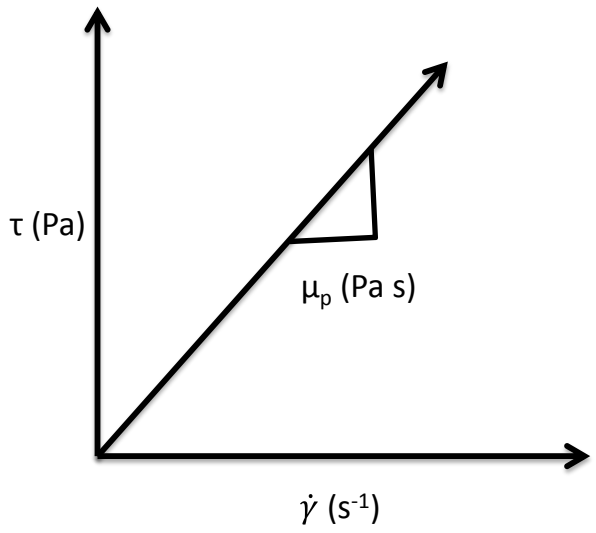

Figure 2.13. Shear stress vs. shear rate curve in a Newtonian fluid.

Non Newtonian fluid: Unlike Newtonian fluid, non-Newtonian fluids show a dependence of the viscosity depends on shear rate and time. Hence the shear stress versus shear rate curve does not go through the origin. A certain stress level must be overcome before the fluid starts to flow. Moreover, a non-Newtonian fluid behaves like a solid in the absence of any shear force. The behaviour of non-Newtonian fluid has been described by different models. Bingham plastic model (98) is shown in the equation 2.7, 2.8.

The two parameters described by Bingham model are

1. The value of τ is τ_0 when $\dot{\gamma}$ is zero.
2. The slope of straight line is known as plastic viscosity and described as η_p.

$$\tau = \tau_0 + \eta_p \dot{\gamma}\,, \tau > \tau_0 \qquad 2.7$$

$$\dot{\gamma} = 0\,, \tau \leq \tau_0 \qquad 2.8$$

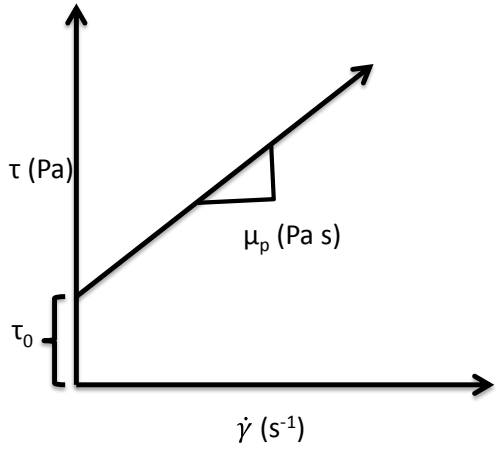

Figure 2.14. Shear stress vs. shear strain curve in Bingham model for non-Newtonian fluid.

Some fluids follow a different type of behaviour expressed as power law behaviour. In these cases, the viscosity is not constant, but rather changes with shear rate (Figure 2.9).

$$\tau = K\dot{\gamma}^n \qquad 2.9$$

K and *n* are power law parameters. *n* represents the flow behaviour index by which fluids can be classified. In case of $n < 1$, it shows pseudo-plastic behaviour (shear thinning behaviour). If $n > 1$, it is dilatant and shows shear thickening behaviour.

A fluid is shear thinning when the apparent fluid viscosity decreases with shear rate. This is shown in Figure 2.15. The viscosity of shear-thickening materials increases with the increase of shear rate (Figure 2.16).

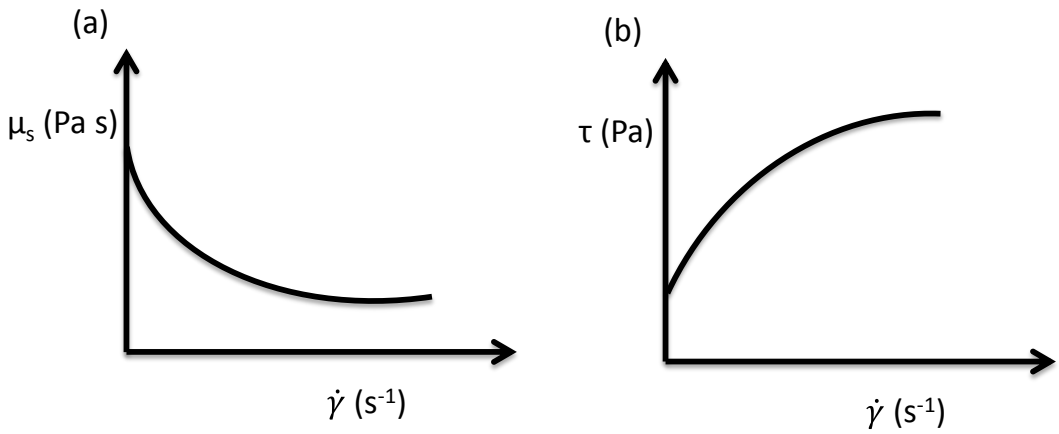

Figure 2.15. Viscosity (a) and shear stress (b) vs. shear strain curve for a shear thinning fluid.

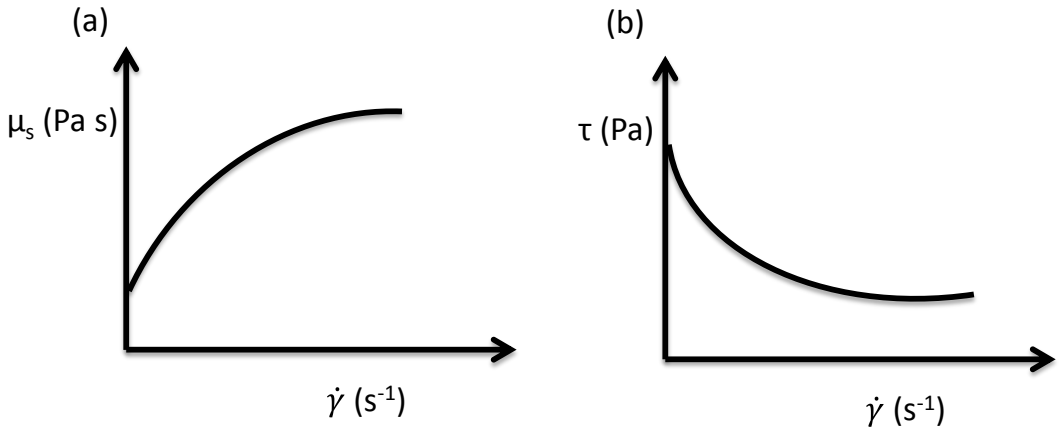

Figure 2.16. Viscosity (a) and shear stress (b) vs. shear rate curve for a shear thickening fluid.

A Herschel-Bulkley fluid combines power-law and Bingham plastic behaviours of fluids through the following formula:

$$\tau = \tau_0 + K\ \dot{\gamma}^n \qquad 2.10$$

Here τ_0 is the yield stress, i.e. the minimum stress required for the flow of the fluid, K and n are power law parameters. The electrode slurry for lithium ion battery follows this model (100, 101).

Linear viscoelastic rheology: Fluids have viscosity which opposes flow. But they do not have any opposition against the deformation. Solids resist deformation due to their elasticity. Most of the engineering fluids like polymer melt, particle suspensions, and emulsions have both elasticity to oppose deformation and viscosity to oppose the flow. Hence they are called viscoelastic fluids. For viscoelastic fluids, deformation behaviour is very much of interest for their application such as coatings and mouldings. The deformation of a viscoelastic fluid is more like a deformation of spring. When these liquids are deformed, thermodynamic forces immediately begin to operate to restore this rest state just like in spring. Also like a spring, movement from the rest state represents storage of energy. This kind of energy is the origin of elasticity in structured liquids. Alongside these elastic forces the viscous forces are present due to the dissipation of energy proportional to the rate of deformation not to the extent of deformation.

Viscoelastic behaviour can be emulated by a simple mechanical model combining a pure elastic spring and pure reservoir of viscos fluid together i.e. springs and dashpots (Figure 2.17). A spring is a liner elastic element and follow Hooks law. So the strain is proportional to the applied stress.

$$\sigma = G\gamma \qquad 2.11$$

Where G is the modulus and γ is the strain. It can be noted that there is no term of time. Hence with application of strain γ to the unstrained model, the resultant stress σ suddenly appears, and then, if the strain is removed, the stress σ falls immediately to zero. For a dashpot model where the fluid only shows viscous behaviour the stress stain behaviour can be explained with equation 2.11. Hence in case of viscous liquid the fluid immediately starts to deform with shear rate of $\dot{\gamma}^n$ when stress τ is applied. Once the stress is removed, the deformation stops (Figure 2.17).

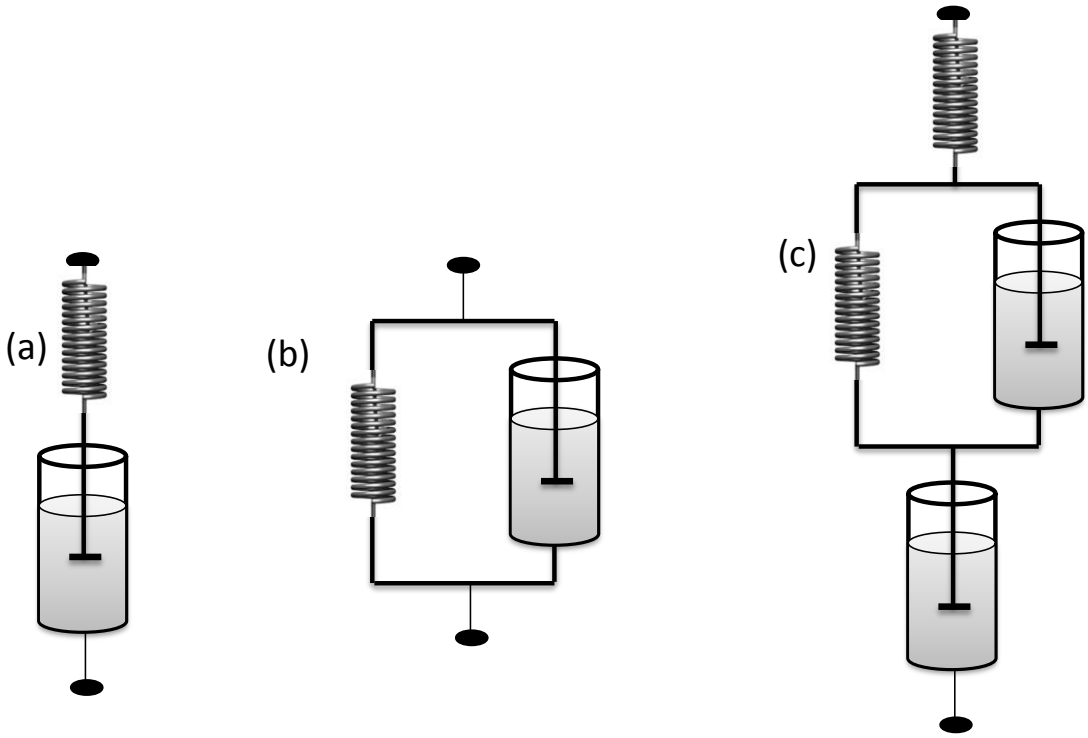

Figure 2.17. Schematic of different spring and dashpot models to represent viscoelastic fluid.

Figure 2.17 shows a spring model connected to a dashpot in series. It is known as the Maxwell model. It represents the behaviour of a viscoelastic liquid. Figure 2.17 shows a spring in parallel to a dashpot and called Kelvin-Voigt model. It represents the behaviour of a viscoelastic solid. Figure 2.18c represents a Maxwell model and a Kelvin-Voigt model in series, the Burgers model. This model is the most complicated since it describes all the basic features of interest for a viscoelastic material.

There are several ways to measure linear viscoelastic behaviour. One of the simplest methods is the sudden application of a constant stress to the liquid being tested and the monitoring of the resulting strain. This is called creep testing. Another frequently used method is oscillatory testing, i.e. applying an oscillating stress or strain

as an input to the liquid and monitoring the resulting oscillatory strain or stress output. Small amplitude oscillatory measurements are of special interest for battery electrode slurries because the slurry coating process can be very well simulated in rheometer instrument and settling behaviour of the active material in the slurry can be studied (15, 100).

Oscillatory testing: In this case a sinusoidal shear strain is applied to the fluid and the shear stress response is measured. To understand the response of a viscoelastic fluid, the response of a spring and dashpot model is considered first separately.

In case of a spring model the applied strain is,

$$\gamma = \gamma_0 sin\omega t \qquad 2.12$$

Where $\gamma_0$the strain amplitude and ω is the angular velocity and is $2\pi f$ where f is the applied frequency, the response is,

$$\tau = \tau_0 sin\omega t \qquad 2.13$$

Where τ_0 is the stress amplitude and the model stress and strain are in phase with each other.

For the dashpot model, one obtains

$$\dot{\gamma} = \frac{d\gamma}{dt} = \omega\gamma_0 cos\omega t \qquad 2.14$$

It can be seen that the shear stress is 90 ° out of phase with applied strain.

$$\tau = \frac{d\gamma}{dt} = \eta\gamma_0\omega cos\omega t \qquad 2.15$$

For the viscoelastic fluid, the two behaviours can be combined. Hence,

$$\tau = \tau_0 sin\omega t + \eta\gamma_0\omega cos\omega t \qquad 2.16$$

This can be simplified as,

$$\tau = G' sin\omega t + G'' cos\omega t \qquad 2.17$$

Where G' is the storage modulus which describes elastic behaviour. And G'' is the loss modulus and describes viscous or fluidic behaviour.

2.5.2 Application of rheology for battery electrode slurries

The binder plays an important role in composite coating preparation. It determines the required flow properties of the composite slurry during electrode fabrication (15, 101,

102). Different binders such as PVDF and CMC have been studied with active material suspensions for their dispersion properties and flow behaviours (15, 101). Porcher et al. (15) proposed design considerations for processing of $LiFePO_4$ positive electrodes with PVDF, CMC and hydroxypropyl methylcellulose (HPMC) as binders. They have found settling of active materials in slurries with HPMC due to their liquid-like flow behaviour, whereas PVDF and CMC binders could inhibit the settling of the active materials yielding a homogeneous structure throughout the cross section of the coating. Ligneel et al. (100) studied the effect of solvent concentration on the properties of slurries and their processing behaviour for $Li_{1.1}V_3O_8$ and poly (methyl methacrylate) (PMMA) binder. They found an optimum solvent concentration of 0.006 mL mg^{-1} for which the resulting electrodes exhibited a maximum performance.

2.5.3 Particle interaction in the slurry suspension

The viscosity of the suspension is changed due to presence of the particles in the solvent. To understand the effect of particles, the relative viscosity term is used. It is the ratio of viscosity of the suspension to the viscosity of the solvent.

$$\eta_r = \frac{\eta}{\eta_s} \qquad 2.18$$

The relative viscosity can be described in terms of Baxter interaction parameter τ_B,

$$\eta_r = 1 + 2.5\varphi + (6.2 + \frac{2.1}{\tau_B})\varphi^2 \qquad 2.19$$

Where φ is the volume fraction of solid in the suspension. The Baxter interaction parameter is a measure of attractive forces. Its value tend to infinity in the case of hard spheres and decreases towards zero in the case of adhesive hard spheres as the strength of attractive force increases (103). The equation has been verified experimentally up to 15 % volume percent of particles in the suspension. For even higher solid loading (φ = 0.495), the relative viscosity can be described as,

$$\eta_r = (1 - \frac{\varphi}{\varphi_m})^{-\eta\varphi_m} \qquad 2.20$$

Where φ_m is the maximum concentration at which flow is possible. Above this concentration the suspension behaves like solid.

3 Experimental

3.1 Synthesis of PANI and POMA

PANI and POMA are chemically synthesized by oxidation polymerization. A schematic of the synthesis process is shown in Figure 3.1. 1:1 mass ratio of aniline or orthomethoxyaniline monomers and ammonium persulphate, $(NH_4)_2SO_4$ are mixed with 2 mol L^{-1} hydrochloric acid at 0 °C for 4 hours. Emeraldine salts of the corresponding polymers are formed with Cl^- as counter ion. The residue is washed with water and acetone and then dried at 10 mbar pressure and 40 °C for 24 h. The dried residue is treated with 10 % NH_4OH for 4 hours with stirring in order to convert the emeraldine salt into emeraldine base and remove the chlorine counter ions (62, 104) . The solution is filtered, washed and the residue is dried at 10 mbar pressure 40° C for 36 h to obtain the final polymer sample.

Figure 3.1. Schematic of synthesis process of PANI and POMA.

3.2 Conductive polymer electrode preparation

The synthesized PANI and POMA are dissolved in NMP by stirring for 12-18 h then coated on a 15 μm thick Al foil by doctor blading technique. The Al foil is pre-treated with dielectrically hindered plasma (n.transfer GmbH, Germany) with argon as working gas (50 L min^{-1}). The samples are dried at room temperature for 12 h then at 60 °C in a vacuum oven for another 3 h.

PEDOT:PSS water suspension from Sigma Aldrich is also coated on a plasma treated Al foil with doctor blading technique. Then it is dried in vacuum oven to remove all water traces.

3.3 Composite electrode preparation

The composite electrodes with PANI/POMA are prepared with active material, conductive binder, normal binder and conductive additive. In case of PEDOT:PSS electrodes, no additional binder or conductive additives are used. A schematic of the process is shown in the Figure 3.2. The active material used in all cases is $LiFePO_4$. For the electrodes with PANI/POMA the used $LiFePO_4$ is brought from a different manufacturer than in case of electrodes with PEDOT:PSS (Table 3.3). It is referred as $LiFePO_4^*$ throughout the chapters.

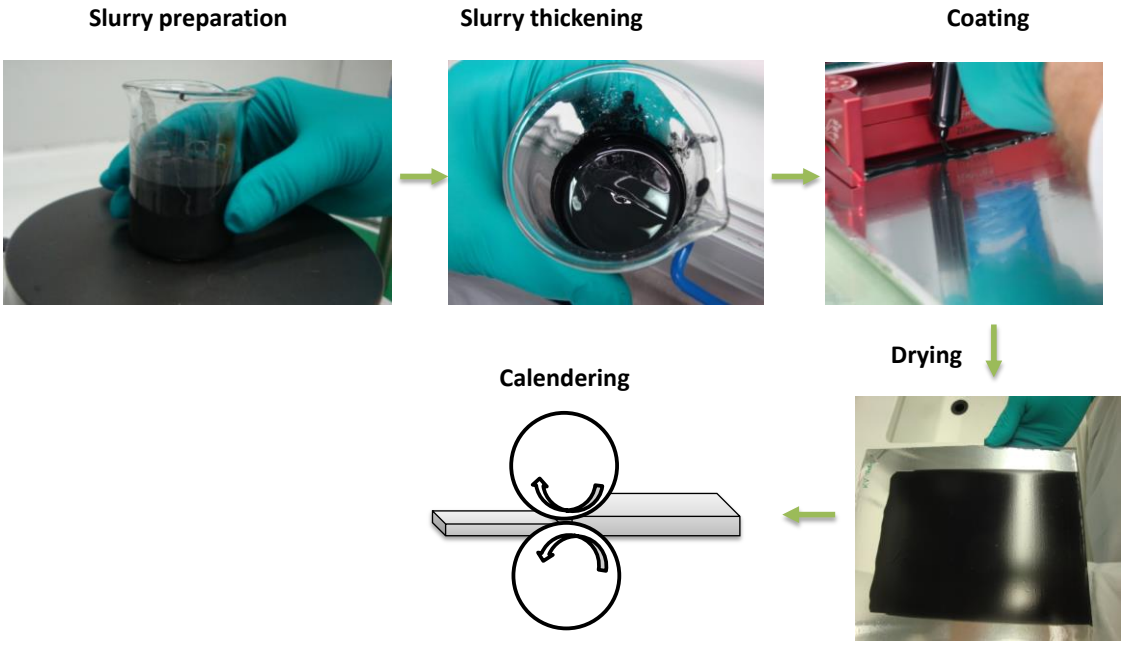

Figure 3.2. Different processes for preparation of composite electrode for lithium ion battery.

The first step is the mixing of the components. In case of both PANI and POMA based composite electrodes, PVDF and solvent is mixed for 2 hours at 50 °C with NMP solvent then CP is added. After that, carbon black is added and mixed for 30 min, and then $LiFePO_4^*$ is added and mixed for another 3 h. For the PEOT:PSS based composite electrode, an aqueous suspension of PEDOT:PSS and $LiFePO_4$ is prepared. An additional slurry thickening step is required to achieve the required flow behaviour of the slurry by drying it at 60-70 °C and removing the excess water. The prepared slurries are coated on a plasma pre-treated Al foil. The coating of the slurry is made using a doctor blade technique. The gap between the Al foil and the doctor blade is kept at 150 µm and the speed of the doctor blade is 1 mm s^{-1}. Then it is dried in red light for 3 h for

slow drying and then in vacuum oven for 12 h. After drying the positive electrodes are calendared using a hot rolling machine (MTI). The average thicknesses of all positive electrodes after drying and calendaring are in the range of 30 to 40 µm. For comparison conventional electrodes are prepared with $LiFePO_4^*$/$LiFePO_4$, C-black and PVDF. The slurry preparation and coating process is performed similar to other coatings.

For the PANI and POMA cells, the composition of the composite electrode is shown in Table 3.1. For the composite electrodes with PEDOT:PSS as binder, no additional binders are used. The composition of the electrodes is shown in the Table 3.2.

Table 3.1. composition of the composite electrodes prepared with PANI, POMA.

Sample Name	**%Active material $LiFePO_4^*$**	**%Binder (PVDF)**	**% CP**	**% carbon black**	**Solvent used**
PANI	84	2	4	10	NMP
POMA	84	2	4	10	NMP
PVDF	84	6	-	10	NMP

Table 3.2. composition of the composite electrodes prepared with PEDOT:PSS.

Sample Name	**%Active material $LiFePO_4$**	**%Binder (PVDF)**	**% PEDOT:PSS**	**% carbon black**	**Solvent used**
6 %	94	-	6	-	Water
8 %	92	-	8	-	Water
16 %	84	-	16	-	Water
PVDF	84	6	-	10	NMP
PEDOT:PSS	-	-	100	-	Water

3.4 Single cell preparation

From the prepared composite electrode, 1.1 mm diameter discs are cut using a cutter (E-Cell, Germany) to prepare positive electrodes for single cells. The prepared positive electrodes are used in standard swagelok single cells inside a glove box (MBRAUN,

Germany). Li metal is used as negative electrode and reference electrodes (Alfa Aesar GmbH & Co KG). A glass microfiber separator (Whatman company, Germany) and 1:1 ratio of ethylene carbonate (EC) and ethyl-methyl carbonate (EMC) with 1 M $LiPF_6$ (ABCR, Germany) is used as electrolyte for the cells. A schematic of the swagelok cell is shown in Figure 3.3.

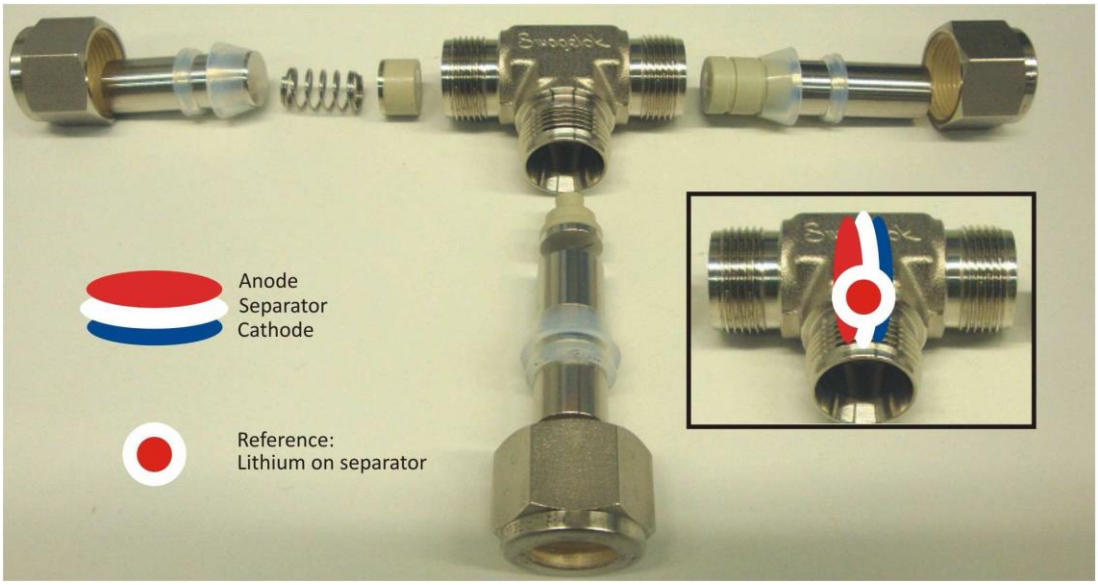

Figure 3.3. Schematic of a swagelok cell.

3.5 Rheology experiments

3.5.1 Rheological measurements using rheometer

A rheometer (Thermo Fischer-HAAKE) is used to perform rheological analysis of fluids, suspensions or emulsions. There are different kinds of arrangements of the shear force application such as cup and bulb, cone and plate and parallel plate type. For many particle suspensions parallel plate is used to study the rheological behaviour because of the advantage of lower sample volume requirements.

In this measurements the sample is kept in between two parallel plates with defined radius of 50 mm. The distance where the sample is placed should be in the range of 1 mm. The upper plate is controlled to put different kind of shear force on the sample. To apply shear deformation, the upper plate can be rotated in a particular angular velocity. The shear rate is changed by changing the speed of rotation. This is depicted in Figure 3.4a. Small amplitude tests can also be performed with good

precision using this technique. In this tests, a sinusoidal shear stress is applied and the fluid layers move accordingly as shown in the Figure 3.4b.

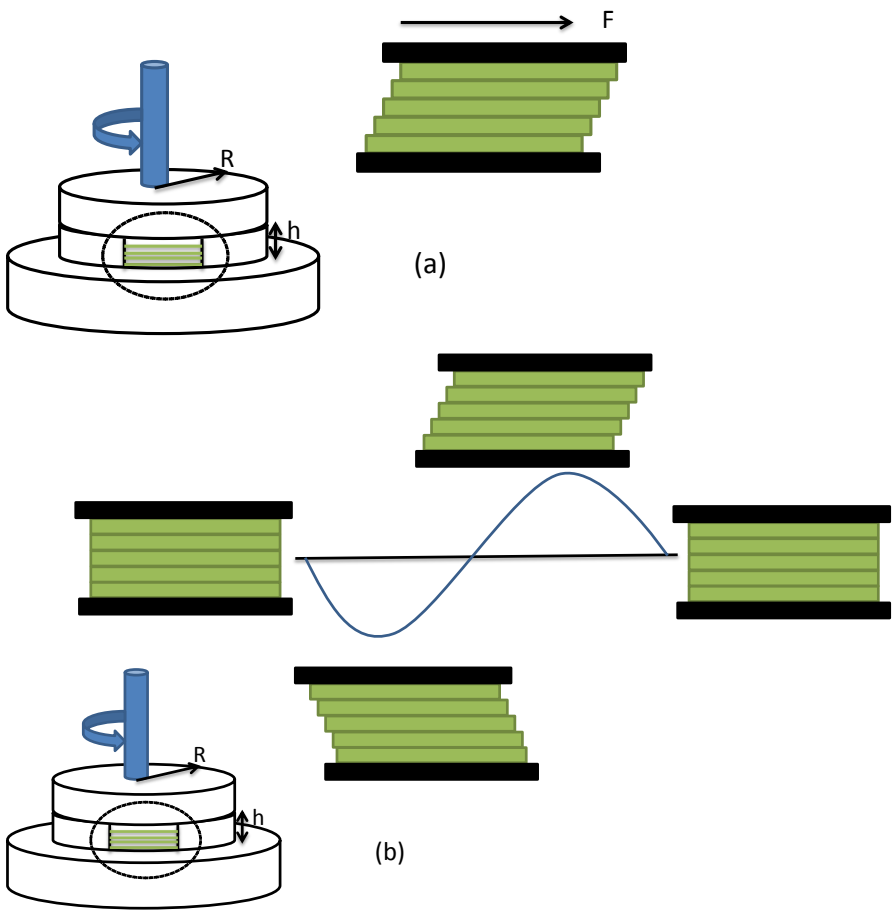

Figure 3.4. schematic of fluid movement in plate-plate rheology measurents (a) shear deformation (b) small amlitude shear test.

For the rheological measurements, two kind of test are performed in a plate-plate rheology measurement as described above. One is the deformation test to study the slurry behaviour with shear rate. The other is the small amplitude rheology test for understanding the viscoelastic response of the slurry. The rheological measurements are performed at 25 °C with a rheometer (MARS III, Thermo Fischer - HAAKE, Germany) using a plate-plate geometry with 35 mm diameter plates and a gap of 0.8-1 mm between the plates. In order to ensure that the entire sample had the same mechanical history, the samples are pre-sheared at 1000 s^{-1} for 45 s and then kept at rest for 1000 s (15). The slurry viscosity and shear stress is studied as a function of shear rate between 0 to 1000 s^{-1}. For understanding the viscoelastic behaviour of the slurries and to simulate the flow induced by the doctor blade coating process, a small amplitude shear rate measurement is performed. The shear rate applied during coating of the slurry using

doctor blade is the ratio of speed and gap between doctor blade and substrate. For a speed of 1 mm s^{-1} and gap of 150 µm, the shear rate is 6.7 s^{-1}. Three small amplitude stress measurement have been performed. To determine the linear elastic regime, stress sweep at a strain of 0.01 to 100 % is measured at frequency of 1 Hz followed by frequency sweep from 1 Hz to 10 Hz at 0.4 % strain which is in the linear elastic regime. Finally, in order to simulate the coating conditions, the slurry is sheared at 6.7 s^{-1} and then kept at rest for 1000 s to understand its flow behaviour.

3.6 Physical and mechanical characterization of the composite electrodes

The morphology of the composite positive electrodes is studied using scanning electron microscope (SEM NEON 40EsB, Zeiss, Germany) operating at 5-20 kV. High resolution x-ray computer nano-tomography (nano-CT, SkyScan 2011, Bruker, Belgium) is used to understand the bulk morphology of the composites. The images are taken as the average of six frames with two seconds exposure time per frame. The resulting images are reconstructed using the Sky Scan NRecon software package. The porosity of the electrodes is measured with mercury porosimetry (Pascal 140/400, Porotec, Germany). Standard 4-probe method is used to measure the in plane conductivity of the coatings prepared on a glass substrate by doctor blade technique. Through plane conductivity is evaluated by measuring the resistance across the thickness of the electrodes as a function of the applied pressure. The adhesion strength of the coating to the current collector is investigated by a 90° peel-up tape test (105). In this measurement, the electrodes with an area of 3.8 mm^2 are fixed between two parallel stamps by means of an adhesive tape (tesafix, Germany). The tensile force is applied by using a uniaxial testing machine to the upper plate to peel the electrode out of the current collector. The adhesion strength is calculated from the tensile force required to peel the coating off the Al foil and the area of the electrode where the stress is applied.

3.7 Electrochemical characterization of the single cells

The electrochemical behaviour of the prepared cells is tested using a conventional potentiostat/galvanostat (Verstastat, Ametek, USA). The positive electrodes made of only conducting polymers are also studied in this potential range to understand their

behaviour. The composite electrodes are studied between potential ranges of 2.8 till 4 V. The charging-discharging tests are performed using a battery test station (Basytech instruments, Germany) in a climatic chamber (Vötsch, Germany) at 25 °C.

3.8 Chemicals used

Table 3.3. list of chemicals used

Chemicals	**Company**	**City**	**Country**
PEDOT:PSS	Sigma Aldrich	Munich	Germany
$LiFePO_4^*$	Süd chemie	Munich	Germany
$LiFePO_4$	MTI	Richmond, CA	USA
carbon black	Timcal	Düsseldorf	Germany
PVDF	Alfa Aesar GmbH & Co KG	Karlsruhe	Germany
Natriumcarboxymethylcellulose (CMC)	MTI	Richmond, CA	USA
Li metal	Alfa Aesar GmbH & Co KG	Karlsruhe	Germany
separator	Whatman	Dassel	Germany
ethylene carbonate, ethyl-methyl carbonate, Lithium hexyflourophosphate	ABCR	Karlsruhe	Germany
Aniline, o-methoxyaniline	Sigma Aldrich	Munich	Germany
ammonium persulphate	Sigma Aldrich		Germany

4 Polyanilines

In the present chapter the characterization of the chemically synthesized PANI and POMA is described and their electrochemical behaviour in aprotic electrolyte is discussed. Their usability as a partial binder for positive electrode for lithium ion battery is described.

4.1 Structural and thermal characterization

Infrared spectroscopy (IR) is performed on the synthesized samples of PANI and POMA to verify their structure. The corresponding IR spectra are presented in Figure 4.1. The spectrum of PANI shows pronounced absorption features at 1588 cm^{-1} and 1493 cm^{-1}. These peaks correspond to the nitrogen-quinoid-nitrogen (N-Q-N) stretching of the quinoid unit and nitrogen-nitrogen (N-N) stretching of the benzoid unit respectively (74, 106). The features at 1289 cm^{-1} and 1142 cm^{-1} correspond to the carbon-nitrogen (C-N) stretching in amide and amine bonds (74, 107). These characteristics indicate that the polyaniline is present in its emeraldine state. Furthermore the absence of peaks in the ranges of 1300- 1340 cm^{-1} implies that there is no protonation of the imine sites (108) and thus the deprotonated state of emerladine, the emeraldine base state, is confirmed. In the case of POMA, the characteristic absorption peaks of the N-Q-N stretching of the quinoid unit (1593 cm^{-1}) and nitrogen-benzoid-nitrogen (N-B-N) stretching of the benzoid unit (1508 cm^{-1}) are shifted to higher wave number than for PANI. This shifting is due to the positive mesomeric effect of the methoxy functional group, causing an increase of the electron density in the benzene ring (109). The characteristic absorption peak indicating the presence of C-O stretching of the methoxy group appears at ca. 1142 cm^{-1} (109). Moreover, both POMA and PANI emeraldine base structure is confirmed due to absence of the peaks for protonated imine groups.

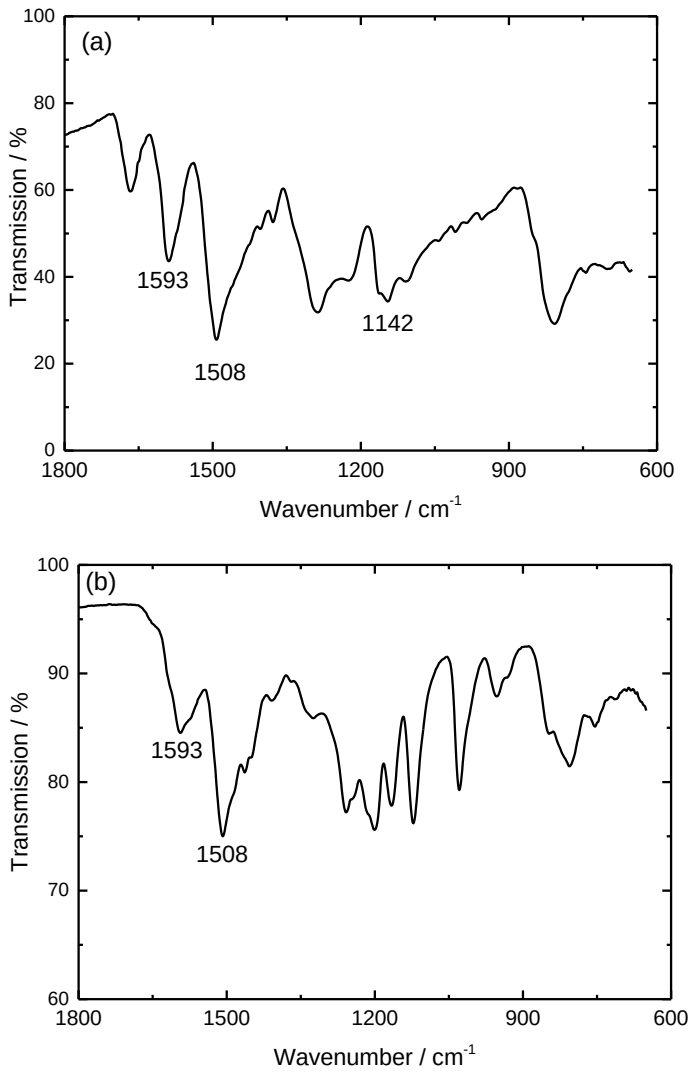

Figure 4.1. IR spectra of (a) PANI and (b) POMA

The thermal behaviour of the polymers is studied using thermo gravimetric analysis (TGA) and differential scanning calorimetry (DSC) to understand its stability at elevated temperatures. High temperature stability is necessary when it is used for a binder in battery composite electrode. Figure 4.2 shows the mass loss and phase transition temperatures for the polymers in the temperature range from 0 to 500 °C. For both polymers, an endothermic reaction occurs between 50 °C to 120 °C and a minor mass loss is observed in the TGA curve, which corresponds to water evaporation (110, 111). A pronounced exothermic reaction is visible for both POMA and PANI between 200 °C and 300 °C coupled also with a distinct mass loss. This behaviour indicates re-crystallization followed by a crosslinking isomerization reaction, which typically occurs for the PANI family of polymers in the temperature window of 175 °C - 350 °C (111-113). The weight loss observed between 350 and 500 °C (PANI), 300 and 500 °C

(POMA), respectively, are due to the polymer degradation. The differences observed for PANI and POMA are related to the crosslinking isomerization process that is taking place prior to the beginning of the degradation process. The crosslinking process is affected by the size of the alkoxy substituent and subsequently the degradation process upon the thermal treatment (111-113). However, from these results it is not possible to state that the crosslinking process occurs through a different mechanism for the different types of polymer, i.e. PANI, POMA. The presence of the methoxy group in POMA results in a steric effect, which blocks the crosslinking chemical reaction. In the PANI system, where the monomer aromatic ring does not contain any alkoxy group, the crosslinking isomerization reaction proceeds as expected, i.e. the degree of crosslinking in polyaniline system is much higher than in POMA (111). It can be seen from both TGA and DSC results that the degradation temperature for PANI is higher than that of POMA. Hence the increased crosslinking isomerization of PANI enhances its thermal stability which is in good agreement with the literature (111).

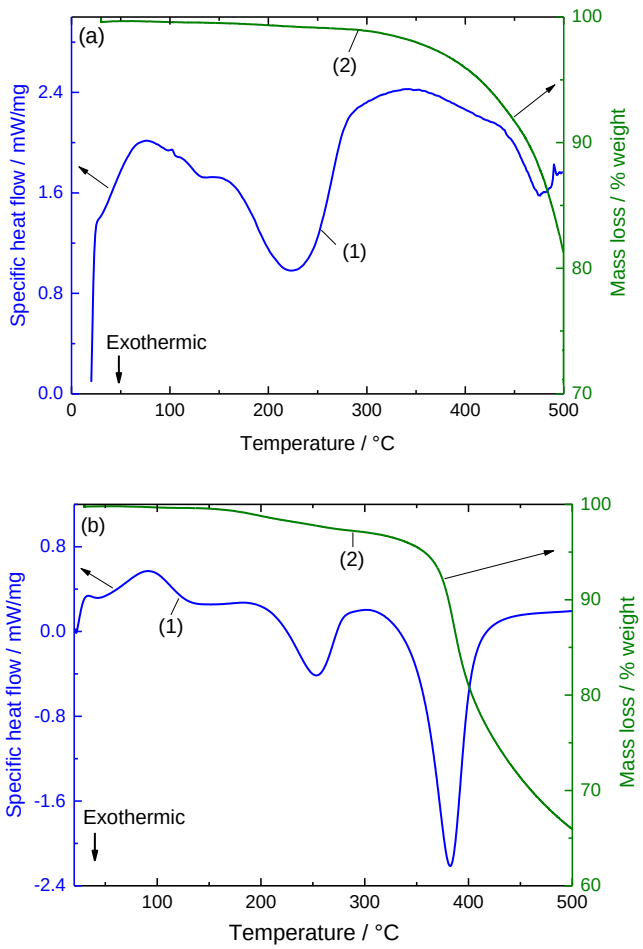

Figure 4.2. DSC (1) and TGA (2) curve for (a) PANI and (b) POMA.

4.2 Electrochemical behaviour of PANI and POMA

In order to understand the stability and redox behaviour of PANI and polymer films of PANI and POMA coated on aluminium substrates are studied in aprotic electrolyte by cyclic voltammetry with lithium metal as counter electrode and reference electrode. The used electrolyte consists of 1:1 ratio of EC:EMC and $LiPF_6$ salt (section 3.2, 3.7). The cyclic voltammograms (CVs) curve for PANI are shown in the Figure 4.3a at a scan rate of 5, 10 and 50 mVs^{-1}. At scan rate of 5 mVs^{-1} there is a clear oxidation peak at 3.5 V in good agreement with literature (74). At 3.85 V a shoulder in the CVs curve is observed. This can be the over oxidation of the polymer or it can be due to inhomogeneous distribution of different chain length of PANI in the film. Another explanation can be the presence of crystalline and amorphous domains of PANI within the polymer chain. The interaction of ions is different at these two different domains of polymers which lead to voltammetric signals at different potentials.

During the sweep from 4 to 2 V a broad cathodic peak is observed which spans from 3.6 till 3 volts. This is due to overlapping of two peaks from the reverse reduction reaction of the two oxidation reactions described above. The separation between the cathodic and anodic peak gives insight to the reversibility of the reaction. The separation between first pair of peaks is 0.17 V showing a quasi-reversible behaviour of PANI. The separation between the over oxidation peak is higher than for the main peak. At the scan rate 50 mVs^{-1}, the over oxidation peak is vanishing. Thus it may be concluded that this reaction is highly dependent on the scan rate. This effect could be attributed to the second reaction which is more pronounced at lower scan rates and is considered to be largely irreversible. Thus this reaction may be considered a degradative one. The oxidation and reduction process of PANI is studied by Raman spectroscopy and it is shown that the polymer is changing from emeraldine form to pernigraniline form during oxidation and from pernigraniline to emeraldine from during reduction (114).

The redox behaviour of POMA coated on Al foil in the aprotic electrolyte atmosphere at different scan rates is shown in the Figure 4.3b. The CV curve at 10 mV s^{-1} scan rate shows an oxidation peak at 3.5 V and a reduction peak during the back scan at 3.25 V. However, the observed redox peaks are shifting to higher potentials with increasing scan rate, which indicate the quasi-reversible nature of the redox reaction. The increase in peak separation in POMA as compared to PANI can be due to presence

of bulky methoxy group in the polymer chain, which reduces the electrical conductivity of POMA. Nevertheless, the CV measurements show both PANI and POMA are redox active in the aprotic electrolyte.

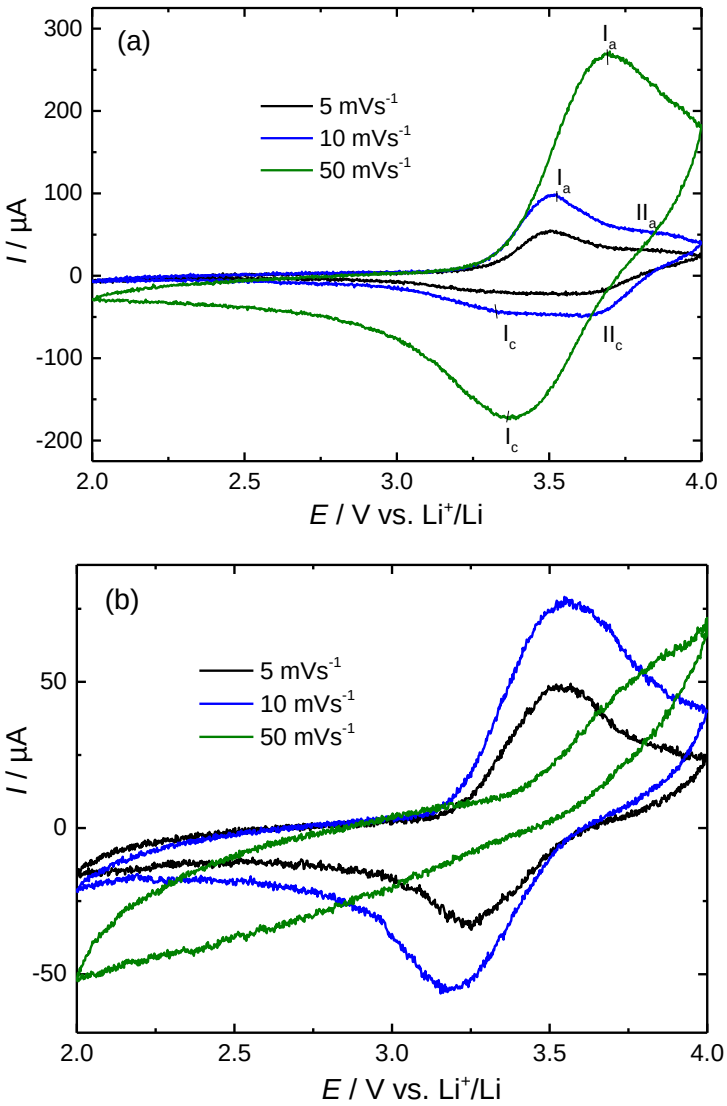

Figure 4.3. Cyclic voltammograms of (a) PANI and (b) POMA vs. Li^+ / Li counter electrode in aprotic electrolyte containing Li^+ ions.

4.3 Composite electrodes with $LiFePO_4^*$

After understanding the electrochemical behaviour of PANI and POMA in aprotic electrolyte, composite electrodes are prepared by partially substituting the conventional PVDF binder with POMA or PANI. As already mentioned in the experimental part, the composite positive electrodes consisted of $LiFePO_4^*$ active material, carbon black, PVDF binder and PANI/POMA. For comparison a composite electrode is prepared only

with PVDF binder and carbon black. The total amount $LiFePO_4^*$ and carbon black are kept constant in all cases i.e. 84 % and 10 % respectively.

The electrochemical behaviour of the prepared electrodes is shown in the CVs in Figure 4.4. The measured current is normalized by the corresponding mass of the electrodes for better comparison between the different composite electrodes. All electrodes show a redox activity i.e. oxidation and reduction peaks, in the potential range of 3 to 4 V which is typical for $LiFePO_4$ (65-71). In case of PANI, the oxidation and reduction peak separation is smaller and the peak starts at earlier potential as compared to other composite electrodes. Hence better reversibility of the redox reactions is observed in the composite electrodes containing PANI than the electrodes with POMA binder. This can be due to higher electrical conductivity of PANI compared to POMA. Due to presence of bulky methoxy groups the electrical conductivity of POMA decreases (115). However, as mentioned in the theory section, the solubility of POMA in NMP solvent is better than that of PANI due to the presence of the bulky methoxy group. So, the processing of slurry and preparing the electrodes is easier. Due to the small polymer content and the overlapping with the redox reaction of the active material, the polymer redox reaction cannot be clearly distinguished in both composite electrodes. The electrodes with only PVDF as binder without any conducting polymers show lower reversibility than PANI containing electrodes. However their reversibility is better than the POMA electrodes.

The charge density of the composite electrodes can be calculated from the CVs. It is the area under the current versus time curve as shown in Figure 4.5. The POMA composite electrodes show the highest gravimetric charge density (491 C g^{-1} / 136.4 mAh g^{-1}) followed by PANI (460 C g^{-1} / 127.8 mAh g^{-1}) and then PVDF binder based electrode (372 C g^{-1} / 103.33 mAh g^{-1}) electrode. This increased charge density of POMA and PANI containing composite electrodes can be explained by the redox behaviour of these polymers in the operating potential window. POMA and PANI can provide extra charge density due to their redox behaviour in the potential range increasing the overall charge density. However in case of PVDF binder electrodes the charge density is related to the redox reaction of Fe^{+3}/Fe^{+2} in $LiFePO_4^*$ only. From the CVs it can be expected that the composite electrode contacting PANI and POMA will have higher discharge capacity due to the added redox behaviour of these conducting polymers. It can also be expected that the PANI electrodes will show better voltage efficiency due to good electron transfer kinetics and higher electrical conductivity.

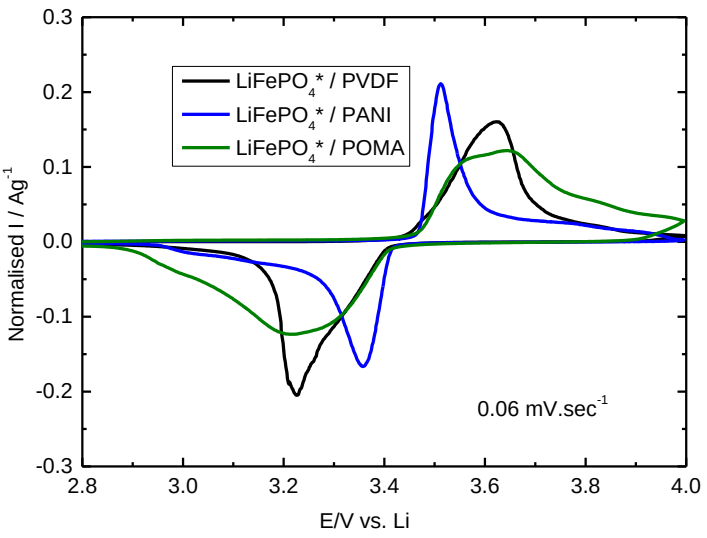

Figure 4.4. Cyclic voltammetry of composite electrodes vs. Li+/Li counter electrode in aprotic electrolyte containing Li^+ ions.

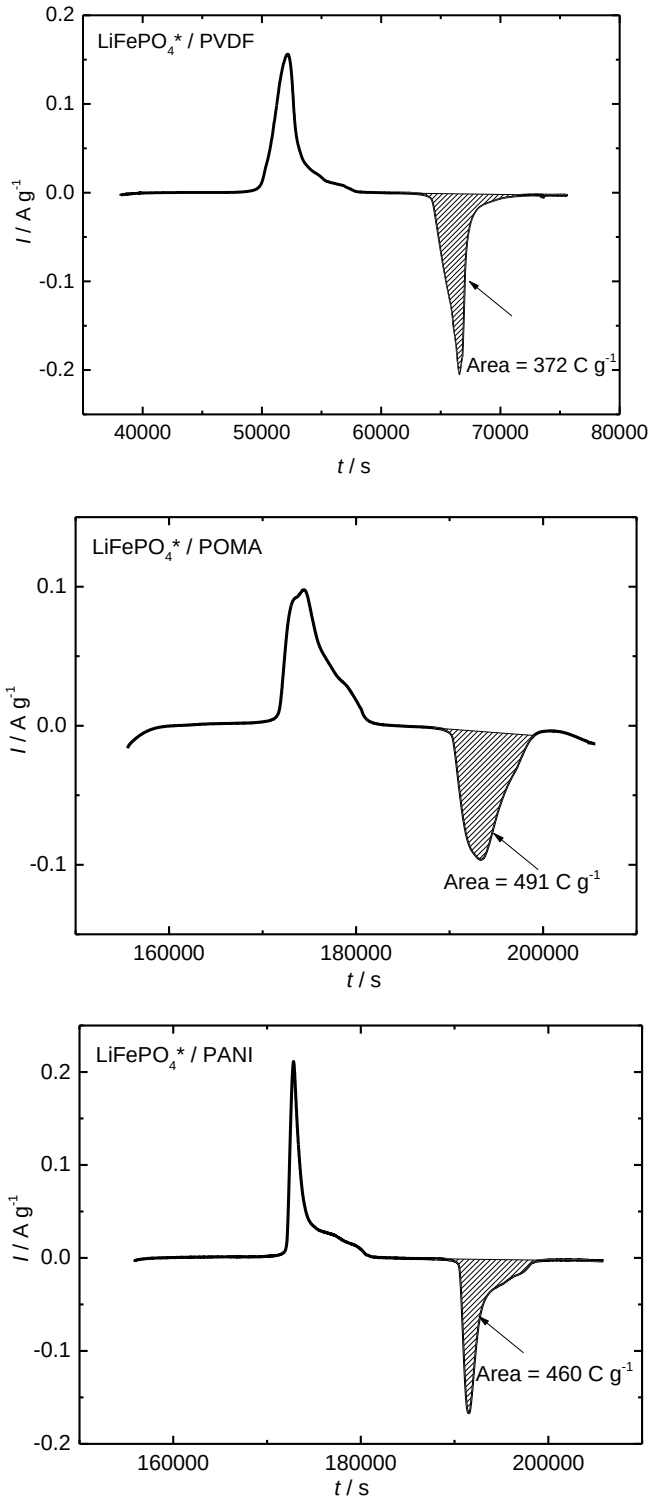

Figure 4.5. Current Vs. time plot for the CV for composite electrodes. The area under the curve shows the charge densities.

Galvanostatic charging and discharging at a rate of 0.2 C are performed to study the performance of the composite positive electrodes. The obtained voltage profiles are shown as a function of the gravimetric capacity (mAh g^{-1}) in Figure 4.6. The capacity is

called gravimetric capacity because it is obtained by normalizing the electrode capacity with the mass of the active material ($LiFePO_4$). The positive electrodes containing conducting polymer binders (POMA, PANI) showed a superior performance than the conventional positive electrodes with only PVDF which is in a good agreement with the capacity data obtained from the CVs. The PANI and POMA composite positive electrodes show 15 % higher specific discharged capacity (145 mAh g^{-1}) than the conventional PVDF positive electrode (126 mAh g^{-1}). A similar effect has also been demonstrated for $LiFePO_4$ / PANI composite positive electrodes in literature (41). In general, the polymeric binders also influence the stabilization of the active material (AM) and CB powders in the electrode slurry during the electrode preparation and thus the architecture of the electrode, which has significant influence on the electrode performance (9). Because of the flexible structure of the conducting polymers the overall three dimensional conductivity of the composite electrode is improved. Hence, it is presumed that utilization of active material is significantly improved in the composite positive electrode containing PANI/POMA. This eventually improves the capacity of the whole system.

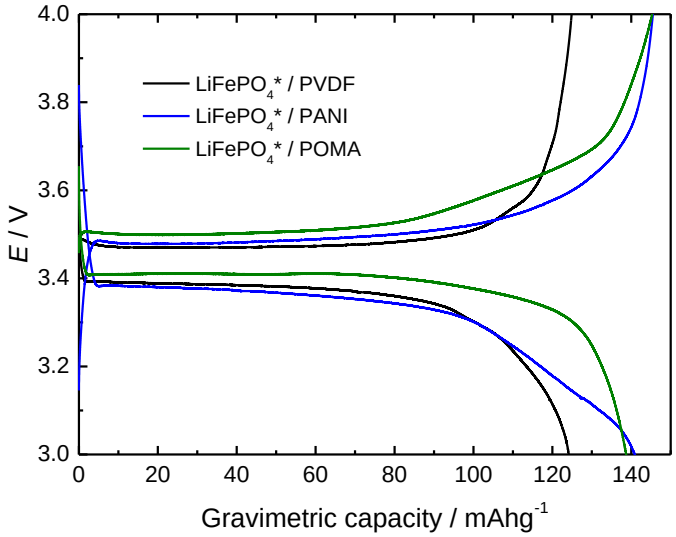

Figure 4.6. Potential vs. gravimetric-capacity for composite electrodes at a charging and discharging rate of 0.2 C.

Another important requirement of the composite electrodes is the rate capability. Therefore, the composite electrodes are charged at rates between 0.5 C and 5 C and discharged at 0.5 C to study the charging rate capability. Furthermore, electrodes are discharged at rates between 0.5 C and 5 C and charged at 0.5 C to study the discharging rate capability of the composite electrodes.

Figure 4.7a shows the charging rate capability of the composite electrodes. All the electrodes show a drop in capacity with increasing C rate due to polarization of electrodes. However, the capacity retention of electrodes with conducting polymers is higher compared to electrodes containing only PVDF binder showing that the composite electrode has higher conductivity. The oxidation of the polymer is faster than the iron oxidation in $LiFePO_4$. PANI and POMA are oxidized to pernigraniline from emeraldine form as explained in section 4.2. It has been shown that pernigraniline form of PANI forms a stable highly conducting salt with Li^+ ions from the electrolyte solution (116). Therefore, the conductivity of the composite electrode containing CP increases and the polarization is reduced with the transition of PANI/POMA from emeraldine to pernigraniline salt state.

Figure 4.7b shows the discharging rate capability of the composite electrodes. All electrodes show a drop in the discharge electrode capacity at higher charging rates as expected due to polarization of the electrodes. The rate capability of the POMA and PANI electrodes is similar to the PVDF electrode and after charging at 5 C less than 50% of the total capacity is retained during discharging. The change in the CP conductivity during the redox reaction is the reason for the observed behaviour. It is due to reduction of the pernigraniline salt to emeraldine base state of PANI/POMA. The base structure conductivity of PANI/POMA is lower compared to the salt form. Hence during reduction of the composite electrode conductivity of the polymer is reduced and only C-black helps in electrical conduction. Hence the rate capability at higher C-rate is very much like the conventional PVDF system where the electronic conductivity is only coming from the carbon additives.

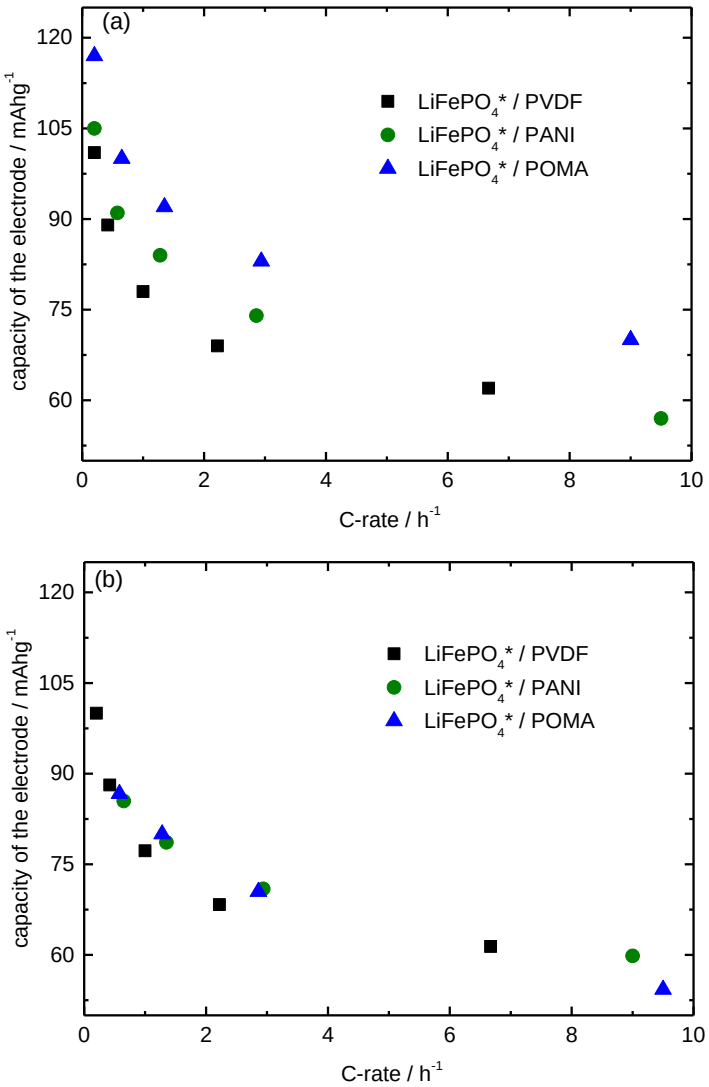

Figure 4.7. Gravimetric-capacity for composite electrodes at (a) different charging rates and same discharging rate of 0.5 C (b) 0.5 C charging rate and different discharging rates.

The cycling stability of prepared composite positive electrodes is studied by continuous battery cycling at 1 C in the potential window 2.8-4 V (Figure 4.8) for 100 cycles. Every 20th cycle, a capacity test at 0.2 C is performed. Electrodes, where PANI is used as a partial binder, run for 60 cycles and stopped running after that. This can be due to the degradation of electrode with cycling because of its bad adhesion to the current collector. POMA and PVDF samples run for 100 cycles and their behaviour is also shown in the Figure 4.8. POMA and PVDF cells show decrease in electrode capacity with cycling.

However, the PVDF and PANI cells show higher and stable voltage efficiency than POMA cells for 100 cycles. The voltage efficiency of POMA is lowest. This can be due to higher polarization effect of electrodes consisting of POMA than PANI and PVDF/C-black cells. It could also be due to lower stability of POMA with cycling as compared to PANI. To verify the cyclic voltammetry of the electrodes with only PANI and POMA is performed at a scan rate of 50 mVs^{-1} for 200 cycles (Figure 4.9). In case of POMA the current is decreasing with the cycle number (cycle number 1 to 200). In case of PANI the change is not very significant. Hence, it can be seen clearly that the POMA electrodes are degrading with cycling. The possible reason could be the expansion and contraction of the polymer during the redox reactions which is also found for PANI and related polymers in water based electrolytes (117, 118). However, clear redox peaks of both POMA and PANI are absent which could be due to higher scan rate or thicker coatings of electrodes used for the measurements.

Figure 4.8c shows the coulombic efficiency of the samples with cycling. The coulombic efficiency of a battery is the ratio of the charge that can be extracted from the battery during discharging relative to the charge entering the battery during charging. The losses that reduce coulombic efficiency are primarily associated with irreversible side reactions such as degradation of the electrode components and the electrolyte. For the PANI samples the coulombic efficiency is fluctuating for 60 cycles. This can also explain the low cycling stability of PANI because of material losses during cycling. The columbic efficiency of POMA is higher and more stable than PVDF samples for 100 cycles (Figure 4.8c) showing its superior performance over the studied cycle range.

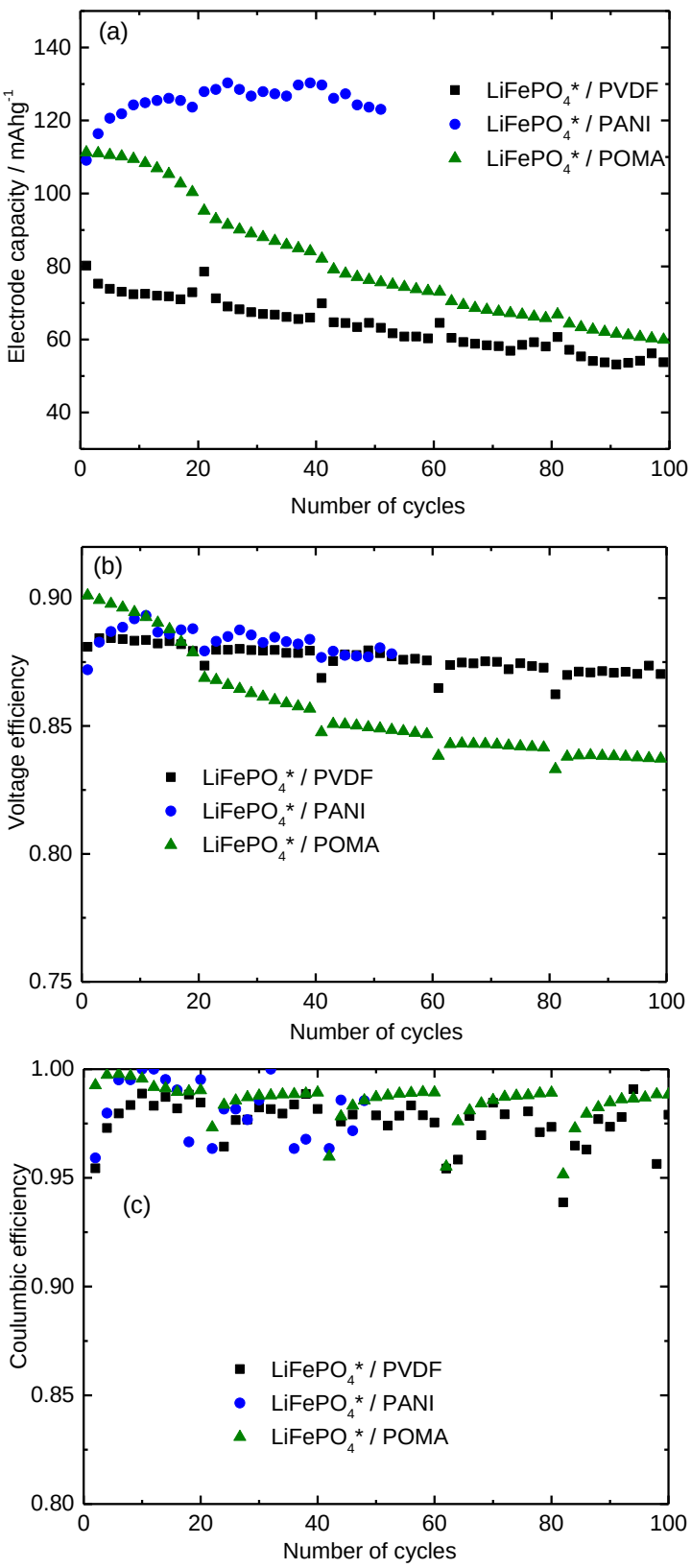

Figure 4.8. (a) Electrode capacity at 1 C (b) Voltage efficiency and (c) coulombic efficiency of PANI, POMA and PVDF samples from cycling test.

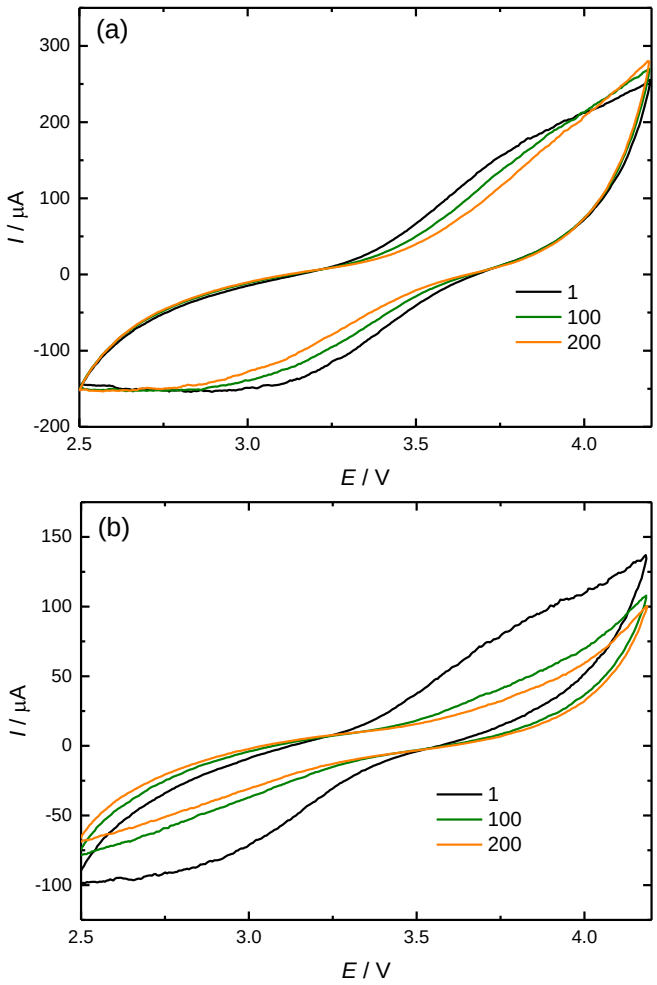

Figure 4.9. CV of (a) PANI, (b) POMA for 200 cycles at 50 mVs^{-1} vs. Li^+ / Li counter electrode in aprotic electrolyte containing Li^+ ions.

4.4 Conclusion

Infrared spectroscopy, TGA and DSC are used to characterize the chemically synthesized PANI and POMA. The emerldine base state of the polymers is confirmed with these measurements. Both polymers show high temperature stability up to 200 °C suggesting their usefulness in battery environment. PANI and POMA also help to improve the capacity of the system because of their redox active behaviour in the potential range of 3 to 4 V. Moreover, an improvement in the discharge rate capability is visible. However, the charge rate capability is not changing in comparison to the conventional PVDF binder electrode indicating the change in the conductivity of the conducting polymer due to the oxidation to the low conducting pernigraniline state. The composite electrodes with PANI showed stable behaviour till 60 cycles and POMA

showed ageing behaviour with cycling. The presence of PANI and POMA in composite electrodes improves their three dimensional conductivity. However, the oxidised state of PANI and POMA is not electrically conductive as compared to the reduced state. Hence additional C-black is always needed in this type of composite positive electrode so that the composite electrode can conduct electrons at potentials where PANI and POMA have very low electronic conductivity. Complete replacement of PVDF binder and C-additive is not possible with using PANI or POMA as conductive binder. However, the composite electrodes show low cyclic stability, which is partially due to bad adhesion to the current collector. Therefore, the complete exchange of the PVDF binder by PANI or POMA is also not feasible. Hence, PANI and POMA can be used only as a partial binder material in positive electrodes using $LiFePO_4$ as active material, which give rise to slight improvement of the electrode performance.

5 Poly-3,4-ethylendioxythiophene (PEDOT:PSS)

The PEDOT:PSS water suspension, bought from Sigma-Aldrich company, has an average molecular weight of 280,000 and the ratio between PEDOT and PSS units is 1:2.5. Its thermal behaviour, morphology and electrochemical behaviour are studied using different characterization methods.

5.1 Thermal characterization

The polymer suspension is dried in the vacuum oven at 60 °C for 12 hours to get dry powder of PEDOT:PSS polymer. The thermal behaviour of the powder is studied using DSC and TGA. The results obtained from the thermal characterization are shown in Figure 5.1. In the DSC curve, the endothermic process around 100 °C is related to the mass loss due to evaporation of water, in good agreement with the literature (110, 111). The water content estimated from the TGA results amounts to approximately 10 mass % is relatively high, considering the drying of samples in vacuum oven before TGA measurements. Water is known to be detrimental inside the battery environment. It reacts with the common electrolyte especially with the $LiPF_6$ to degrade the salt and decrease the concentration of electrolyte (119, 120). It also reacts with active electrode material or SEI in the negative electrode side and reduces the lifetime of the cell (121, 122). Hence it is necessary to take out all water from the coatings through extensive drying process to achieve better performance of the electrode. At about 300 °C the counter ion PSS starts to decompose followed by the melting and degradation of PEDOT at about 400 °C. Both PSS and PEDOT decomposition result in significant mass losses as observed in the TGA curve. This results show, that the polymer have very high thermal stability which is also shown by other studies (68).

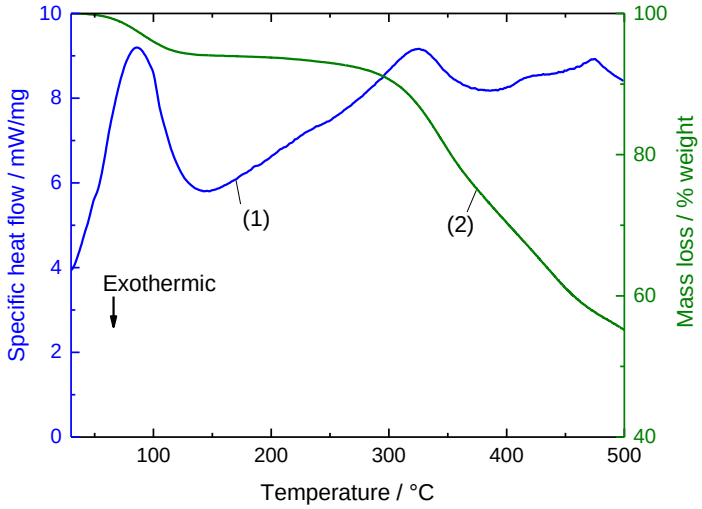

Figure 5.1. DSC (1) and TGA (2) curves of PEDOT:PSS.

5.2 Morphology of PEDOT:PSS

The morphology of the dried PEDOT:PSS powders is studied using scanning electron microscopy (SEM). In Figure 5.2 the SEM images of PEDOT:PSS are shown at different magnifications. Both images depict the porous morphology of the polymer. This morphology can be helpful when PEDOT:PSS is used as a binder in composite electrodes for lithium ion battery because it will enhance the ion mobility through the electrode.

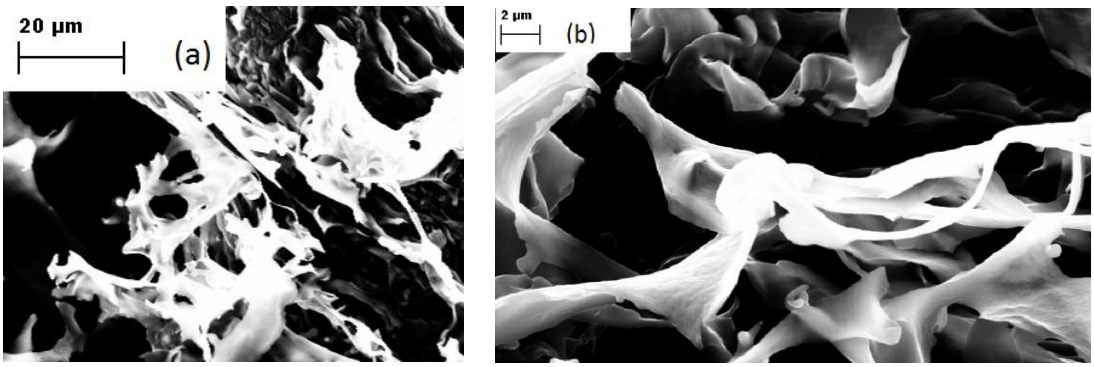

Figure 5.2. Scanning electron microscope images of PEDOT:PSS**.**

5.3 Electrochemical behaviour of PEDOT:PSS

Although there are lot of studies performed with PEDOT:PSS in aqueous electrolyte, there is a little information about the behaviour of PEDOT:PSS in organic aprotic electrolyte. Hence, thin film coatings of the polymer with a thickness of 1-4 µm are prepared on an Al foil by doctor blading and their electrochemical behaviour is studied. Then the coatings are dried extensively for 12 h at 60 °C in the vacuum oven. According to the thermal analysis no change in polymer structure is observed at this temperature. Subsequently, three electrode swagelok cells are prepared with a lithium as counter electrode and Li^+ containing aprotic electrolyte (1:1 EC:EMC + 1 M $LiPF_6$). The electrochemical behavior of these swagelok cells is studied by cyclic voltammetry at different scan rates and at different temperatures. The scan rate is varied from 5 mV s^{-1} to 500 mV s^{-1} in the potential range of 2.5 V to 4.2 V. This potential window is where the common positive electrode materials such as $LiFePO_4$, $LiCoO_2$ are redox active. The polymer layers show a pseudo-capacitive behaviour in the potential range 2.5 to 4.2 V and the redox reaction can hardly be distinguished even at low sweep rates (Figure 5.3). Here it should be mentioned, that the appearance of the pseudo capacitance in this potential range is more pronounced for thicker layers of 4 µm. For thin layers (2 µm), which are shown in Figure 5.4, it is negligible. The observed reduction wave at potentials more negative than 3 V and the corresponding oxidation shoulder can be attributed to the partial redox reaction of single PEDOT chains and/or domains within the polymer matrix, since the bulk reduction of the PEDOT:PSS in such electrolytes starts at potentials more negative than 2.5 V (76). However, the polymer shows little redox activity in the potential range of 3 to 4 V where $LiFePO_4$ is redox active. Therefore, it is not expected that a change in the conductivity of the electrodes due to reduction of the polymer will take place upon charging and discharging of the polymers in the potential range 3 to 4 V.

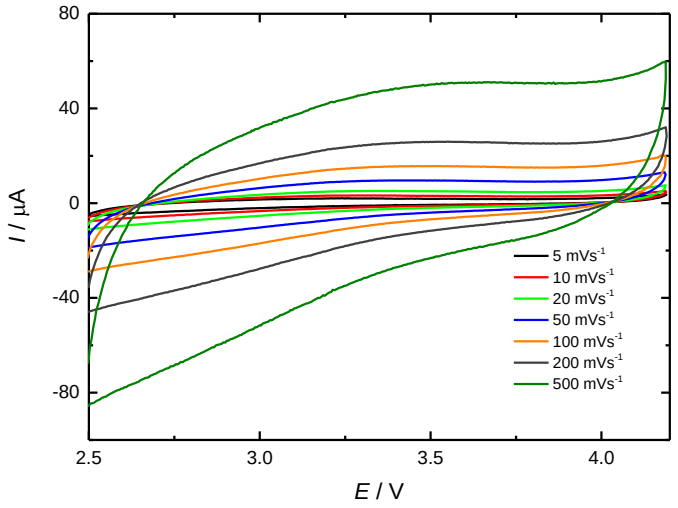

Figure 5.3. CV at different scan rates of PEDOT:PSS film with approximatly 4 µm thickness versus lithium counter electrode in the presence of aprotic Li^+ containing electrolyte (1:1 EC:EMC + 1 M $LiPF_6$).

Since conventional lithium ion batteries operate at different temperatures, it is interesting to study the electrochemical behaviour of the PEDOT:PSS thin films in the range from 10 °C to 40 °C (Figure 5.4). For this measurements thinner coating of approximately 2 µm are used in order to reduce the influence of the bulk thickness and porosity. It can be seen from the Figure 5.4 that there is no pseudo capacitive behaviour present in the CVs at different temperatures. The capacitive current is rising with increasing temperature, indicating the increase in the double layer capacitance of the system with temperature.

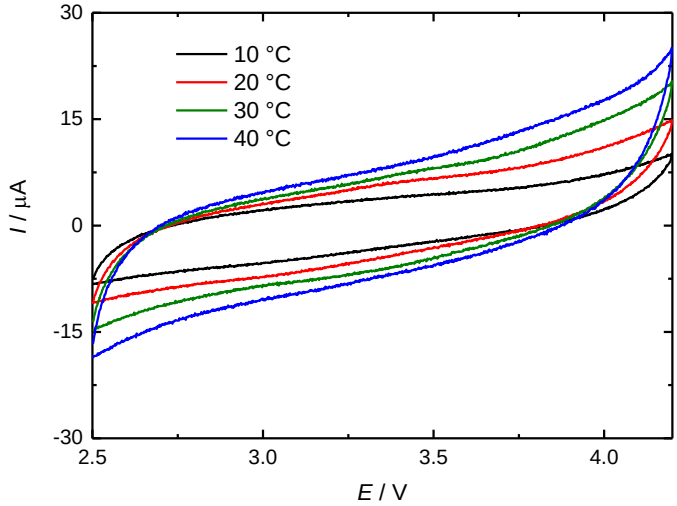

Figure 5.4. CV at different temperatures of PEDOT:PSS film of 2 µm thickness; 10 mV s^{-1} scan rate verses lithium counter electrode in the presence of aprtotic Li^+ ion containing electrolyte (1:1 EC:EMC + 1M $LiPF_6$). Reproduced from own publication (I).

Electrochemical impedance spectroscopy (EIS) at 2.5 V and 3.5 V DC level are performed to quantify the effect of the temperature on the electrical conductivity of PEDOT:PSS. The corresponding Nyquist plots at different temperatures in the frequency range 500 mHz to 100 kHz are shown in the Figure 5.5. For all the temperatures three distinct regions are visible in the graphs. At high frequencies, a linear increase in the impedance arises with a slope near 45° (Warburg type) which is characteristic for the transmission-line behaviour of porous systems. This behaviour is caused by pore exhaustion and distortion effect due to progressive iR-drop down the pores (123). At lower frequencies at about 100 Hz a knee region can be observed, going into a third region of the complex plane, where the capacitive behaviour is more dominant. At frequencies higher than the knee frequency the ions in the electrolyte follow semi-infinite diffusion and at frequencies lower than the knee frequency finite diffusion takes place (124). It can be observed at 2.5 and 3.5 V that the knee frequency decreases with increasing temperature. This is due to increase in diffusion coefficient with increasing temperature. It can also be observed that, the difference between the low frequency regions is more significant at 3.5 V than at 2.5 V.

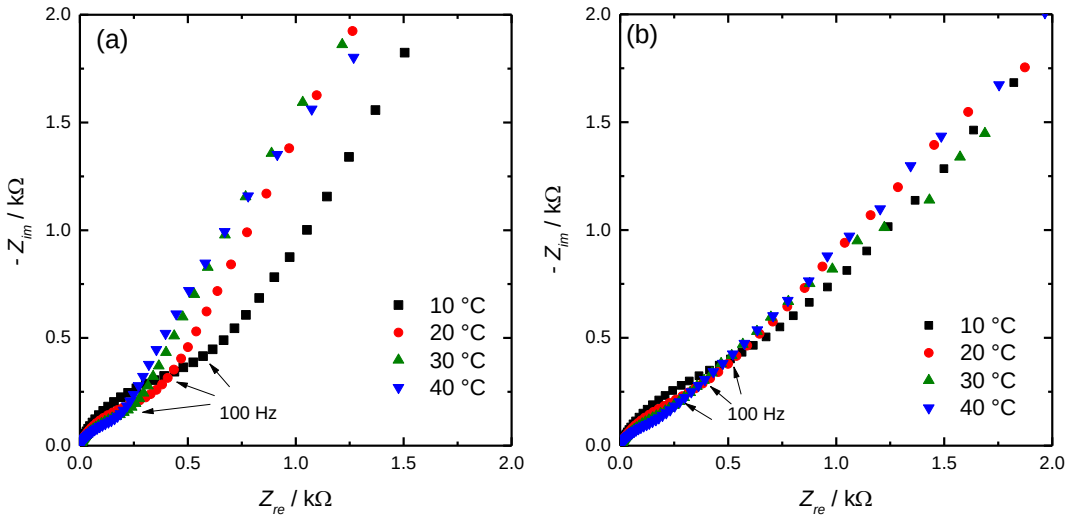

Figure 5.5. EIS at 500 mHz to 100 kHz at different temperatures; electrolyte is 1:1 EC:EMC + 1 M $LiPF_6$, 10 mV DC voltage a) 3.5 V b) 2.5 V; AC amplitude.

The physical interpretation of the observed impedance curve is very complicated, A modified transmission line model can be used to evaluate the electronic and ionic conductivities within the porous conducting polymer film (125, 126). The electric circuit used for the quantitative evaluation of the impedance data is shown in Figure 5.7. Each element contains a series of an electronic (R_I), an ionic (R_E) resistor and a double layer capacitor (C_F). Several of these three different impedance components are connected parallel to each other. The solution resistance (R_S) is in series with this circuit. The values have been calculated for different EIS plots at 2.5 V and 3.5 V DC using the following equations (126, 127).

$$\frac{1}{R_\infty} = \frac{1}{R_E} + \frac{1}{R_I} \qquad [5.1]$$

$$R_\Sigma = R_E + R_I \qquad [5.2]$$

$$|Z - R_\infty - R_S|^2 = \frac{R_\infty(1-2\rho)^2}{\omega C_F} \qquad [5.3]$$

Where R_∞ is the high frequency intercept of the Warburg type region in the complex impedance plot minus R_S and R_Σ is the theoretically constant real impedance at lower frequency minus R_S (Figure 5.6). ω is the angular frequency applied and $\rho = (R_E+R_I)/R_\Sigma^2$. Rs is calculated using the intercept of impedance plot of current collector (Al) vs. lithium electrode in the battery electrolyte.

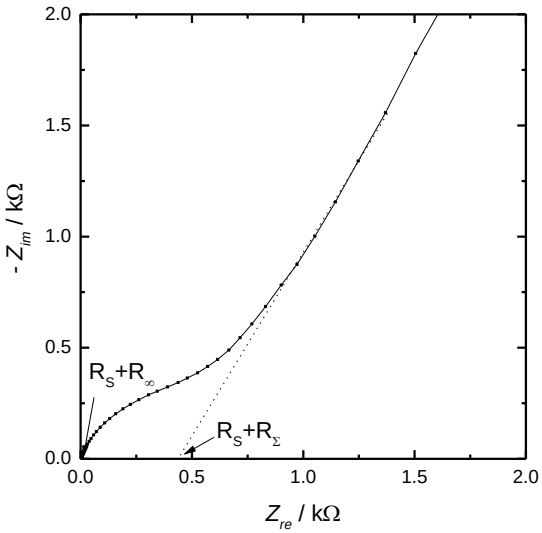

Figure 5.6. Complex plane impedance plot of PEDOT:PSS.

The obtained values indicate that the resistance values decrease with increasing temperature. This effect is more pronounced for the electronic and ionic resistance of the polymeric film in comparison to the electrolyte resistance. An increase in the capacitance of the system with rising temperature is also observed which is in good agreement with the CVs in Figure 5.4.

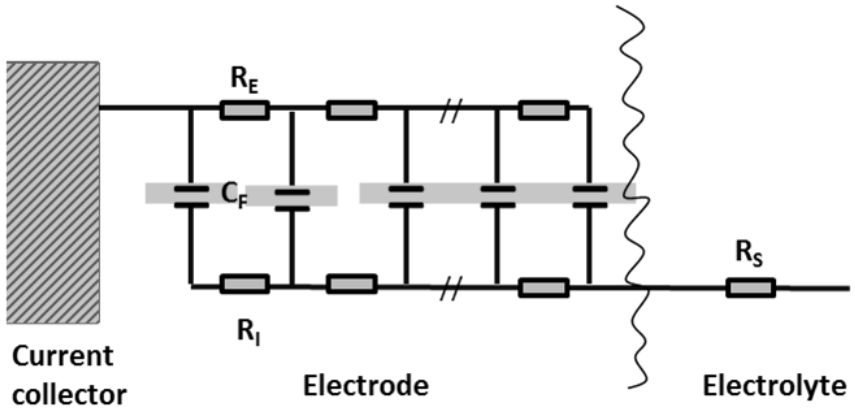

Figure 5.7. Equivalent circuit used to model the impedance behavior of PEDOT:PSS films. Reproduced from own publication (I).

Table 5.1. Impedance data evaluated using equivalent model 3.5 V.

T (°C)	R_S (Ω)	$R_{Electronic}$ (Ω)	R_{Ionic} (kΩ)	C_F (μF)
10	2.70	0.724	11.60	36.80
20	1.91	0.558	9.61	40.80
30	1.47	0.179	8.20	53.20
40	1.16	0.078	1.66	80.70

Table 5.2. Impedance data evaluated using equivalent model 2.5 V.

T (°C)	R_s (Ω)	$R_{Electronic}$ (Ω)	R_{Ionic} (kΩ)	C_F (μF)
10	2.5	0.53	10.9	62
20	1.88	0.53	9.89	90
30	1.52	0.23	6.25	143
40	1.15	0.07	4.22	211

The specific electrical conductivity of the PEDOT:PSS film calculated from the EIS data at 2.5 V and 3.5 V are plotted as a function of the temperature in Figure 5.8. The electrical conductivity of PEDOT:PSS obtained at 20 °C is 0.99 S cm^{-1} and 0.94 S cm^{-1} at 2.5 V and 3.5 V, respectively. These values are in very good agreement with the 4 probe conductivity data of PEDOT:PSS coatings on glass which is 1 S cm^{-1} at room temperature. Therefore, it can be considered that the behaviour of the PEDOT:PSS film under the studied conditions can be described very well by the modified transmission line model (Figure 5.7). In Figure 5.8, it can be clearly seen that the electronic conductivity of the polymer increases with the increasing temperature at both studied potentials. This is typical for semiconductors with a positive temperature coefficient such as PEDOT in its oxidized conductive form (128). Therefore, improved rate capability and voltage efficiency at elevated temperatures of 40 °C can be expected when PEDOT:PSS is used as a binder in composite positive electrodes for lithium ion batteries.

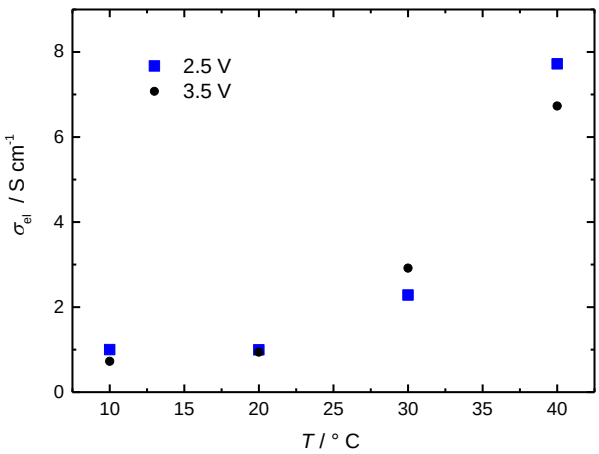

Figure 5.8. Electrical conductivity of the PEDOT:PSS film as a function of temperture at 2.5 V and 3.5 V DC potential vs. Li/Li^+.

The electrochemical stability of the polymer layers at room temperature is also studied by CV in the potential range from 2.5 to 4.2 V with 50 mV s^{-1} scan rate. Selected CVs are shown in Figure 5.9a for polymer film with 4 µm thickness. No significant ageing of the PEDOT:PSS layer under the cycling conditions is apparent for the preformed 200 cycles in this potential window. However the pseudo capacitance observed in the initial cycles for the thick layers diminishes with cycling, which can be beneficial for the battery performance, since the reduction of PEDOT leads to a decrease of electrical conductivity. An increase in the calculated electronic conductivity can be observed with increasing cycle number (before cycling 0.34 S cm^{-1}, after cycling 0.66 S cm^{-1}). This effect could be caused by rearrangement in the polymer structure during cycling, which may facilitates the interchange hopping of the charge carriers. EIS is performed at OCV before and after the cycling of PEDOT:PSS films for 200 cycles. There is no significant change in the impedance behaviour in Figure 5.9b. Hence, only minor changes in the properties of the polymer can be expected. This confirms the stability of the polymer in aprotic electrolyte environment for 200 cycles in the used potential window.

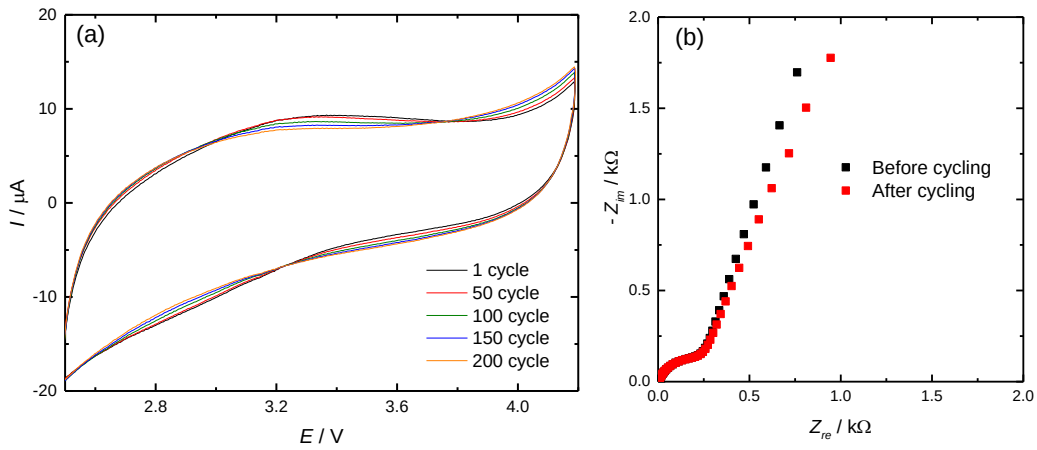

Figure 5.9. a) CV at a scan rate of 50 mV s^{-1} for 200 cycles b) EIS at OCV 500 mHz - 100 kHz and 10 mV AC amplitude, before and after 200 cycles ; electrolyte used: 1:1 EC:EMC + 1 M $LiPF_6$. Reproduced from own publication (I).

5.4 Conclusion

The obtained results show that PEDOT:PSS has a high thermal stability and porous morphology which can be very beneficial for lithium ion battery applications. No pronounced redox reaction of the polymer bulk is observed in the potential window between 3 to 4 V in aprotic electrolyte for Li^+ containing electrolyte. Due to absence of

any redox activity, it can be confirmed that the PEDOT:PSS has the high conductivity throughout the operating voltage between 3 to 4V.

However, thicker layers show pseudo capacitive behaviour and a small reversible reduction wave at potentials more negative than 3 V. Electrochemical impedance spectroscopy is performed at different ambient temperatures and the observed behaviour of PEDOT:PSS corresponds to transmission-line behaviour of porous systems. Quantitative evaluation of the impedance data is performed with a modified transmission line model allowing the separation of the electronic and ionic resistance within the polymer film. The results show that the electrical conductivity of the polymer increases with rising temperature, a typical behaviour for semiconductors with a positive temperature coefficient. The performed cyclic voltammetry and impedance measurements reveal that PEDOT:PSS has a high electrochemical stability in the studied potential window during multiple cycling. The performed experiments show that PEDOT:PSS could be used as binder material for positive electrodes in lithium ion battery contributing to the improvement to the electrical conductivity of the electrodes.

6 Processing of composite electrode

The proposed two-component composite electrodes are prepared by using $LiFePO_4$ as active material and PEDOT:PSS as binder. In this composition, PEDOT:PSS completely replaces the conductive additive (carbon black) and conventional binder (PVDF). Conventional PVDF/carbon black composite electrodes are prepared as a reference for comparison. Before preparation of the composites, the slurry behaviour of $LiFePO_4$ with new conductive binder PEDOT:PSS is studied using rheology. The influence of the solid loading of the slurry on the electrode properties and behaviour is examined and optimum solvent amount / solid loading is determined for a better coating on aluminium current collector.

6.1 Rheology

The rheological behaviour of PEDOT:PSS is studied at 25 °C in parallel plate configuration as described in the section 3.5. The behaviour of the shear stress and the viscosity of the suspension as a function of the shear rate are shown in Figure 6.1. The shear stress rises with shear rate and follows power law type behaviour as explained in the theory section. At low shear rates the viscosity increases and decreases after a certain threshold. This decrease in viscosity is typical for a shear thinning polymer suspensions. Viscosity increase at very low shear rates could be caused by the Newtonian plateau behaviour shown by the entangled polymers at low shear rate (129). According to this phenomenon, the polymers are not entangled and free to move when shear movements are applied. The rheological behaviour of the aqueous PEDOT:PSS suspension show similar rheological behaviour as conventional water based binder used in lithium ion battery such as sodium carboxymethyl cellulose (CMC) systems (130).

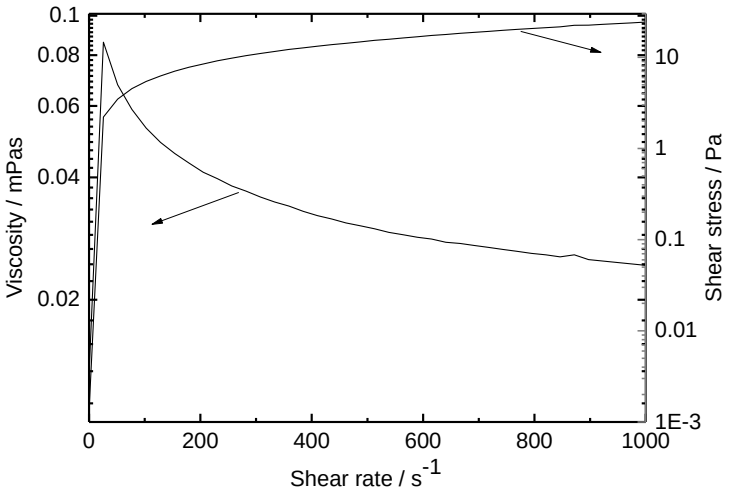

Figure 6.1. Rheological behavior of PEDOT:PSS.

As mentioned in the section 3.5, the composite slurry with different solid loading (solid/solution) is prepared and studied to understand the influence on the electrode, which is crucial for the electrode preparation and application.

Steady state flow tests are performed on these slurries in the rheometer using the parallel plate geometry as mentioned in the (section 3.5) with shear rates between 0 to 1000 s^{-1}. The shear stress increases with shear rate (Figure 6.2a) and follows a power law type behaviour. It can be explained very well in terms of Hurschel-Bulkley model described in section 2.5.1. For different solid loading, the power coefficient *n* can be calculated from equation 2.10. The obtained values of *n* are shown in Table 6.1. In all cases *n* is less than 1, which shows a shear thinning fluid behaviour for all studied slurries. At low shear rate ($\approx 0.1\ s^{-1}$), the slurries show a significant yield stress ranging from 5 Pa for 24 % to 500 Pa for 45 %. These values are comparable to PVDF slurries at low shear rates, which are in the range of 15 Pa for slurries with 27 % solid loading with N-methyl pyrolidon (NMP) as a solvent (15, 131). Figure 6.1b shows a logarithmic plot of the shear stress and the viscosity as a function of the shear rate. All the composite slurries show a decrease in viscosity with increasing shear rate confirming the shear thinning behaviour. In addition, the yield stress rises with increasing solid loading. This behaviour is typical for flocculated dispersions where the presence of weak attractive forces between the particles leads to the formation of particle cluster called flocks. At a certain solid loading, these flocks interconnect with each other giving rise to a weak network structure (132). The yield stress arises due to the presence of weak network structure present in the slurry. The interconnected particles in the

network can transmit force and support shear stress. With increasing solid loading, the connectivity throughout the system improves and the yield stress increases.

Table 6.1. Calculated power coefficient from equation 2.10.

Solid Loading	**Power coefficient (*n*)**
24	0.32
32	0.23
40	0.20
45	0.16

However, the steady state flow tests provide sufficient information only for purely viscous system. The used composite slurries represent viscoelastic fluids due to presence of the PEDOT:PSS polymeric binder. In this case more detailed information can be obtained by dynamic oscillatory shear measurements (15, 101) as described in the section 2.5.1.

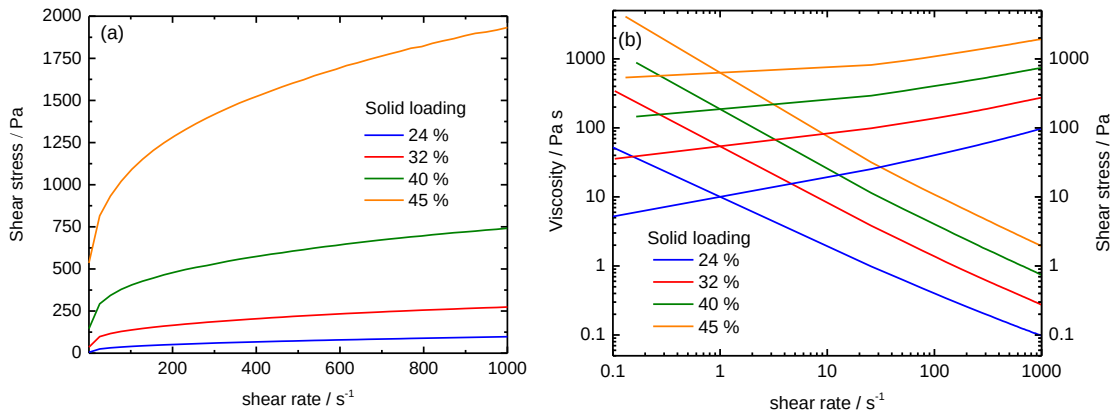

Figure 6.2. a) Shear stress as a function of shear rate for composite slurries with different solid loading; b) Shear stress and viscosity vs. shear rate on a logarithmic scale. Reproduced from own Publication (II).

Dynamic oscillatory shear measurements are performed by applying small amplitude shear stress on the slurries with different solid loadings. Three kinds of measurements are performed.

1. Amplitude sweep measurements
2. Frequency sweep measurements
3. Simulating the coating conditions in parallel plate rheology measurements

For amplitude sweep measurements, a sinusoidal angular velocity is applied on the upper plate of the viscometer as described by Equation 2.12. The stress applied on the fluid can be described using Equation 2.17. At very small strain amplitude γ_0 the fluid structure is not disturbed. The measured stress at this strain is controlled by the rate of spontaneous rearrangements or relaxation present in the fluid in the quiescent or equilibrium state (15). This region is called linear elastic regime. It can be determined by knowing the maximum shear amplitude at which the storage modulus of the slurry starts to decrease due to disruption of the slurry structure. The evolution of storage modulus (*G'*) with shear amplitude for all slurries is shown in the Figure 6.3a. It can be seen that *G'* values do not change up to a certain strain value and subsequently started to decrease for all samples. Hence the viscoelastic regime for the composite slurries lies between shear strains of 0.1 % to 1 %.

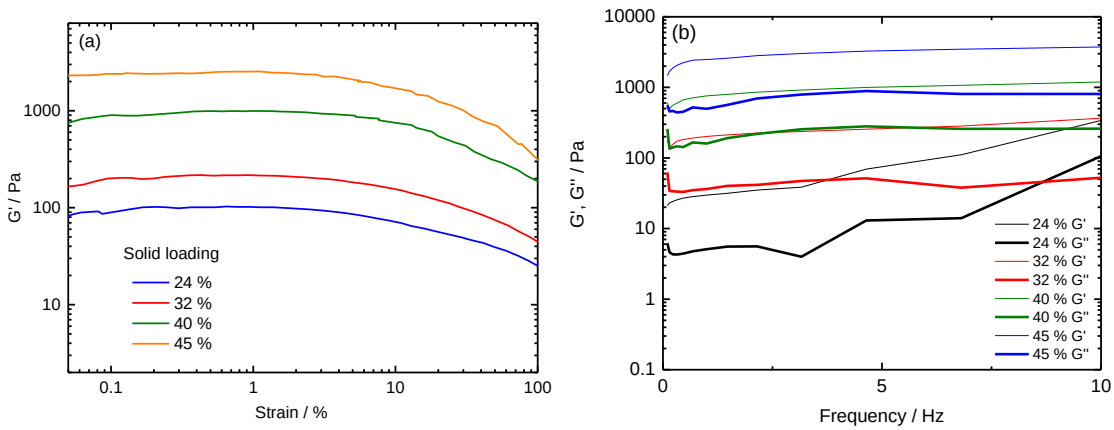

Figure 6.3. Small amplitude oscillatory shear measurements of the composite slurry a) storage modulus *G'* as a function of shear strain at a frequency of 1 Hz (amplitude sweep); b) storage modulus *G'* and loss modulus *G''* as a function of frequency at shear strain of 0.4% (frequency sweep). Reproduced from own publication (II).

Frequency sweep measurements are performed by applying shear rates with different frequency ranging from 0.1 to 10 Hz in the linear elastic regime of the composite slurries (i.e. 0.1-1 %). The objective is to understand the influence of frequency on slurry storage and loss modulus. Figure 6.3 shows the frequency sweep of the composite slurries at various frequency ranges. The shear and loss modulus is independent for frequencies from 0.1 Hz till 10 Hz for samples with solid loading as high as 40 % and 45 %. For lower solid loadings (24 % and 32 %), the observed variation of the moduli with the frequency indicates its fluidic behaviour. This can

influence the distribution of particle agglomeration in the composite electrode during the coating process. However, the storage modulus (*G'*) dominated the loss modulus (*G''*) in the measured frequency range reflecting a solid like behaviour in all cases. Thus the settling of the active material particles in the studied slurries is unlikely. The interaction between particles in the slurry determines its viscoelastic behaviour. When the attractive forces dominate the inter-particle interaction at smaller strains, the slurry behaves like a solid. In this case the active particles form network like agglomerates and can bear stress (133, 134). When the particles are isolated from each other and well dispersed, a fluid-like rheology is observed and in this case the active material settle giving an uneven distribution of particle throughout the cross-section.

In order to simulate the doctor blade coating conditions, the slurry is pre-sheared at the same rate as used in the doctor blade process (6.7 s^{-1}) for 10 s and then a sequence at constant strain and frequency for next 1000 seconds as described in the section 3.5.1. in all cases *G'* dominated *G''* over the 1000 s (Figure 6.4). Hence, a solid-like behaviour is observed which is favourable for avoiding any settling of active material. This behaviour is consistent with our observation of high yield strength for the slurries in the steady state flow measurements which is shown in the Figure 6.2. The motion of the doctor blade forces the composite slurry to flow which breaks the internal structure. However, due to Brownian motion of the particles and macromolecules and also due to inter-particle attractive forces the structure spontaneously rebuilds when it is allowed to stand at rest (15). These rearrangement and rebuilt process of the slurries can be correlated directly with the evolution of storage and loss moduli because the applied strain amplitude is very small.

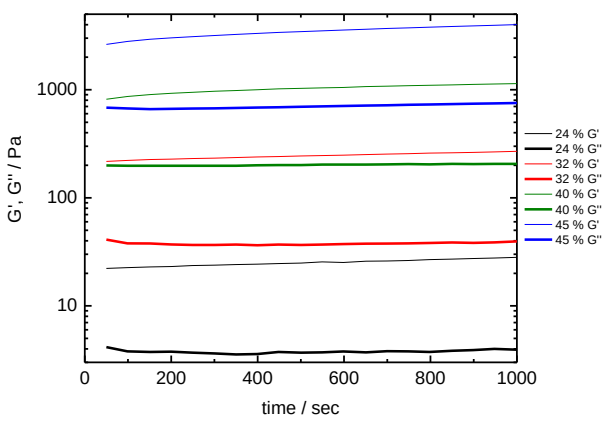

Figure 6.4. *G'* and *G''* vs. time at a frequency of 1 Hz and a shear strain of 0.4. Reproduced from own publication (II).

6.2 Particle interaction in the slurry

As described in section 2.5.1, relative viscosity is a convenient means to understand the inter-particle interaction. The effect of only particles in the slurry rheology behaviour can be explained with relative viscosity. Figure 6.5 shows the relative viscosity of slurries with different solid loadings with shear rate. The relative viscosity for all slurries decrease with shear rate which shows a shear thinning behaviour and suggests that the attractive forces between particles are higher than the repulsive forces and agglomeration is probable (135). The relative viscosity at 1 S^{-1} shear rate is plotted with the volume fraction φ of the active materials in Figure 6.5. It shows power law behaviour with negative n, and can be described by Equation 2.20 as shear thinning fluids of high solid loading. Hence, it can be concluded that the van der Waals attractive forces are dominant over the repulsive interaction of the particles in the slurry with PEDOT:PSS as binder (136).

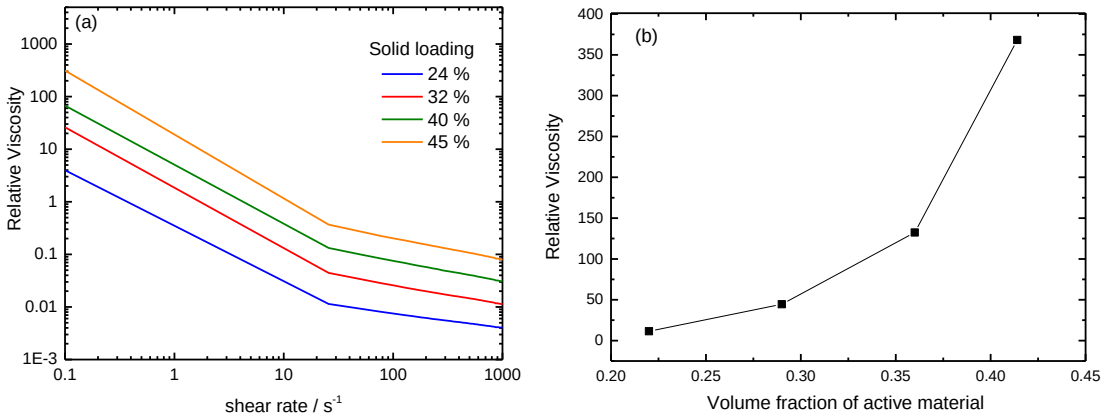

Figure 6.5. Relative viscosities of the composite slurries (a) with shear rate (b) with volume fraction of active material ($LiFePO_4$).

To understand the interaction of PEDOT:PSS polymer chains with the $LiFePO_4$ particles, the zeta potential of the dispersion with low concentration of $LiFePO_4$ in water suspension of PEDOT:PSS is measured at different pH. The pH is adjusted using diluted sodium hydroxide (NaOH) and hydrochloric acid (HCl) solutions. The zeta potential does not change significantly in pH range 4 to 12 (Figure 6.6) due to presence of PEDOT:PSS. In colloid system steric stabilization is achieved by the interaction of polymer with the particles when the zeta potential value becomes close to zero (137, 138). Hence it can be concluded that polymers are not adsorbing on the active material

surface to provide steric stabilization. Moreover, the non-adsorbing PEDOT:PSS may cause depletion flocculation supporting the agglomeration of the active material (136).

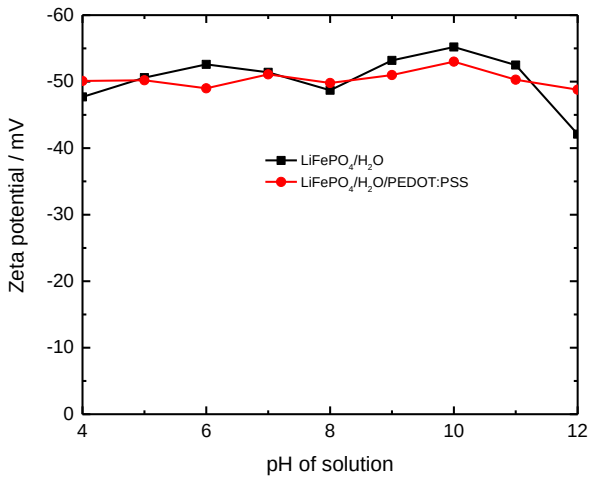

Figure 6.6. Zeta potential of the $LiFePO_4$ at different pH values, in the presence and absence of PEDOT:PSS.

6.3 Physical properties of composite electrodes

After studying the rheological behaviour of these slurries, electrodes are prepared by casting the slurries on plasma-treated aluminium current collectors by the doctor blade technique as described in section 3.3. The coatings are dried in a vacuum oven and then compressed using a rolling machine. The physical properties and electrochemical performance of these coatings are studied to understand the effect of flow behaviour of the slurries on properties and performance of the coating. Due to the very high viscosity of the slurry with 45 % solid loading, the electrode casting under the used coating conditions such as coating speed, thickness and drying procedure is not reproducible. Therefore, in the following section only the properties and the behaviour of the electrodes casted from 24 %, 32 % and 40 % solid loading are discussed.

6.3.1 Porosity measurements

The mercury intrusion porosimetry is used to study the morphological behaviour of the composite electrodes. With increase in solid loading, the porosity of the composite positive electrode decreases (Table 6.2). For the 24 % solid loading the porosity is 49 % whereas for 32 % and 40 % it reduces to 42% and 39 %, respectively. This can be due

to denser particle packing in the slurry at high solid loading (131, 139). In order to obtain more information from porosity measurement data pore size distribution is evaluated. In composite electrodes pores are created due to evaporation of the solvent from the coating which consists of particles, agglomerates and binder. Thus, the pore size is influenced by the size of the primary particles and agglomerates (140). From the pore size distribution (Figure 6.7) two distinct pore size regions can be seen for all composite electrodes. One of regions is in mesopore (10 to 30 nm pore diameter) and another is in macropore (> 300 nm pore diameter). The pore size distribution broadens and the number of mesopores decreases with increase in solid loading. Such broadening in the pore size distribution is often correlated with a decrease in the agglomerate size (140). The volume of pores in the larger pore diameter range increase with increasing solid loading. The results of the porosity measurements reveal that the solid loading of the slurry influences significantly the electrode architecture.

Table 6.2. Physical properties of composite positive electrodes.

Sample solid loading	**Porosity (%)**	**Adhesion strength (N cm^{-2})**	**Thickness of the positive electrode (µm)**	**Sheet resistance (kΩ/ sq.)**
24 %	49	73 ± 15.7	36.8 ± 4.8	19.4 ± 3.3
32 %	42	83 ± 14.4	36.8 ± 1.17	15 ± 0.96
40 %	39	105 ± 8.6	39.6 ± 1.4	10.35 ± 1.1

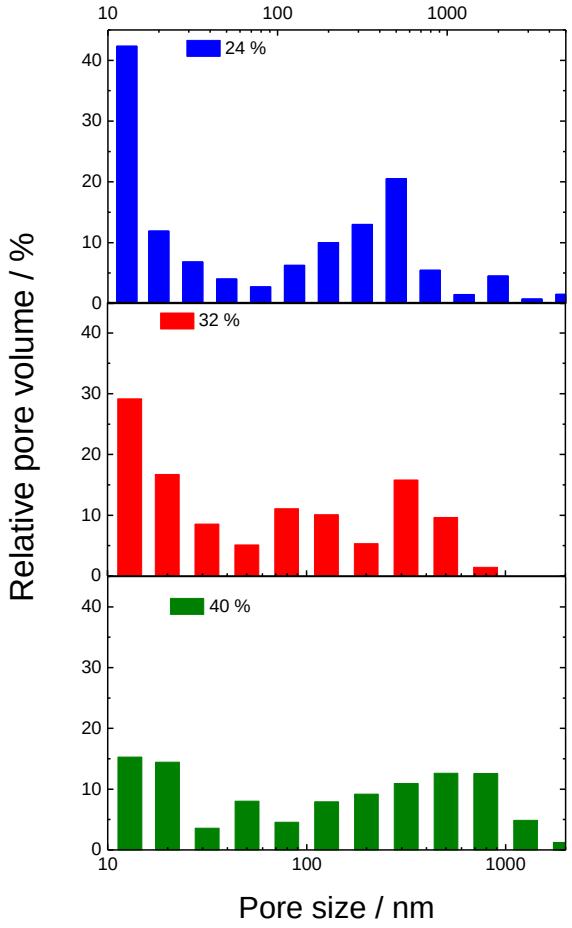

Figure 6.7. Pore size distribution of composite positive electrodes prepared with different solid loading. Figure taken from own publication (II).

6.3.2 Computer Tomography

High resolution nano computer tomography (CT) measurements are performed to study the particle distribution within the different electrodes. Due to difference in the density and correspondingly in the X-ray absorption of the PEDOT:PSS binder and $LiFePO_4$, only active material particles can be resolved by adjusting the threshold of the CT. This is already shown for conventional $LiCoO_2$ positive electrodes (141). Figure 6.8 shows representative CT images of active material alone in electrodes with different solid loading. The visible structures represent the $LiFePO_4$ active material within the composite electrodes. No distinct particle settling is visible in very good agreement with the rheology data. The active material particles possess irregular shapes and at high solid loading they are densely packed. As shown in the CT image the 24 % solid loadings electrodes are very inhomogeneous and exhibit a low amount of randomly distributed $LiFePO_4$ particles. With increasing solid loading of the slurry, the

distribution of the particles becomes uniform which improve the active material utilization within the electrodes significantly. To quantify these observations, reconstructed Volume of Interests (VOI) has been binarized and morphometric parameters are calculated in three dimensional analyses using the CT-analyser software (Table 6.3).

Euler analysis provides a measure of connectivity density indicating the number of redundant connections between structures per unit volume and the Euler number can be used as an indicator of connectedness of the analysed particles (142). The Euler analysis of the CT images show that the Euler number rises with increasing solid loadings revealing increased agglomeration of the active material particles. This observation is in good agreement with the steady state rheology measurement suggesting the appearance of flocculated particle clusters in the slurries with high solid loadings. Moreover, the low Euler number value for the 24 % solid loading electrodes shows that the particles are rather isolated from each other, which can be also seen in the reconstructed CT image (Figure 6.8).

The volume occupied by the active material within the analysed VOIs also behaves in a similar manner indicating the increase in the active material amount within the electrode structure. In addition, comparison of the surface area of particles to the total analysed volume ratio for the different electrodes, it is apparent that the ratio rises exponentially with increasing solid loading.

Another parameter which can be used to evaluate the particle density within a three dimensional structure is called structure linear density. The structure linear density implies the number of traversals touching the particles per unit length by a random linear path through the volume of interest. The value obtained for the 40 % solid loading is several orders of magnitude higher in comparison to the lower solid slurry loading electrodes (Table 6.3) revealing denser particle packing in good agreement with the obtained lower porosity values. Therefore, all the evaluated parameters from the nano-CT pictures show that the intermixing of the PEDOT:PSS binder and the $LiFePO_4$ active material particles is inefficient and poor at slurries with low viscosity leading to inhomogeneous structure and bad active material utilization. For samples prepared by highly viscous slurries the particles density is much higher and the distribution more homogeneous. As a consequence the utilization of the particles is better within in the electrode structure and higher capacity values and reproducible behavior are expected.

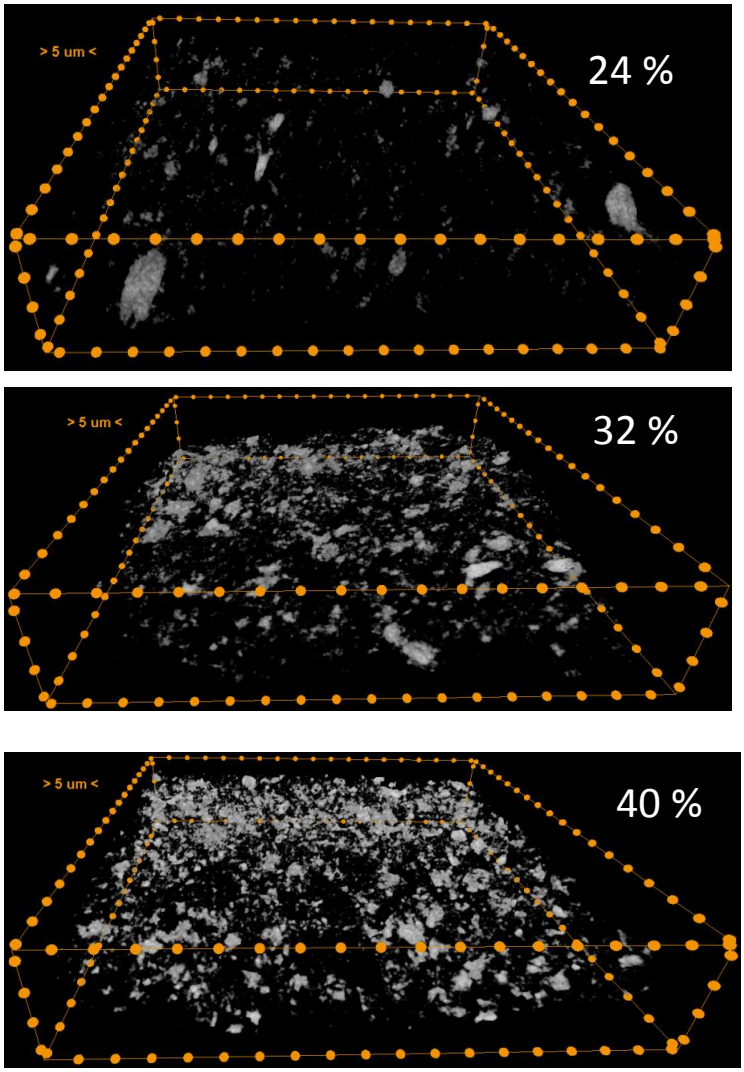

Figure 6.8. Nano computer tomography (CT) images of the composite electrodes prepared with different solid loading samples. Reproduced from own publication (II).

Table 6.3. Quantitative evaluation of binerized nano-computer tomography measurements (II).

Morphometric parameters of the $LiFePO_4$ particles	**solid loading of the composite electrode slurry**		
	24 %	32 %	40%
Euler Number	15	113	416
Structure surface/ total volume ratio (μm^{-1})	0.00156	0.01345	0.18704
Structure volume/ total volume ratio (%)	0.07	0.62	10.96
Structure linear density (μm^{-1})	0.00031	0.00277	0.03799

6.3.3 Mechanical properties

One of the crucial roles of binder is to provide adhesion strength to the coating to the current collector. Various techniques such as peel, pull off and scratch tests are used and discussed to evaluate the adhesion of such electrode coatings to the metal current collector (105, 143, 144). The applied procedures are rather indirect and the results are strongly dependent on the experimental setup for example on the type of the adhesive tape used in peel tests (143). It has been also shown that experimental parameters such as data acquisition rate for the measurements, pull off velocity of the tape and contact stress between the adhesive tape and the electrode coating have a big influence on the calculated adhesive stress values in pull-off test setup (105). However, the pull-off method provides a good basis for semi-quantitative evaluation of the adhesion strength of the electrodes to the current collector. Thus this method is implemented for the prepared coatings to compare the adhesion of the electrodes to the aluminium current collector as a function of the solid loading of the slurry. The adhesion strength of the coatings on the current collector (Al) can be calculated by equation [6.1]

$$\sigma = \frac{F_{t,max}}{A} \qquad [6.1]$$

Here $F_{t,max}$ is the maximum applied tensile force to peel the coating out of the aluminium foil and A is the area of the composite electrode used for the measurement. Table 6.2 shows the adhesion strength and its standard deviations for coatings prepared from slurries with different solid loading. For each coating at least 8 different samples are tested and the standard deviation has been calculated. It can be seen that, the mean adhesion strength of the $LiFePO_4$/PEDOT:PSS coatings varied in dependence of the slurry solid loading from 70 to 105 N cm^{-1}. The 40 % solid loading sample showed the highest adhesion strength (105 N cm^{-1}) and the lowest standard deviation. The low deviation of the adhesion strength values can be due to uniformity of the coatings which is in good agreement with the nano CT images. Although the mean thickness is about 40 µm for all electrodes, an increased deviation can be observed for the electrodes prepared from slurries with lower solid loadings revealing the inhomogeneity of these coatings in good agreement with the frequency sweep rheology results (Figure 6.3b). Since the samples prepared with slurries of lower solid loading (24 % and 32 %) showed more fluidic behaviour as compared to 40 % solid loading slurry sample, the agglomerates are distributed non-uniformly over the coating causing deviation in the electrode properties. In order to compare the obtained values to state of the art

electrodes, the adhesion strength of commercially available single side coated $LiFePO_4$/PVDF/CB electrodes from MTI is measured via the same adhesion test procedure. The values for the adhesion strength of these samples on the aluminium current collector are in the range of 35 to 40 N cm^{-1}, which are in the same order of magnitude as the values observed for the PEDOT:PSS samples. However, it should be pointed out that the improved adhesion of the PEDOT:PSS coatings may originate not solely by the properties and the amount of the used polymer but also by the performed plasma pre-treatment of the aluminium current collector. To understand the effect of plasma treatment, 40 % solid loading slurry has been casted on non-plasma treated Al collector and the adhesion strength is examined using the same procedure. The value of 55-65 N cm^{-1} is obtained in this case which reveal that the adhesion strength of the electrodes is significantly improved by the plasma treatment. However, these values are still slightly higher than the commercial PVDF containing electrodes confirming that PEDOT:PSS alone can provide good adhesion of the coating to the aluminium current collector

6.3.4 Electrical properties of composite electrode

The electrical conductivity of the coating is an important parameter for the battery performance specifically at higher rates. The slurries are coated on glass substrates and the sheet resistance is measured by the 4-probe technique. The mean values and their standard deviations for different solid loading electrodes are shown in the Table 6.2. The standard deviations are calculated from the same sample at 3 different locations. The sheet resistances of all samples are in the same order of magnitude. This can be due to presence of the same amount of conductive binder (8 %) in all composite slurries. However, the conductivity trough the thickness of the coatings i.e. the through plane conductivities of the composite positive electrode is important for the electrode performance. Hence the through plane conductivity of the composite electrodes is measured as a function of applied pressure. For all of the coatings under the test conditions, the conductivity values rise linearly with the applied pressure (Figure 6.9). It can also be observed that the 40 % solid loading sample has higher conductivity as compared to 24 and 32 % showing that the uniform distribution of the agglomerates within the electrode has a significant influence on the trough-plane conductivity.

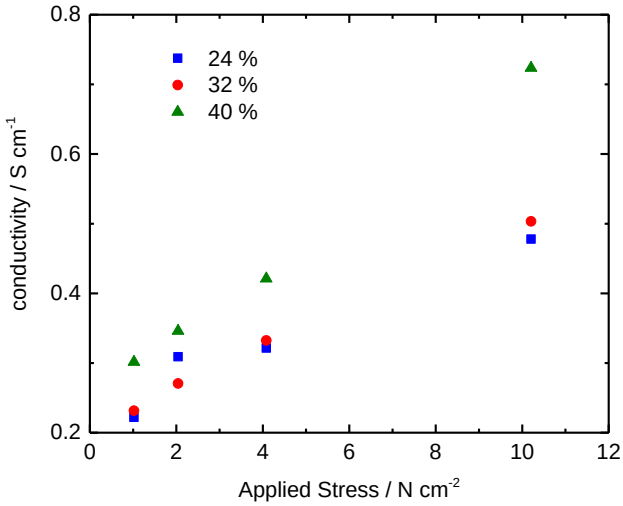

Figure 6.9. Through plane conductivity of the composite electrode verses applied stress. Figure reproduced from own publication (II).

6.4 Electrochemical performance of the composite electrode

After characterizing the coatings made with different solid loading slurries, the electrochemical behaviour of the coatings is studied. Therefore, standard three electrode swagelok cells are prepared using composite electrodes as positive electrode and Li as negative electrode and reference. The electrolyte used for the cells contains 1 M $LiPF_6$ in an aprotic solvent made with 1:1 ratio of EC:EMC. The performance of these cells are studied by galvanostatic charging and discharging of the cells at C-rate of 0.2 (Figure 6.10a). The samples with 40 % solid loading showed the highest average discharge capacity of approximately 130 mAh g^{-1}. For the positive electrodes made with low solid loading slurries, the capacity values at 0.2 C are less than that for 40 % solid loading. The decrease in the discharge capacity for electrodes with lower content of solids is related to the incomplete utilization of the active material due to the electrode inhomogeneity. As mentioned already, the coatings made with 24 % and 32 % solid loading slurry shows a more liquid-like behaviour than the 40 % solid loading sample. Hence inhomogeneous distribution of the active material is present in the coatings which are supported by nano CT images (section 6.3.2) and adhesion strength data (section 6.3.3).

For comparison to conventional system, electrodes containing PVDF and C-black with 84 % of the same $LiFePO_4$ active material are prepared and tested in a swagelok cell using the same electrolyte and counter electrode. The discharge

gravimetric capacity ($LiFePO_4$ specific) of the PVDF electrode is 133 mA h g^{-1} which is slightly higher than the 40 % solid loading sample with PEDT:PSS (Figure 6.10). However the gravimetric capacity values for all composite electrodes are much lower than the theoretical capacity of $LiFePO_4$ active material which is 169 mAh g^{-1}. It is well known that the electrochemical properties of $LiFePO_4$ are directly correlated to the amount of carbon, its coating thickness, uniformity and used carbon precursor (145, 146). Thus, it can be concluded that the used PEDOT:PSS binder does not cause the low specific capacity rather it is due to low capacity of the used active material ($LiFePO_4$). Moreover, higher gravimetric capacity is obtained for the PEDOT:PSS/$LiFePO_4$ composite than for the conventional system using the same active material and considering the total electrode mass of the composites.

Figure 6.10b shows a comparison of the rate capabilities of the composite electrodes. All composite positive electrodes are charged at rates between 0.5 C and 5 C and discharged at 0.5 C. The mean values are normalized to the discharge capacity at 0.5 C and the error bar shows the standard deviation of the capacities from 3-5 different Swagelok cells prepared from the coatings made with different solid loading samples. At low C-rates, all samples show the same capacity retention behaviour, since the active material properties are dominant at low current densities (147). A difference in the discharge rate capability is observed from C rates higher than 2 C. The rate capability decreased with decrease of the solid loading. This can be explained by the higher electrical conductivity and better active material utilization for the 40 % electrodes. The capacity retention of 80 % at 5 C is observed with samples with 40 % solid loading. For comparison, the capacity retention is 70 % at 5 C of the reference conventional PVDF based electrodes (Figure 6.10b). Moreover, it has been shown for other $LiFePO_4$ electrodes that the capacity retention at 5 C is 65 % for PVDF based coatings with similar thickness of 45 µm, containing 10 % acetylene black (147). The results show that the application of PEDOT:PSS as binder is influencing positively the rate capability of the electrodes. This can be due to the connectivity of conducting polymeric binders in three dimensions within the structure, which improves the overall electronic conductivity of the composite electrode. Moreover, the rate capability of the electrodes can be significantly improved by application of nano-sized active materials and optimized electrolytes (148).

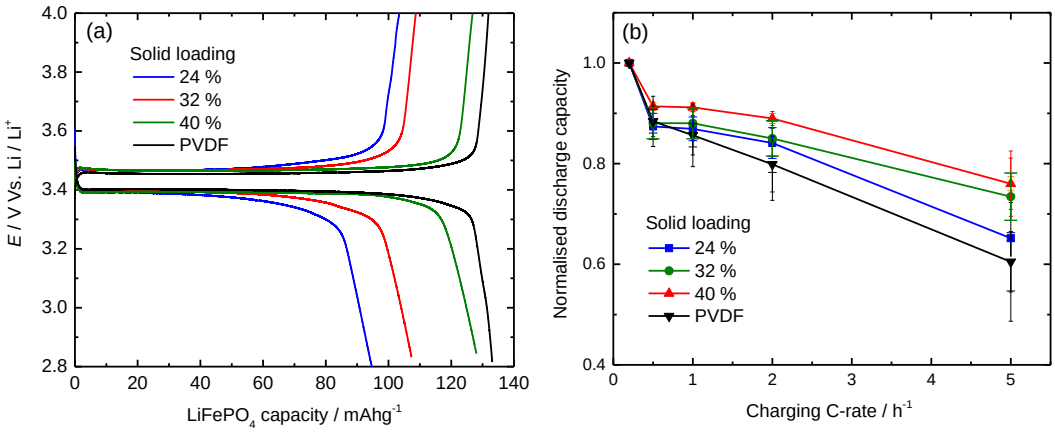

Figure 6.10. a) Charging and discharging behaviour of composite electrodes at 0.2 C. The capacity is normalized by the total $LiFePO_4$ mass; b) Rate capability of composite positive electrode samples at different C-rates.

6.5 Cycling behaviour of the composite electrode

The cycling stability of the cells prepared with the composites of different solid loading is studied by continuous cycling at 1 C between 2.8 - 4 V. At the end of every 20th cycles a capacity test is performed at lower rate of 0.2 C rate. The ratio between the discharge capacities in each cycle to the initial discharge capacity in the 1st cycle is referred to as state of health (SOH) of the cell. In Figure 6.11a SOH is and plotted as a function of the cycle number for the different composite electrodes. In all samples there is an increase in SOH with cycle number, i.e. an increase in discharge capacity with cycling. It is assumed that rearrangement of the composite structure during cycling can cause such behaviour. Figure 6.11b shows the voltage efficiency of different composite electrodes during continuous cycling. The voltage efficiency is higher for samples prepared from higher solid loading slurry (32 % and 40 %). It is in good agreement with the rate capability measurements where higher solid loading samples showed better rate capability due to better three dimensional conductivity. Figure 6.11c shows the columbic efficiency of the composite electrodes for the 100 cycles. It can be observed that for 24 % sample after 60 cycles and for 32 % sample after 80 cycles there is a drop in columbic efficiency whereas 40 % samples show stable columbic efficiency for 100 cycles. This suggests that the amount of irreversible, parasitic reactions in the cell reduces with increase in solid loading. This can be related to the agglomerate distribution in the composite electrode. For higher solid loading sample it is uniform than for samples with lower solid loading as observed from nano CT images.

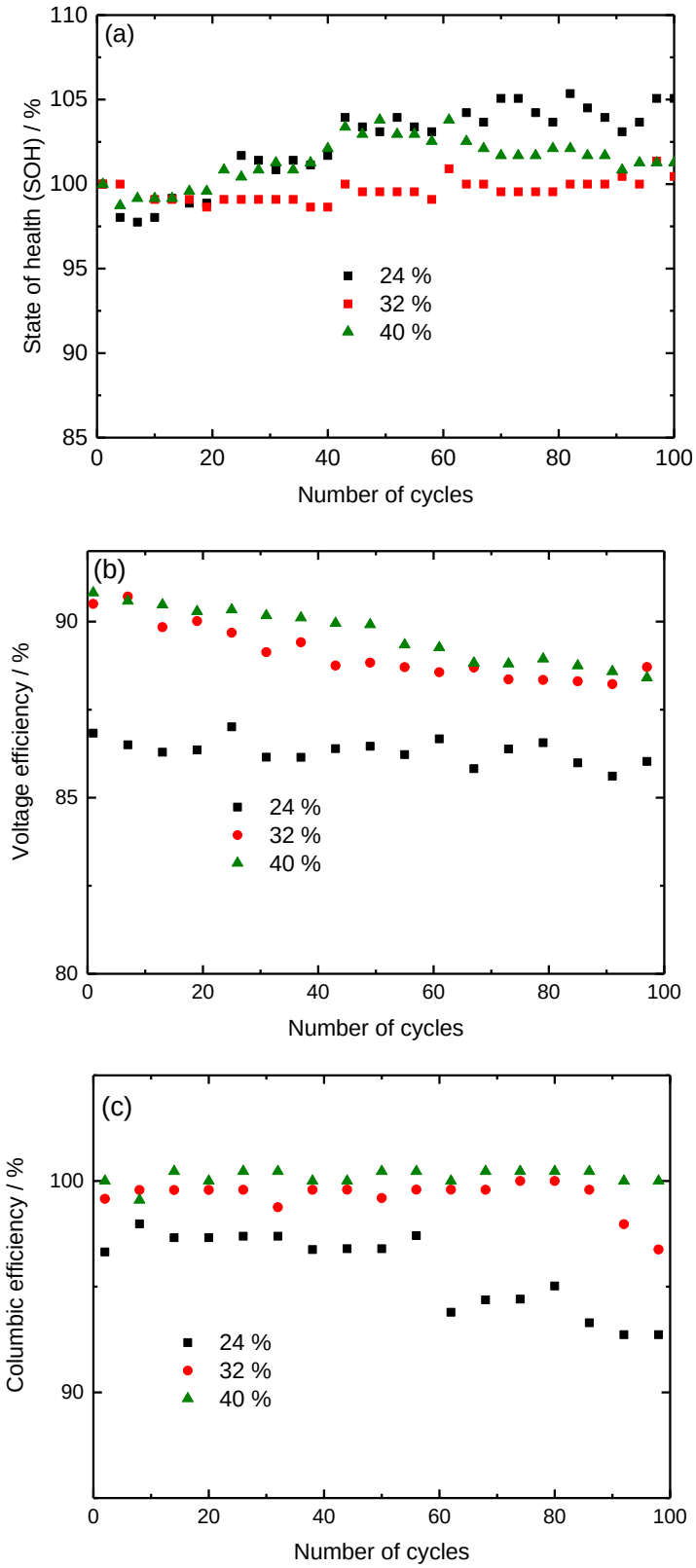

Figure 6.11. a) State of health; b) Voltage efficiency and (c) columbic efficiency of the composite electrodes with number of cycles. The solid lines are guide lines for the eye.

6.6 Conclusion

For the first time, the behaviour of aqueous, two-component slurries consisting of PEDOT:PSS binder and $LiFePO_4$ active material in absence of conductive carbon additives is reported. The influence of the solid loading of the slurry on the electrode properties and performance is evaluated. The solid loading of the slurry from which the electrodes are prepared exhibits a significant impact on the mechanical, physical, morphological and electrochemical properties of the composite positive electrodes. X-ray computer tomography measurements reveal that the utilization of the active material within the composite structure improves by higher solid loading slurries and the electrode shows a more homogeneous particle distribution. With an increase in the solid loading to 40 %, better adhesion, higher electrical conductivity and improved electrochemical performance of the resulting positive electrodes become apparent. The rheological measurements show that no settling of the active material particles during the electrode coating process should be expected for slurries with solid loading from 24 % to 45 % due to their high yield stress at low shear rate. This ensures the absence of sedimentation and of a particle-binder compositional gradient through the cross-section. However, with the used coating procedure reproducible coatings are not possible from the slurry with 45 % solid loading. The performed study showed that PEDOT:PSS can be used as functional binder for positive electrodes in lithium-ion batteries providing good adhesion, improved electrode rate capability and the possibility to reduce the amount of inactive material in the electrodes.

7 Effect of PEDOT:PSS amount on the electrodes

After understanding the effect of solid loading of the slurries on the behaviour of the composite electrodes, the next step is to understand effect of PEDOT:PSS binder amount (composition) in the composite electrode on the properties and performance of the electrode. For these studies, composite slurries are prepared with different composition of PEDOT:PSS/$LiFePO_4$. The compositions are shown in the Table 3.2. The prepared composite electrodes is referred in this chapter to the amount of binder used for the processing, i.e. 6 %, 8 % and 16 %. The solid loading of the slurries for the 6 % and 8 % sample is 40 %. However, uniform coatings are produced for 16 % samples with slurry of solid loading 24 % due to presence of higher amounts of binder. For comparison to conventional systems, composite electrodes prepared with PVDF and carbon black also are prepared (Table 3.2). This electrode is named as PVDF throughout the chapter. After slurry casting and drying of the electrodes, different analytical techniques are used to study the morphology, physical properties and electrochemical behaviour of these composite positive electrodes.

7.1 Physical properties and morphology of the composite electrode

In order to calculate the composition of the coatings, thermogravimetric analysis is performed. In the Figure 7.1, the weight loss of the composite electrodes is plotted for temperature up to 800 °C. For reference measurements, only PEDOT:PSS and $LiFePO_4$ behaviour is also been studied and plotted. It can be seen that $LiFePO_4$ is very stable in this temperature range showing insignificant mass loss. There is a 60 % mass loss in the case of PEDOT:PSS alone which is expected. The amount of binder for the composite electrodes has been calculated considering the weight loss for the pure $LiFePO_4$ and PEDOT:PSS (Table 7.1). It can be seen that the amount of polymer is almost the composition of polymer in the slurry. It can be seen that the composite electrode contains the expected amount of polymeric binders.

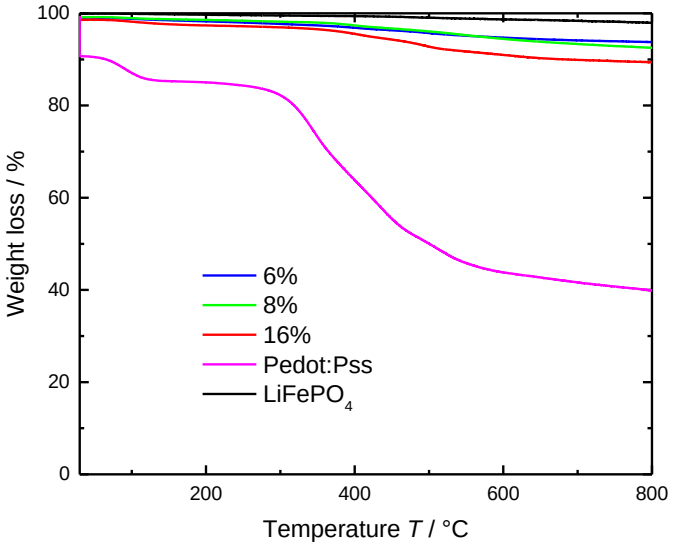

Figure 7.1. TGA of the composite electrodes.

Table 7.1. Electrical conductivity of composite polymers

Sample	**% of binder from TGA measurements**	**Electrical Conductivity (S cm^{-1})**
Polymer	-	2
6 %	5.6	0.0031
8 %	7.9	0.04
16 %	15.8	0.038

After confirming the polymer content of the coating, the conductivity of the composite is measured by coating them on glass substrates and characterizing them by means of 4-probe conductivity measurement. It can be observed that the conductivity of 6 % sample is much less than the 8 % and 16 % samples. This can be due to presence of lower amount of conducting polymer in the composite electrode. This can have a significant effect on discharging behaviour of the electrodes at high rate.

The structure of the prepared composite electrodes is studied by SEM analysis. Figure 7.2a, b, and c shows SEM images of electrodes prepared from the three different compositions of $LiFePO_4$/PEDOT:PSS. All electrodes have a complex and porous structure and show a similar morphology without any significant differences. From the SEM images it is very difficult to see the distribution of polymer and active material or

agglomerates. Hence another method is necessary to observe the distribution of binder and active material in composite electrodes. As already described in Chapter 3, nano-computer tomography (nano-CT) is used to obtain more information on the bulk morphology of composite positive electrodes. This method allows the separate analysis of the $LiFePO_4$ and PEDOT:PSS due to the difference of the X-ray absorption coefficients of PEDOT:PSS and $LiFePO_4$. The $LiFePO_4$ particles are resolved as bright spots in Figure 1a', 1b' and 1c' indicating the distribution of active material within the composite positive electrodes. The darker areas consist of either binder or pores in the electrode. The nano-CT measurements show that the size of agglomerates of the active material is reduced with increasing content of PEDOT:PSS. The reconstructed tomographic data is binarized and different morphometric parameters is calculated in two dimensional "slice by slice" analyses in order to quantify the observed effects. Since the particles of the active material have irregular shapes, the particle size is estimated as the diameter of the largest sphere which is entirely bounded within the solid surfaces using the distance transform methods (149).

The particle size distribution evaluated from the nano-CT data is plotted in in the Figure 7.3. It can be observed that, the majority of the apparent particles have sizes in the range of 1 to 3 μm. With increasing the amount of binder, the particle size decrease and the particle size distribution becomes narrower. The significantly broader particle size distribution of the positive electrode with 6 % binder indicates the increased tendency for agglomeration in composites with low binder content (Figure 7.3a). The particle separation between $LiFePO_4$ is evaluated by using the distance transformation methods. This space represents the volume occupied by polymer and pores in the composite electrode. As expected $LiFePO_4$ particle separation increases with increasing amount of the polymer binder (Figure 7.3b). The particle separation distribution is broader at high binder contents.

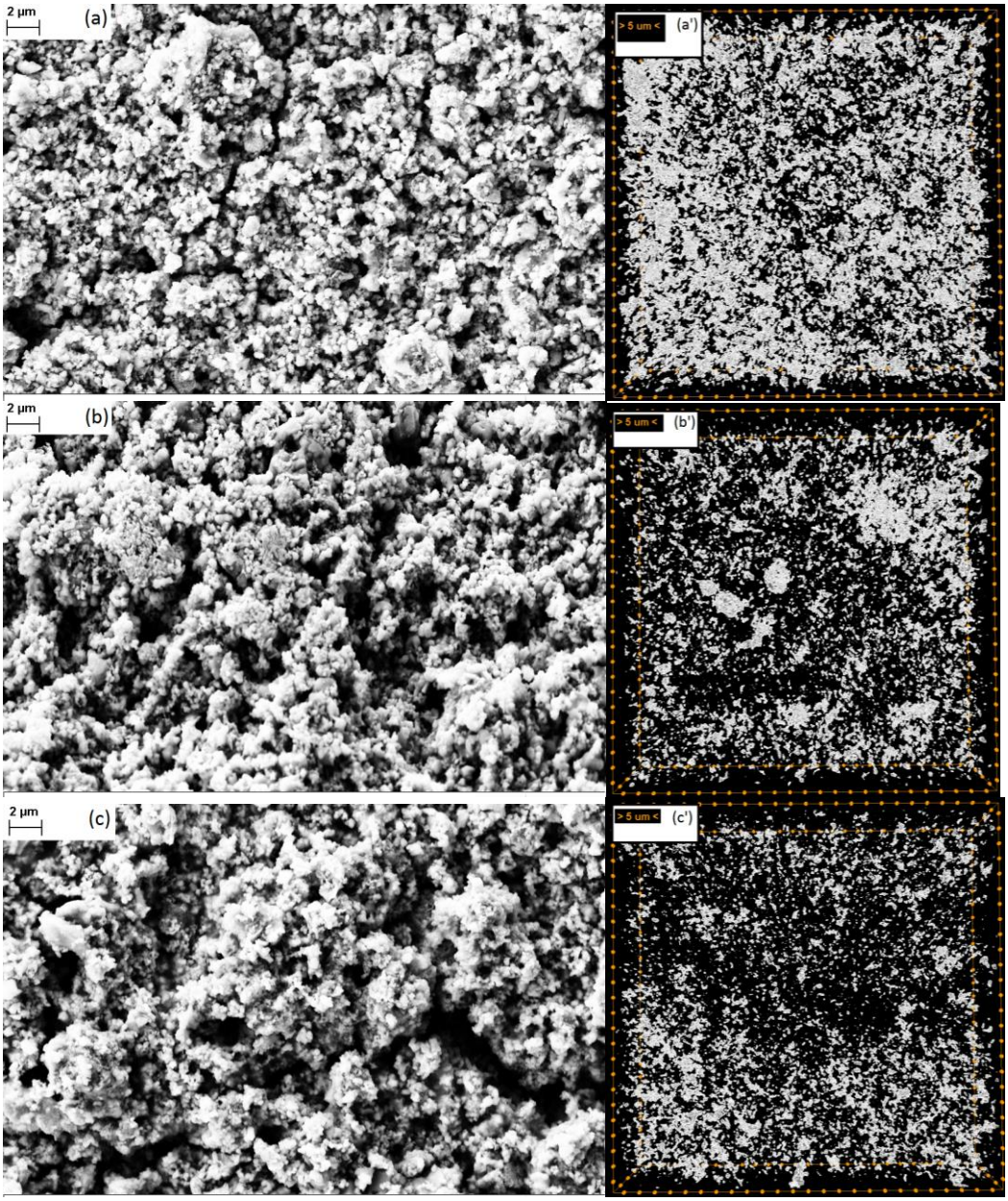

Figure 7.2. SEM (left column) and nano-CT (right column) images of 6 % (a, a), 8 % (b, b) and 16 % (c, c') samples on Al current collector. Reproduced from own publication (III).

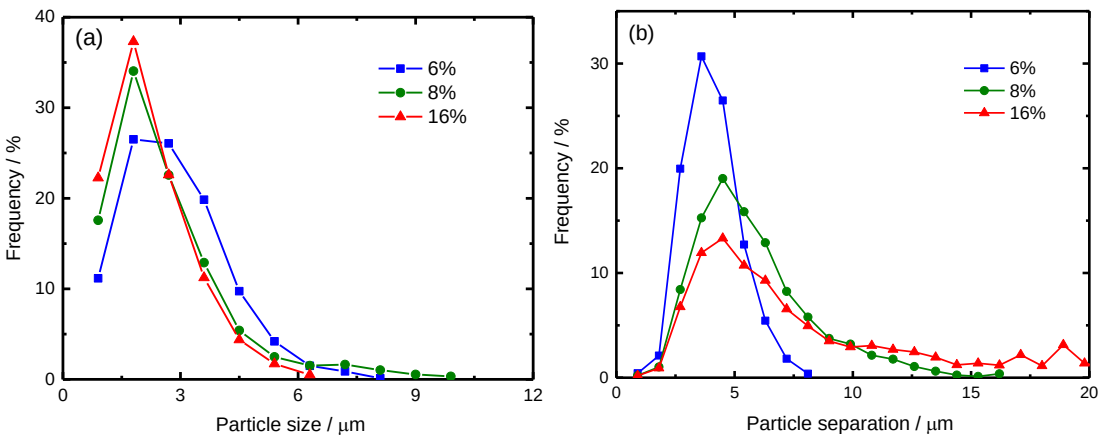

Figure 7.3. Particle size distribution of the active material and (b) particle separation distribution for the composite positive electrodes as evaluated from nano-CT images. Reproduced from own publication (III).

Mercury porosimetry is used to further study the morphological behaviour of the composite electrodes. It is used to study the influence of the PEDOT:PSS amount on the porosity and the pore size distribution of the composites. Despite the calendaring, the 6% sample has 51% total porosity. The porosity of the composite positive electrode decreases with increasing amount of binder. It is 40 % and 31 % for the 8 % and 16 % samples, respectively. Because the density of PEDOT:PSS is much lower than that of $LiFePO_4$, an increase of the PEDOT:PSS mass fraction leads to a strong increase of the binder volume fraction. The polymer can fill any spaces between the $LiFePO_4$ particles and decreases the ratio of the void volume and thereby the porosity of the composite positive electrode (21). Representative pore size distributions for the different composite positive electrodes are shown in Figure 7.3. For the calculation of the pore size distribution, cylindrical pores are assumed and the washburn equation is used. It is described as follows.

$$\Delta \mathrm{P} r = -2\gamma_s \cos\theta \qquad [7.1]$$

Where, ΔP is the pressure difference across the mercury interface, r is the pore radius, γ_s is the surface tension of the mercury and fluid medium (air in this case) and θ is the contact angle of the mercury with the coating surface. Furthermore, a contact angle of 140° and mercury surface tension of 485 dyn/cm is used for the calculations which is already measured and published (150). All three composite positive electrodes show pores in the range from 10 to 2000 nm. For the 16% polymer sample, the small pores of around 20 nm diameter dominate and only a small fraction of pores are in the 1 µm range. In case of 6% and 8% polymer electrodes, the pore size distribution shifts to

larger pores. Hence, with addition of more binder the porosity and the average pore size are decreased. It has been described that the charge transfer resistance of the ions is affected by the size and shape of the pores. Increasing narrowing of the pores (pore funnel) causes a steeper increase in impedance. In expanding pores (pore bottleneck), the impedance reduces strongly (123). Hence the electrochemistry of the system is affected by different pore size distribution.

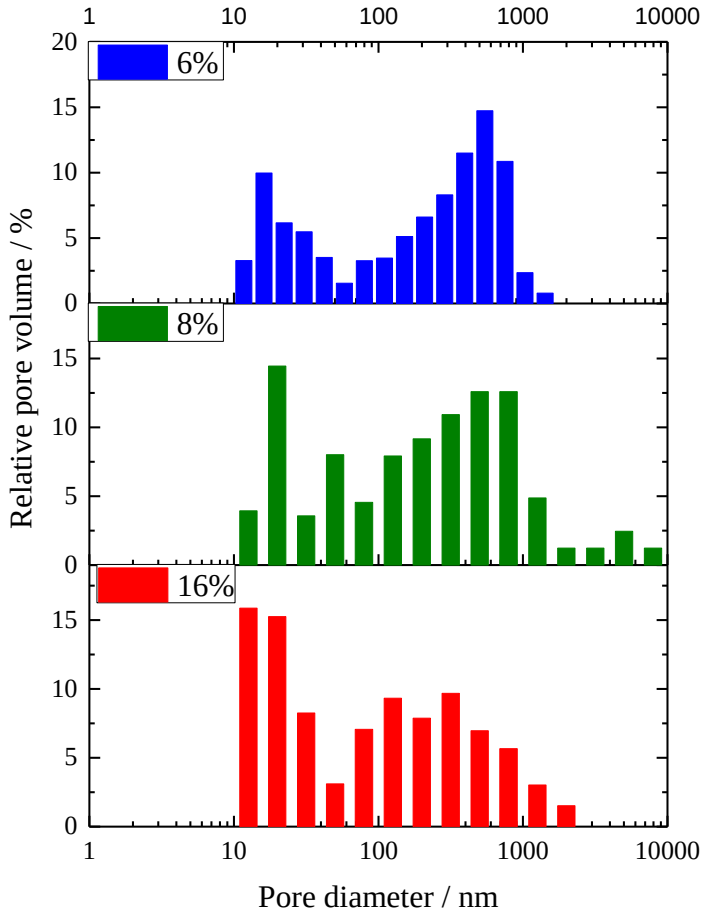

Figure 7.4. Pore size distribution of composite positive electrodes. Reproduced from own publication (III).

7.2 Electrochemical behaviour of the composite positive electrodes

In chapter 2 it is shown that PEDOT:PSS shows stable behaviour in the potential range of 2.8 till 4 V where $LiFePO_4$ is active. There are no significant redox peaks for PEDOT:PSS in this potential range. All the prepared composite positive electrodes are studied in this potential range at a scan rate of 80 μVs^{-1} to understand their redox behaviour. Figure 7.5 shows CVs of $LiFePO_4$/ PEDOT:PSS composites contenting 6%,

8%, and 16% polymer binder. For a direct comparison of the different electrodes, the measured currents are normalized by the electrode mass ($LiFePO_4$ + PEDOT:PSS). The observed redox peaks correspond to the oxidation/reduction of $LiFePO_4$ since PEDOT:PSS is redox inactive in this potential window. With addition of more polymers the apparent kinetics of the redox reaction becomes faster as indicated by the decreasing difference between anodic and cathodic peak potentials for 6 % and 16 % sample. Moreover, with increasing amount of PEDOT:PSS in the composite, the redox reactions start at lower over potential. Hence a better reversibility of the oxidation and reduction reaction is observed with addition of more polymers. This is probably due to the higher electronic conductivity of the composite positive electrodes with higher amount of conducting binder (Table 7.1). Another reason for the better reversibility of the redox reactions is reduction of the size of particle agglomerates (Figure 7.3) with higher amount of polymer. Hence the morphology and agglomerate distribution of the composite electrode influences its redox behaviour in battery electrolyte.

However, for the 16 % sample an additional shoulder appears. The observed feature can be attributed to differences in the diffusion limitation arising in dependence on the pore size. It is found, that for thick porous electrodes the pore depletion becomes significant and the location of the redox peaks depends on the pore depletion rate (20, 151, 152). Generally, small pores are depleted more quickly than larger ones and the peak shifts to lower over potentials with decreasing pore size. Thus the effect of peak splitting observed for the 16 % sample can be attributed to the increased number of small pores in the electrode shifting the main redox peak to lower potentials.

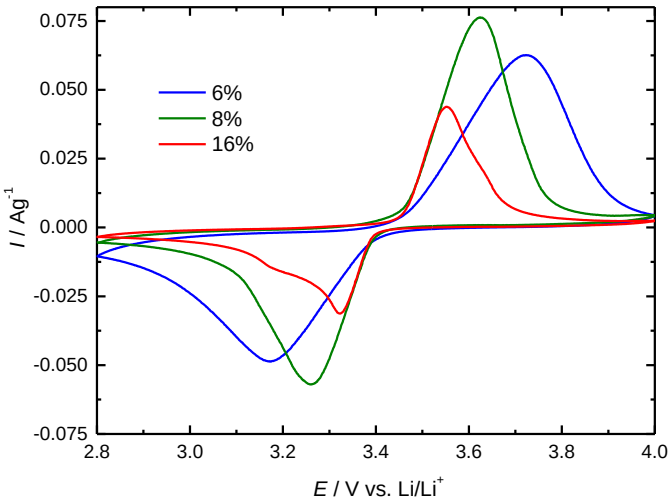

Figure 7.5. CV of positive electrodes with 6 %, 8 % and 16 % PEDOT:PSS binder in 1:1 EC:EMC + 1 M $LiPF_6$ at a $V = 80$ μV s^{-1}. Reproduced from own publication (III).

After studying the CV behaviour of the composite positive electrodes, the battery performances of the cells made with composite positive electrodes are studied by galvanostatic charging and discharging at 0.2 C-rate (Figure 7.5). The behaviour of the composite electrodes is compared to a conventional positive electrode prepared with a PVDF binder and carbon black as mentioned in the section 3.3 (Table 3.2). The electrode capacities are normalized by the total electrode mass including active materials and additives to compare the behaviour of conventional PVDF based electrode and PEDOT:PSS based electrodes. The 8 % sample shows slightly higher electrode capacities than the PVDF positive electrode. The capacity of the 16 % sample is much lower as compared to the 8 % sample. This can be due to two major reasons. Firstly, the amount of active material in 16 % electrode is 84 % whereas in case of 8 % sample it is 92 %. Secondly, the lower porosity in the positive electrode (mentioned earlier) caused by an increased content of binder can hinder the diffusion of Li^+ ions within the electrode and decrease the cell performance in good agreement with the literature (21, 153). The 6 % electrode shows reduced capacity despite the high porosity and increased amount of active material. In addition, high overvoltages can be observed in this case, that is also observed in the CVs of 6 % sample (Figure 7.5). The observed lower capacity is caused by the insufficient amount of conducting binder in the electrode leading to low electronic conductivity of the composite positive electrode. Moreover, the increased agglomeration of the active materials observed in the nano-CT data

(Figure 7.2) can also influence the capacity of the electrode because a fraction of the active material is electronically insulated from the back contact.

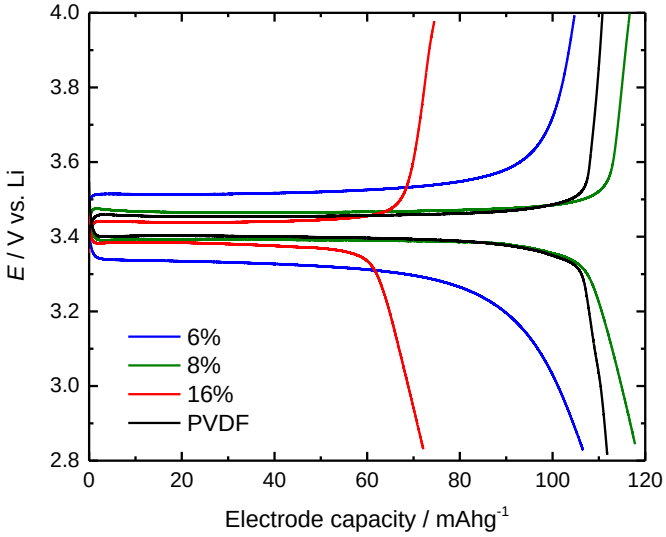

Figure 7.6. Charging and discharging of the composite electrodes at 0.2 C rates. Reproduced from own publication (III).

After studying the charging and discharging properties of the composite electrodes at 0.2 C, the performance at higher rates needed to be studied. Improvement in rate capability is one of the major objectives of the proposed two component composite electrode system. Hence all composite positive electrodes are charged at rates between 0.5 C and 5 C and discharged at 0.5 C to study the charging rate capability. Furthermore, the electrodes are discharged at rates between 0.5 C and 5 C and charged at 0.5 C to study the discharging rate capability of the composite electrodes. The discharge and charging capacity obtained from the above tests is normalized with the value at 0.5 C rates (Figure 7.7). To get a more statistical result 3-5 cells are tested for the calculation of mean values with standard deviations (Figure 7.7). In Figure 7.7a 6 % electrodes show a drastic reduction of capacity at higher C-rates due the low electrical conductivity and increased agglomeration size as mentioned previously. 8 % and 16 % electrodes show enhanced discharge capacity at higher rates compared to the 6 % electrodes. At a charging rate of 5 C, the capacity retention for 16 % and 8 % electrodes are 79 % and 76 %, respectively. The increasing amount of PEDOT:PSS contributes to the reduction of the contact resistance between the electrode and the current collector as already shown in the literature for the polyaniline/$LiFePO_4$ system (90). In case of PVDF electrode, the capacity retention at 5 C charging is 63 %, i.e. much lower than for the 16 % and 8 % electrodes. This is remarkable because carbon black used in the PVDF

electrode has a much higher electrical conductivity (500-1000 S cm^{-1}) than PEDOT:PSS (1 S cm^{-1}). The increase in the rate capability for the PEDOT:PSS electrodes can be caused by the good connectivity of the flexible polymer chains and the inter chain hopping creating more effective conductive bridges in three dimensional electrode than for a mixture of carbon black and an insulating binder. Moreover the three dimensional conductivity of the system is improved making electron transport accessible for all the active material.

The charging rate capability has been shown in Figure 7.7b. It can be seen that the charging rate for 8 %, 16 % and PVDF samples are very similar whereas the 6 % sample shows drastic reduction of capacity at higher rates. This can again be due to presence of insufficient conducting agent and bad adhesion strength.

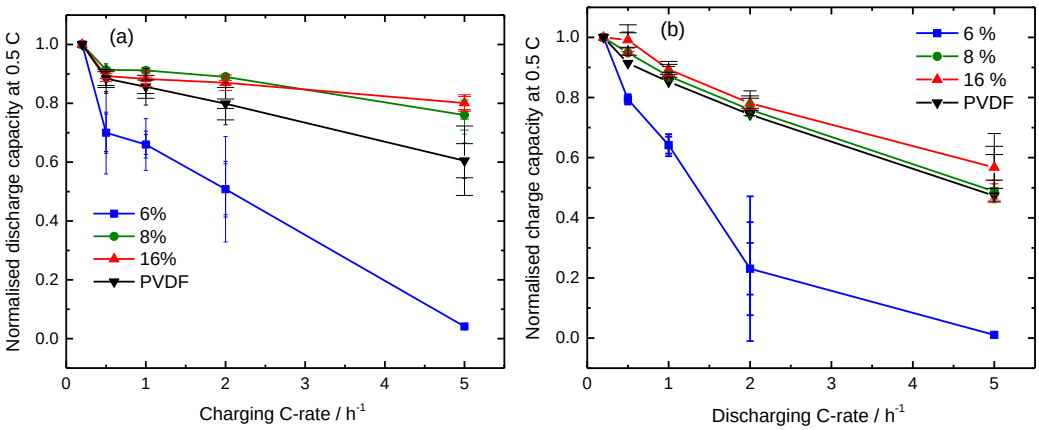

Figure 7.7. Normalised rate capability of composite electrodes.

7.3 Use of PEDOT:PSS binder with conductive carbon black

The composite electrode with 8 % PEDOT:PSS showed highest electrode capacity and very good capacity retention at 5 C charging rate. The next step is to prepare an electrode with both PEDOT:PSS and C-black. As shown in the Table 3.2, a composite electrode is prepared with 8 % PEDOT:PSS and 8 % carbon-black. The capacity of the composite electrode and its rate capability is compared with the 8 % PEDOT:PSS in Figure 7.8.

It can be seen that the capacity decreases slightly due to reduction in the amount of $LiFePO_4$ in the composite electrode. The capacity retention at higher C-rate of 5 C both during charging and discharging improves slightly because of the increase in

electrode conductivity due to presence of carbon-black. However, the intended improvement in the composite electrodes is not achieved. This can be due to the inherent hydrophobic property of carbon black (154). Hence during the slurry preparation, it might segregate and the distribution throughout the composite electrode is bad. Hence further optimization of the carbon black and PEDOT:PSS containing electrodes should be performed in order to obtain better performance.

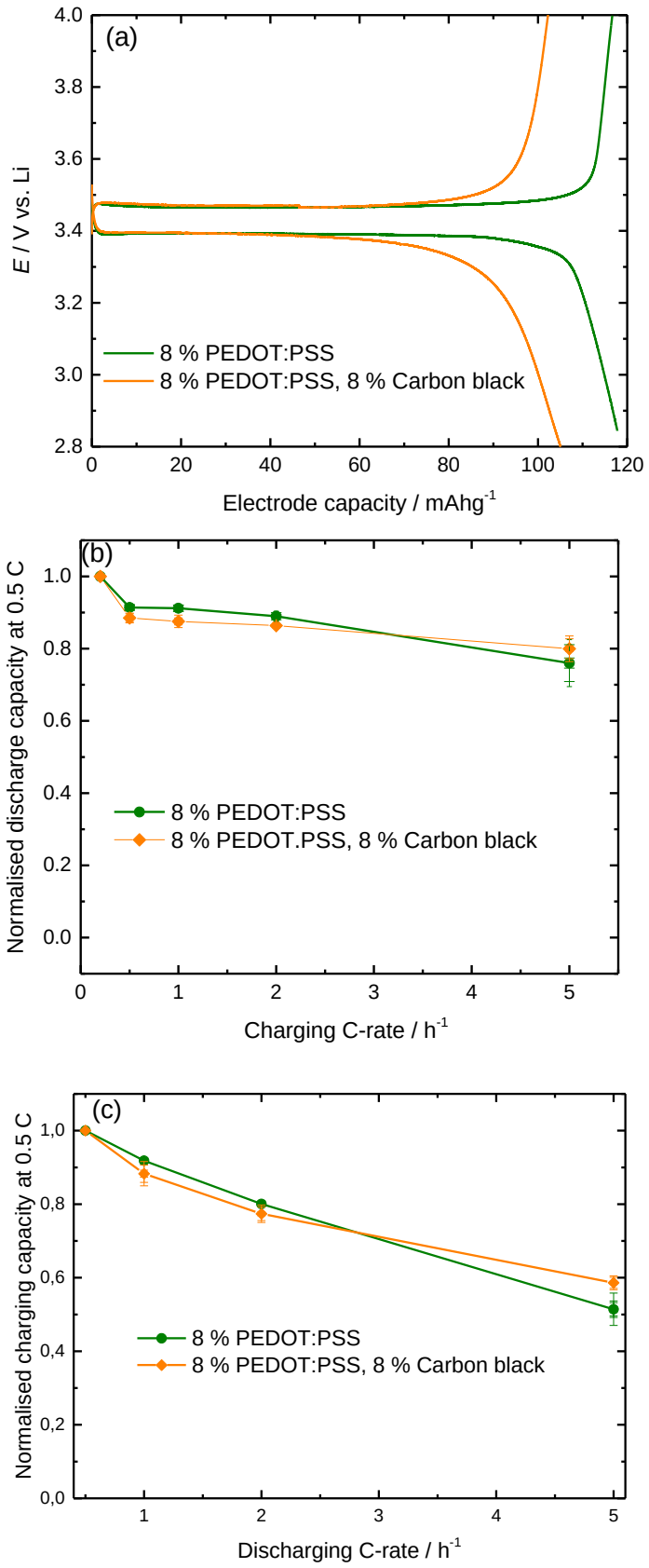

Figure 7.8. (a) Electrode capacity at 0.2 C charging and discharging, (b) rate capability at different C-rate charging of composite electrodes, (c) rate capability at different C-rate discharging of composite electrodes with PEDOT:PSS binder with and without carbon black.

7.4 Cycling behaviour of the composite positive electrodes

The cycling stability of all composite positive electrodes is studied by continuous battery cycling at 1 C in the potential window 2.8-4 V for 100 cycles (Figure 7.9). Every 20th cycle, a capacity test at 0.2 C is performed. The observed fluctuation in the capacity for the initial cycles after each capacity test is in good agreement with literature (155, 156). It can be observed that, there is no significant capacity fading within the 100 cycles for all studied electrodes. The 8 % and 16 % and electrodes show stable cycling behaviour similar to the PVDF sample, whereas fluctuation of the capacity can be observed for the 6 % sample. This behaviour is probably caused by the inhomogeneity and low conductivity of the 6 % electrode. A slight increase in the discharge capacity with cycling can be observed for 8 % and 16 % electrodes, probably due to rearrangement in the composite structures. The voltage efficiencies of these electrodes for the 100 cycles have been plotted in Figure 7.9b. It can be observed that the voltage efficiency of the 16 % sample and 8 % PEDOT:PSS, 8 % C-black sample is comparable to the PVDF sample. The 8 % sample voltage efficiency remains stable up to 100 cycles but the values are less than the PVDF samples, this can be due to a lower conductivity of the sample. The 6 % sample showed the lowest voltage efficiency which further decreased with the cycle number suggesting inhomogeneity and lower conductivity of the composite electrodes. The performed capacity tests at 0.2 C at the 20 cycle interval are shown in the Figure 7.9c. It can be seen that the behaviour is very much similar to the capacity test at 1 C. Hence it can be concluded that there is no degradation of the electrodes taking place.

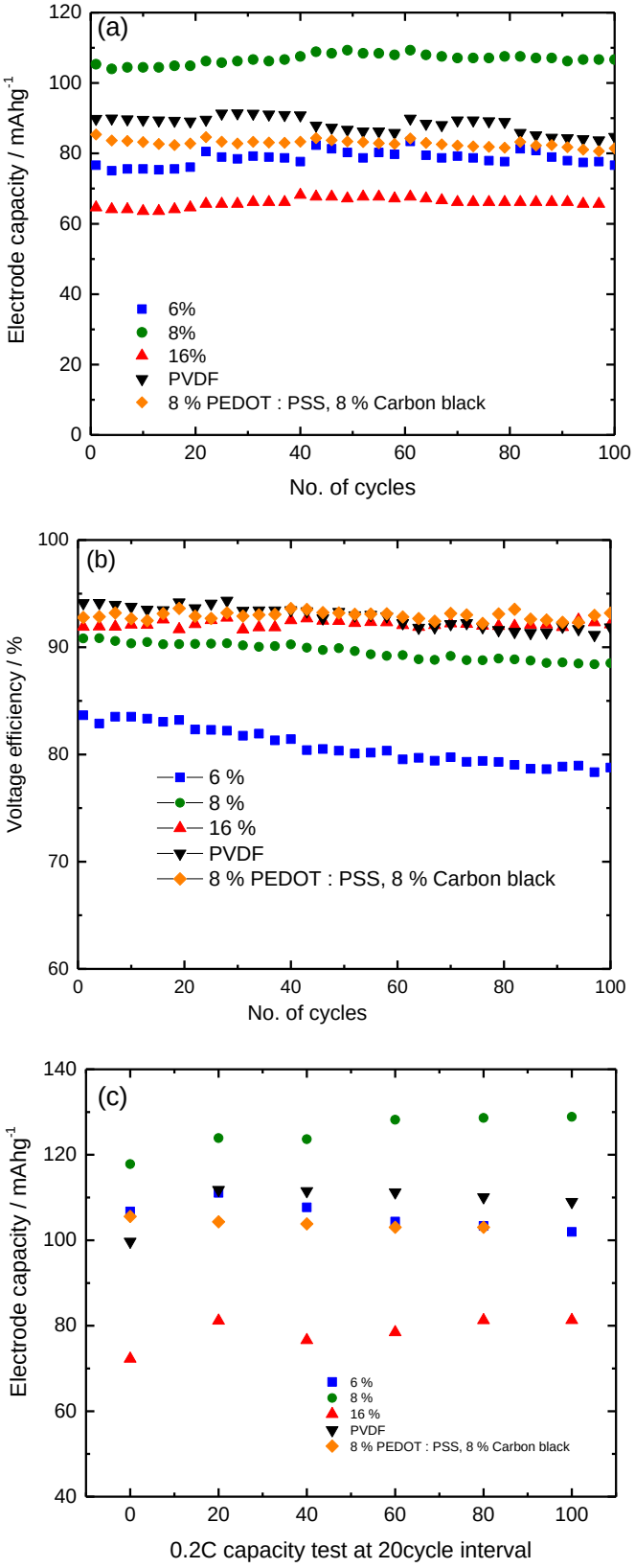

Figure 7.9. (a) Electrode performance with cycling of the composite electrodes, (b) voltage efficiency with number of cycles and (c) capacity at 0.2C after every 20 cycles at 1 C.

7.5 Conclusion

Carbon free composite positive electrodes are prepared by slurry coating process with $LiFePO_4$ as active material and PEDOT:PSS as binder material. The used conductive polymer PEDOT:PSS shows no redox activity in the potential range between 3 and 4 V and is in the conductive state. The amount of conductive polymer influences significantly the electrochemical and the morphometric properties of the positive electrode. A comparison of performance data to conventional positive electrode made of $LiFePO_4$, carbon black and PVDF reveals that replacement of inactive binder and carbon black by PEDOT:PSS, improves the rate capability of the composite positive electrode. With increasing amount of PEDOT:PSS in the composite electrode, the capacity retention at higher C- rates and the cycling stability improve. However, with the use of too much conducting polymer reduces the overall capacity. The use of PEDOT:PSS with higher electronic conductivity in the studied system provides room for further significant improvements. Moreover, the mechanical properties of PEDOT:PSS as a binder need to be evaluated.

8 Conclusion and outlook

The focus of this work is to understanding the role of conducting polymers as binder materials for lithium ion battery positive electrodes. Several conducting polymers such as PANI, POMA and PEDOT:PSS are studied alone in the aprotic electrolyte environment and their electrochemical behaviour in different potential range is analysed. These polymers are used as binder materials for composite positive electrode with $LiFePO_4$ active material and their electrochemical behaviour and battery performance with lithium counter electrode are tested. $LiFePO_4$ is used as a model system for studying the properties of the conducting polymers. For comparison conventional $LiFePO_4$/carbon black/PVDF electrode are prepared.

In the first part of the thesis the behaviour of polymers of the PANI family (PANI and POMA) are studied. They are chemically synthesized and their electrochemical behaviour in the potential range of 2.5 V to 4 V is studied using cyclic voltammetry. Polymers of the PANI family show redox activity in these potential range and changes from reduced state to oxidised state as the potential changes from 2.5 to 4 V. This change in oxidation state is associated with loss in conductivity hence at oxidised state PANI has a very low conductivity. Therefore, additional carbon black additive is always necessary when it is used as a binder for composite electrodes along with $LiFePO_4$. However, the electrodes where the PANI and POMA are used as a partial binder along with PVDF show better rate capability and higher capacity as compared to electrodes with only PVDF binder electrode. It can be due to the high three dimensional conductivity of the composite electrode and redox activity of the conducting polymer in the composite electrodes containing conducting polymer binder. The cycling behaviour of the composite electrodes is also studied. The voltage efficiency of the cells reduced with cycling due to degradation of the used conducting polymers with cycling.

A substantial part of the thesis is to study the PEDOT:PSS polymer behaviour and composite electrode prepared from it. This polymer is chosen because it shows no redox activity and high electronic conductivity in the complete potential range of 2.5 to 4 V. The behaviour of PEDOT:PSS in aprotic electrolyte at different temperature (10 °C

- 40 °C) and different scan rate is studied. The impedance behaviour at completely reduced and completely oxidised state has been studied and no significant change is found. This confirms that the change in conductivity of PEDOT:PSS is not significant with change in potential in the range 2.5 to 4 V. Hence complete replacement of the carbon additive is obtained with PEDOT:PSS as binder and $LiFePO_4$ as active material.

The PEDOT:PSS water suspension and $LiFePO_4$ are used to prepare slurry which are further coated on aluminium current collector to get positive electrodes. As PEDOT:PSS is used for the first time as binder, the processing of the slurry has not been studied previously. Hence slurries with different solvent concentration (24-45 % solid loading) are prepared and their flow behaviour is analysed using a rheometer. The flow behaviour of the slurries containing 32-40 % solid loading shows higher shear stress and viscosity than slurry with PVDF/carbon black/$LiFePO_4$. Moreover, all the composite two-component slurries show shear thinning behaviour which is beneficial during mixing of active material in the PEDOT:PSS suspension. In order to understand the settling mechanism of $LiFePO_4$, small amplitude dynamic viscosity measurement is performed. The results show that there is no settling of the active material suggesting a uniform distributed coating on aluminium. However, the slurries with 24 % and 32 % solid loading show a more fluidic behaviour than the slurries with 40 % and 45 % solid loading. This implies that the distribution of the particles in the low solid loading samples will be less uniform as compared to high solid loading samples. This is further confirmed by conductivity and adhesion strength measurements where the 40 % sample showed superior behaviour due to better distribution of particles in the coating. The performances of batteries prepared with these composite electrodes also show the superior performance of 40 % sample.

The last part of the work aimed for an understanding of the effect of PEDOT:PSS content in the composite electrode on its electrochemical performance. Three different compositions are examined where the amount of PEDOT:PSS is 6 %, 8 %, and 16 %. The rest amount is active material $LiFePO_4$. For comparison electrodes with conventional PVDF binder with carbon additive and $LiFePO_4$ are prepared and tested as well. The capacity retentions of 8 % and 16 % samples are significantly higher at 5C rate than for conventional PVDF sample. This is one of the major goals of this work. The electrode capacity of the 8 % sample is slightly higher than the PVDF sample. The new composite electrodes exhibited stable performance for 100 cycles. However, samples with 6 % solid loading behaved poorly largely due to presence of

low amount of conducting binder. Its adhesion strength is much lower than the higher PEDOT:PSS containing samples.

The work of this dissertation provides evidence that two-component composite electrode with PEDOT:PSS as conducting binder and active material can provide good electrochemical behaviour and battery performance. The objective of avoiding additional carbon additives and water-based processing is also achieved. Moreover, this work contributes to the quickly growing field of new electrode concepts for better rate capability and easier processing routes. It timely adds knowledge to the rapidly growing field of new binder development for lithium ion battery.

For implementation of PEDOT:PSS binder in commercial positive electrode preparation requires further studies. Long term cycling studies up to 1000 cycles should be performed in order to study the cycling performance thoroughly.

Full cells with graphite negative electrode and the proposed positive electrode should be prepared and their electrochemical behaviour needs to be studied. The composite electrodes should be used in pouch bag cells to understand the effect of large area electrode configuration.

The conducting binder could be tested for different active materials ($LiCoO_2$, NMC) with different particle size (micrometres to nanometres) to understand their potential for different active material based positive electrodes.

The conductivity of PEDOT depends on the type of counter ion associated with it (68). In this work only PSS counter ion is used for the binder. Hence different counter ion based PEDOT can be tested to achieve high conducting PEDOT binders. This can further improve the rate capability of the composite electrodes.

9 References

1. P. R. Epstein and C. Rodgers, Inside the Greenhouse: The Impacts of CO2 and Climate Change on Public Health in the Inner City, in, Center for Health and the Global Environment Harvard Medical School (2004).
2. Climate Change 2001: Impacts, Adaptation, and Vulnerability, in, Intergovernmental Panel on Climate Change (IPCC) (2001).
3. IPCC Special Report on Renewable Energy Sources and Climate Change Mitigation, in, Intergovernmental Panel on Climate Change (IPCC) (2001).
4. S. Pacala and R. Socolow, *Science*, **305**, 968 (2004).
5. M. Armand and J. M. Tarascon, *Nature*, **451**, 652 (2008).
6. C. Liu, F. Li, L.-P. Ma and H.-M. Cheng, *Adv. Mater.*, **22**, E28 (2010).
7. L. Dai, D. W. Chang, J.-B. Baek and W. Lu, *Small*, **8**, 1130 (2012).
8. J. B. Goodenough and K.-S. Park, *J. Am. Chem. Soc.*, **135**, 1167 (2013).
9. B. Dunn, H. Kamath and J.-M. Tarascon, *Science*, **334**, 928 (2011).
10. Z. Yang, J. Zhang, M. C. W. Kintner-Meyer, X. Lu, D. Choi, J. P. Lemmon and J. Liu, *Chem. Rev.*, **111**, 3577 (2011).
11. S. Goriparti, E. Miele, F. De Angelis, E. Di Fabrizio, R. Proietti Zaccaria and C. Capiglia, *J. Power Sources*, **257**, 421 (2014).
12. M. Osiak, H. Geaney, E. Armstrong and C. O'Dwyer, *J. Mater. Chem. A*, **2**, 9433 (2014).
13. C.-C. Li, J.-T. Lee and X.-W. Peng, *J. Electrochem. Soc.*, **153**, A809 (2006).
14. C.-C. Li, J.-T. Lee, C.-Y. Lo and M.-S. Wu, *Electrochem. Solid-State Lett.*, **8**, A509 (2005).
15. W. Porcher, B. Lestriez, S. Jouanneau and D. Guyomard, *J. Electrochem. Soc.*, **156**, A133 (2009).
16. W. Porcher, B. Lestriez, S. Jouanneau and D. Guyomard, *J. Power Sources*, **195**, 2835 (2010).
17. B. Lestriez, *CR Chim.*, **13**, 1341 (2010).
18. N.-S. Choi, Y.-G. Lee and J.-K. Park, *J. Power Sources*, **112**, 61 (2002).

19. C. Sisbandini, D. Brandell, T. Gustafsson and J. O. Thomas, *Electrochem. Solid-State Lett.*, **12**, A99 (2009).
20. C. Punckt, M. A. Pope and I. A. Aksay, *J. Phys. Chem. C*, **117**, 16076 (2013).
21. S. Xun, X. Song, V. Battaglia and G. Liu, *J. Electrochem. Soc.*, **160**, A849 (2013).
22. J. K. Hong, J. H. Lee and S. M. Oh, *J. Power Sources*, **111**, 90 (2002).
23. T. Takamura, M. Saito, A. Shimokawa, C. Nakahara, K. Sekine, S. Maeno and N. Kibayashi, *J. Power Sources*, **90**, 45 (2000).
24. S. E. Cheon, C. W. Kwon, D. B. Kim, S. J. Hong, H. T. Kim and S. W. Kim, *Electrochim. Acta*, **46**, 599 (2000).
25. F. Joho, B. Rykart, R. Imhof, P. Novák, M. E. Spahr and A. Monnier, *J. Power Sources*, **81–82**, 243 (1999).
26. SIGMA-ALDRICH, Safety Data Sheet for NMP, in (2015).
27. S.-L. Chou, Y. Pan, J.-Z. Wang, H.-K. Liu and S.-X. Dou, *Phys. Chem. Chem. Phys.*, **16**, 20347 (2014).
28. K. Mizushima, P. C. Jones, P. J. Wiseman and J. B. Goodenough, *Mater. Res. Bull.*, **15**, 783 (1980).
29. M. S. Whittingham, *Chem. Rev.*, **104**, 4271 (2004).
30. N. T. a. T. K., *Prog. Batteries Sol. Cells*, **9**, 209 (1990).
31. S. Saeki, J. Lee, Q. Zhang and F. Saito, *Int. J. Miner. Process.*, **74, Supplement**, S373 (2004).
32. C.-C. Li, J.-T. Lee, Y.-L. Tung and C.-R. Yang, *J. Mater. Sci.*, **42**, 5773 (2007).
33. B. Tran, I. O. Oladeji, Z. Wang, J. Calderon, G. Chai, D. Atherton and L. Zhai, *J. Electrochem. Soc.*, **159**, A1928 (2012).
34. J.-H. Lee, J.-S. Kim, Y. C. Kim, D. S. Zang and U. Paik, *Ultramicroscopy*, **108**, 1256 (2008).
35. S. F. Lux, F. Schappacher, A. Balducci, S. Passerini and M. Winter, *J. Electrochem. Soc.*, **157**, A320 (2010).
36. J. Xu, S.-L. Chou, Q.-f. Gu, H.-K. Liu and S.-X. Dou, *J. Power Sources*, **225**, 172 (2013).
37. J.-H. Lee, U. Paik, V. A. Hackley and Y.-M. Choi, *J. Electrochem. Soc.*, **152**, A1763 (2005).
38. H. Wang, T. Umeno, K. Mizuma and M. Yoshio, *J. Power Sources*, **175**, 886 (2008).

39. J.-H. Jean and H.-R. Wang, *J. Am. Ceram. Soc.*, **84**, 267 (2001).
40. J. Chong, S. Xun, H. Zheng, X. Song, G. Liu, P. Ridgway, J. Q. Wang and V. S. Battaglia, *J. Power Sources*, **196**, 7707 (2011).
41. J. R. Szczech and S. Jin, *Energ. Environ. Sci.*, **4**, 56 (2011).
42. U. Kasavajjula, C. Wang and A. J. Appleby, *J. Power Sources*, **163**, 1003 (2007).
43. H. Buqa, M. Holzapfel, F. Krumeich, C. Veit and P. Novák, *J. Power Sources*, **161**, 617 (2006).
44. J. Li, R. B. Lewis and J. R. Dahn, *Electrochem. Solid-State Lett.*, **10**, A17 (2007).
45. P. Novák, K. Müller, K. S. V. Santhanam and O. Haas, *Chem. Rev.*, **97**, 207 (1997).
46. A. G. MacDiarmid, *Rev. Mod. Phys.*, **73**, 701 (2001).
47. H. Shirakawa, E. J. Louis, A. G. MacDiarmid, C. K. Chiang and A. J. Heeger, *J. Chem. Soc., Chem. Commun.*, 578 (1977).
48. H. S. Nalwa, in *encyclopedia of nanoscience and nanotechnology*, p. 16 (2004).
49. A. Pron and P. Rannou, *Prog. Polym. Sci.*, **27**, 135 (2002).
50. W. P. Su, J. R. Schrieffer and A. J. Heeger, *Phys. Rev. Lett.*, **42**, 1698 (1979).
51. Y. Furukawa, *J. Phys. Chem.*, **100**, 15644 (1996).
52. M. Wan, *Conducting Polymers with Micro or Nanometer Structure*, Springer-Verlag Berlin Heidelberg (2008).
53. E. T. Kang, K. G. Neoh and K. L. Tan, *Prog. Polym. Sci.*, **23**, 277 (1998).
54. A. G. MacDiarmid, L. S. Yang, W. S. Huang and B. D. Humphrey, *Synth. Met.*, **18**, 393 (1987).
55. A. Benyaich, C. Deslouis, T. El Moustafid, M. M. Musiani and B. Tribollet, *Electrochim. Acta*, **41**, 1781 (1996).
56. A. G. Macdiarmid, J.-C. Chiang, M. Halpern, W.-S. Huang, S.-L. Mu, L. D. Nanaxakkara, S. W. Wu and S. I. Yaniger, *Mol. Cryst. Liq. Cryst.*, **121**, 173 (1985).
57. M.-Y. Hua, G.-W. Hwang, Y.-H. Chuang, S.-A. Chen and R.-Y. Tsai, *Macromol.*, **33**, 6235 (2000).
58. M. Leclerc, J. Guay and L. H. Dao, *Macromol.*, **22**, 649 (1989).
59. Y. Wei, W. W. Focke, G. E. Wnek, A. Ray and A. G. MacDiarmid, *J. Phys. Chem.*, **93**, 495 (1989).

60. D. Macinnes Jr and B. L. Funt, *Synth. Met.*, **25**, 235 (1988).
61. L. H. C. Mattoso, S. V. Mello, A. Riul, O. N. Oliveira and R. M. Faria, *Thin Solid Films*, **244**, 714 (1994).
62. A. G. MacDiarmid, *Angew. Chem. Int. Ed.*, **40**, 2581 (2001).
63. S. B. Basame and H. S. White, *J. Phys. Chem.*, **99**, 16430 (1995).
64. C. J. Boxley, H. S. White, C. E. Gardner and J. V. Macpherson, *J. Phys. Chem. B*, **107**, 9677 (2003).
65. N. S. Pereira, M. J. A. Sales and A. M. Ceschin, *Polímeros*, **22**, 384 (2012).
66. R. M. Melo, N. O. Dantas, N. C. d. Souza, O. N. Oliveira Jr., R. M. Faria and A. Marletta, *Química Nova*, **26**, 177 (2003).
67. G. Tourillon and F. Garnier, *J. Electroanal. Chem. Interfacial Electrochem.*, **135**, 173 (1982).
68. A. Elschner, S. Kirchmeyer, W. Lovenich, U. Merker and K. Reuter, *PEDOT: Principles and Applications of an Intrinsically Conductive Polymer*, CRC Press (2010).
69. J. F. a. H. G, in, Germany (1988).
70. B. Winther-Jensen, D. W. Breiby and K. West, *Synth. Met.*, **152**, 1 (2005).
71. F. Jonas, K. Lerch and W. Fischer, in *Bayer AG*, Germany (1996).
72. M. D. Levi, Y. Gofer and D. Aurbach, *Polymers for Advanced Technologies*, **13**, 697 (2002).
73. F. Goto, K. Abe, K. Ikabayashi, T. Yoshida and H. Morimoto, *J. Power Sources*, **20**, 243 (1987).
74. J. Manuel, P. Raghavan, C. Shin, M.-Y. Heo, J.-H. Ahn, J.-P. Noh, G.-B. Cho, H.-S. Ryu and H.-J. Ahn, *Mater. Res. Bull.*, **45**, 265 (2010).
75. A. Corradini, M. Mastragostino, A. S. Panero, P. Prosperi and B. Scrosati, *Synth. Met.*, **18**, 625 (1987).
76. Y. Kiya, A. Iwata, T. Sarukawa, J. C. Henderson and H. D. Abruña, *J. Power Sources*, **173**, 522 (2007).
77. M. Dietrich, J. Heinze, G. Heywang and F. Jonas, *J. Electroanal. Chem.*, **369**, 87 (1994).
78. Y.-H. Huang and J. B. Goodenough, *Chem. Mater.*, **20**, 7237 (2008).
79. S. Kuwabata, S. Masui and H. Yoneyama, *Electrochim. Acta*, **44**, 4593 (1999).
80. A. D. Pasquier, F. Orsini, A. S. Gozdz and J. M. Tarascon, *J. Power Sources*, **81–82**, 607 (1999).

81. G. X. Wang, L. Yang, Y. Chen, J. Z. Wang, S. Bewlay and H. K. Liu, *Electrochim. Acta*, **50**, 4649 (2005).
82. D. Lepage, C. Michot, G. Liang, M. Gauthier and S. B. Schougaard, *Angew. Chem.*, **123**, 7016 (2011).
83. L.-J. Her, J.-L. Hong and C.-C. Chang, *J. Power Sources*, **157**, 457 (2006).
84. C. Arbizzani, M. Mastragostino and M. Rossi, *Electrochem. Commun.*, **4**, 545 (2002).
85. A. V. Murugan, *Electrochim. Acta*, **50**, 4627 (2005).
86. X. Liu, H. Li, D. Li, M. Ishida and H. Zhou, *J. Power Sources*, **243**, 374 (2013).
87. D.-l. Ma, Z.-y. Cao, H.-g. Wang, X.-l. Huang, L.-m. Wang and X.-b. Zhang, *Energ. Environ. Sci.*, **5**, 8538 (2012).
88. K. S. Park, S. B. Schougaard and J. B. Goodenough, *Adv. Mater.*, **19**, 848 (2007).
89. Y.-H. Huang, K.-S. Park and J. B. Goodenough, *J. Electrochem. Soc.*, **153**, A2282 (2006).
90. T. Tamura, Y. Aoki, T. Ohsawa and K. Dokko, *Chem. Lett.*, **40**, 828 (2011).
91. S. Kuwabata, T. Idzu, C. R. Martin and H. Yoneyama, *J. Electrochem. Soc.*, **145**, 2707 (1998).
92. C. W. Y. J. Y. Shi, K. Kim, *Bull. Korean Chem. Soc.*, **31**, 3 (2010).
93. F. M. Courtel, S. Niketic, D. Duguay, Y. Abu-Lebdeh and I. J. Davidson, *J. Power Sources*, **196**, 2128 (2011).
94. J.-M. Kim, H.-S. Park, J.-H. Park, T.-H. Kim, H.-K. Song and S.-Y. Lee, *ACS Appl. Mater. Inter.*, **6**, 12789 (2014).
95. A. Ponrouch and M. R. Palacín, *J. Power Sources*, **196**, 9682 (2011).
96. K. M. Kim, W. S. Jeon, I. J. Chung and S. H. Chang, *J. Power Sources*, **83**, 108 (1999).
97. G.-W. Lee, J. H. Ryu, W. Han, K. H. Ahn and S. M. Oh, *J. Power Sources*, **195**, 6049 (2010).
98. H. A. Barnes, J. F. Hutton and K. Walters, *An Introduction to Rheology*, Elsevier (1997).
99. S. Gebhard, *A Practical Approach to Rheology and Rheometry*, Gebrueder HAAKE GmbH, Karlsruhe (2000).
100. E. Ligneel, B. Lestriez, A. Hudhomme and D. Guyomard, *J. Electrochem. Soc.*, **154**, A235 (2007).

101. W. Bauer and D. Nötzel, *Ceram. Int.*, **40**, 4591 (2014).
102. T. F. Tadors, *Applied Surfactants: Principles and Applications*, Wiley- VCH Verlag GmbH & Co. KGaA, Weinheim (2005).
103. J. Goodwin and R. Hughes, Rheology for Chemists : An Introduction, in, p. P001 (2008).
104. J.-C. Chiang and A. G. MacDiarmid, *Synth. Met.*, **13**, 193 (1986).
105. W. Haselrieder, B. Westphal, H. Bockholt, A. Diener, S. Höft and A. Kwade, *Int. J. Adhes. Adhes.*, **60**, 1 (2015).
106. B. Pałys and P. Celuch, *Electrochim. Acta*, **51**, 4115 (2006).
107. M. Ibrahim and E. Koglin, *Acta Chim. Slov*, **52**, 5 (2005).
108. S. Quillard, G. Louam, J. P. Buisson, M. Boyer, M. Lapkowski, A. Pron and S. Lefrant, *Synth. Met.*, **84**, 805 (1997).
109. X. Wang, S. Ray, M. Gizdavic-Nikolaidis and A. J. Easteal, *J. Polym. Sci., Part A: Polym. Chem.*, **50**, 353 (2012).
110. W. A. Gazotti Jr and M.-A. De Paoli, *Synth. Met.*, **80**, 263 (1996).
111. W. F. Alves, E. C. Venancio, F. L. Leite, D. H. F. Kanda, L. F. Malmonge, J. A. Malmonge and L. H. C. Mattoso, *Thermochim. Acta*, **502**, 43 (2010).
112. N. C. de Souza, J. R. Silva, J. A. Giacometti and O. N. Oliveira Jr, *Thermochim. Acta*, **441**, 124 (2006).
113. H. S. O. Chan, L. M. Gan, T. S. A. Hor, S. H. Seow and L. H. Zhang, *Thermochim. Acta*, **225**, 75 (1993).
114. T. Radojičić, Application of polyaniline (PANI) and polyanisidine (POMA) in lithium ion battery cathodes, in, Oldenburg university, Oldenburg (2012).
115. P. K. Upadhyay and A. Ahmad, *Chinese Journal of Polymer Science*, **28**, 191 (2010).
116. K. S. Ryu, B. W. Moon, J. Joo and S. H. Chang, *Polymer*, **42**, 9355 (2001).
117. T. Ohtake and H. Tanaka, *Polym J*, **48**, 25 (2016).
118. G. Inzelt, *Conducting Polymers, A New Era in Electrochemistry* (2012).
119. A. V. Plakhotnyk, L. Ernst and R. Schmutzler, *J. Fluorine Chem.*, **126**, 27 (2005).
120. T. Kawamura, S. Okada and J.-i. Yamaki, *J. Power Sources*, **156**, 547 (2006).
121. H. H. Lee, C. C. Wan and Y. Y. Wang *J. Electrochem. Soc.*, **151**, A542 (2004).
122. D. Aurbach, I. Weissman, A. Zaban and P. Dan, *Electrochim. Acta*, **45**, 1135 (1999).

123. M. J. R. Barsoukov Evgenij, *Impedance Spectroscopy, Theory, Experiment, and Applications*, Wiely Interscience (2005).
124. S.-B. Yoon, J.-P. Jegal, K. C. Roh and K.-B. Kim, *J. Electrochem. Soc.*, **161**, H207 (2014).
125. M. M. Musiani, *Electrochim. Acta*, **35**, 1665 (1990).
126. X. Ren and P. G. Pickup, *J. Chem. Soc. Faraday T.*, **89**, 321 (1993).
127. W. J. Albery and A. R. Mount, *J. Chem. Soc. Faraday T.*, **89**, 327 (1993).
128. J. Zhou, D. H. Anjum, L. Chen, X. Xu, I. A. Ventura, L. Jiang and G. Lubineau, *J. Mater. Chem. C*, **2**, 9903 (2014).
129. O. T. A. Rudolph Natalie Polymer Rheology: Fundamentals and Applications, Hanser (2014).
130. A. Benchabane and K. Bekkour, *Colloid Polym. Sci.*, **286**, 1173 (2008).
131. E. Ligneel, B. Lestriez, A. Hudhomme and D. Guyomard, *Electrochem. Solid-State Lett.*, **10**, A122 (2007).
132. T. F. Tadros, *Solid/Liquid Dispersions*, Academic Press, London (1987).
133. S. R. Raghavan, J. Hou, G. L. Baker and S. A. Khan, *Langmuir*, **16**, 1066 (2000).
134. S. R. Raghavan, M. W. Riley, P. S. Fedkiw and S. A. Khan, *Chem. Mater.*, **10**, 244 (1998).
135. R. G. Larson, *The Structure and Rheology of Complex Fluids*, Oxford University Press, Newyork (1998).
136. J. Goodwin and R. Hughes, (2008).
137. D. H. Napper, *Journal of Colloid and Interface Science*, **58**, 390 (1977).
138. G. Fritz, V. Schädler, N. Willenbacher and N. J. Wagner, *Langmuir*, **18**, 6381 (2002).
139. G. P. van der Beek, U. Gontermann-Gehl and E. Krafczyk, *J. Eur. Ceram. Soc.*, **15**, 741 (1995).
140. K. S. Ishizaki Kozo, Nanko Makoto *Porous Materials*, Springer US (1998).
141. L. Komsiyska, S. A. Garnica, M. Lewerenz, D. Ledwoch and O. Osters, *Advances in Science and Technology*, **93**, 158 (2014).
142. H. Gunderson, R. Boyce, J. Nyengaard and A. Odgaard, *Bone*, **14**, 217 (1993).
143. B. Son, M.-H. Ryou, J. Choi, T. Lee, H. K. Yu, J. H. Kim and Y. M. Lee, *ACS Appl. Mater. Inter.*, **6**, 526 (2014).

144. J. Chen, J. Liu, Y. Qi, T. Sun and X. Li, *J. Electrochem. Soc.*, **160**, A1502 (2013).

145. Y.-D. Cho, G. T.-K. Fey and H.-M. Kao, *J. Power Sources*, **189**, 256 (2009).

146. R. R. Zhao, G. Z. Ma, L. C. Zhu, A. J. Li and H. U. Chen, *Int. J. Electrochem. Sci.*, **7**, 10923 (2012).

147. D. Y. W. Yu, K. Donoue, T. Inoue, M. Fujimoto and S. Fujitani, *J. Electrochem. Soc.*, **153**, A835 (2006).

148. K. Zaghib, M. Dontigny, A. Guerfi, J. Trottier, J. Hamel-Paquet, V. Gariepy, K. Galoutov, P. Hovington, A. Mauger, H. Groult and C. M. Julien, *J. Power Sources*, **216**, 192 (2012).

149. E. Remy and E. Thiel, *Pattern. Recogn. Lett.*, **23**, 649 (2002).

150. S. Lowell, J. E. Shields, M. A. Thomas and M. Thommes, *Characterization of Porous Solids and Powders: Surface Area, Pore Size and Density*, Springer, Netherlands (2004).

151. D. Menshykau and R. G. Compton, *Electroanalysis*, **20**, 2387 (2008).

152. C. Punckt, M. A. Pope, J. Liu, Y. Lin and I. A. Aksay, *Electroanalysis*, **22**, 2834 (2010).

153. G. Liu, H. Zheng, X. Song and V. S. Battaglia, *J. Electrochem. Soc.*, **159**, A214 (2012).

154. J.-B. Donnet, *Carbon Black: Science and Technology* (1993).

155. J. Yang, J. Wang, X. Li, D. Wang, J. Liu, G. Liang, M. Gauthier, Y. Li, D. Geng, R. Li and X. Sun, *J. Mater. Chem.*, **22**, 7537 (2012).

156. D. Zane, M. Carewska, S. Scaccia, F. Cardellini and P. P. Prosini, *Electrochim. Acta*, **49**, 4259 (2004).

10 Own publications and conferences

Publications

I. P. R. Das, A. Gräfenstein, D. Ledwoch, O. Osters, L. Komsiyska and G. Wittstock, ECS Trans., 63, 31 (2014).

II. P. R. Das, L. Komsiyska, O. Osters and G. Wittstock, *Synth. Met.*, **215**, 86 (2016).

III. P. R. Das, L. Komsiyska, O. Osters and G. Wittstock, *J. Electrochem. Soc.*, **162**, A674 (2015).

Poster presentations

I. Kraftwerkbatterie Konferenz, 27.04.-29.04.2015, Aachen
P. R. Das, L. Komsiyska, O. Osters and G. Wittstock: "Pedot:PSS a functional binder material for Lithium ion battery."

II. Gesellschaft Deutscher Chemiker, Electrochemistry, 22.09-24.09.2014, Mainz
P. R. Das, A. Gräfenstein, D. Ledwoch, O. Osters, L. Komsiyska and G. Wittstock: "Conducting polymers as a functional binder for cathodes of Li-ion battery."

III. Kraftwerkbatterie Konferenz, 25.03.-26.03.2014, Münster
P. R. Das, A. Gräfenstein, D. Ledwoch, O. Osters, L. Komsiyska and G. Wittstock: "A Comprehensive Study of the Influence of the Synthesis Conditions on the Performance of PEDOT:p-Tos in Li-Ion Batteries."

Oral presentations

I. AGEF-Symposium, 08.04.2015, Oldenburg, P. R. Das, L. Komsiyska, O. Osters and G. Wittstock: "Application of Carbon Black Free Cathodes in Li-Ion Batteries."

II. 15th International Conference Advanced Batteries, Accumulators and Fuel Cells [ABAF 15th], 24.08-28.08.2014, Brno, Czech Republic

P. R. Das, A. Gräfenstein, D. Ledwoch, O. Osters, L. Komsiyska and G. Wittstock: “Application of Conducting Polymers as cathodic Binders for Li-ion Batteries.“

11 Curriculum viate

Personal date

Name	Pratik Ranjan Das
Date of birth	30/05/1987
Place of birth	Basudevpur
Nationality	Indian

Education

09/2012 - 05/2016	PhD student in Electrochemistry, university of Oldenburg, Oldenburg, Germany Thesis title: “Conducting polymers as functional binders for lithium ion battery positive electrodes “.
10/2009 - 06/2012	Master of Science in Advanced Materials and Process, F.A.U.Erlangen, Germany Elite graduate program with 30 credits of soft-skill courses Average grade: 1.8. Thesis titel: “Investigation of foaming behavior of rubber toughened Polymers”.
05/2005 - 09/2009	Bachelor of Technology in Metallurgical and Materials Engineering, National Institute of Technology, Nagpur, India Average grade 8.5/10.

Ich versichere hiermit, dass ich diese Arbeit selbstständig verfasst und nur die angegebenen Quellen und Hilfsmittel benutzt habe. Während der Dissertation sind die Untr "Publications" aufgelisteten Veröffentlichungen entstanden. Die Dissertation hat weder zu Teilen noch in Gänze einer anderen wissenschaftlichen Hochschule zur Begutachtung in einem Promotionsverfahren vorgelegen.

Oldenburg, den

Pratik Ranjan Das